

**Cellular and subcellular characterization of prostate carcinomas
by molecular magnetic resonance imaging**

Inaugural-Dissertation
to obtain the academic degree
Doctor rerum naturalium (Dr. rer. nat.)

submitted to the Department of Biology, Chemistry, Pharmacy
of Freie Universität Berlin

by

Avan Kader
born in Altamim/ Iraq

Berlin 2022

This thesis was carried out at the Charité - Universitätsmedizin Berlin, Department of Radiology in Berlin from February 2019 until July 2022 under the supervision of Professor Dr. med. Marcus R. Makowski.

First Reviewer:

Univ.- Professor Dr. med. Marcus R. Makowski

Klinikum rechts der Isar
Der Technischen Universität München
Institut für Diagnostische und Interventionelle Radiologie
Ismaninger Str. 22
81675 München

Second Reviewer:

Univ.- Professor Dr. med. Andreas Diefenbach

Charité - Universitätsklinik Berlin
Institut für Mikrobiologie und Infektionsimmunologie
Hindenburgdamm 30
12203 Berlin

Date of defense: 22th May 2023

Natural science does not simply describe and explain nature, it is part of the interplay between nature and ourselves.

Werner Heisenberg

Table of Contents

List of Figures and Tables	1
List of Abbreviations	2
Summary	5
Zusammenfassung	7
1. Introduction	9
1.1 Prostate Cancer	9
1.1.1 Molecular biology of prostate cancer	10
1.1.2 Biomarker for PCa and clinical diagnosis	15
1.1.2.1. Challenges in PCa biomarker screening	17
1.1.3 Treatment of PCa	19
1.1.4 Animal models of prostate cancer	20
1.2 Imaging modalities for prostate cancer	22
1.2.1 Magnetic resonance imaging	22
1.2.1.1 Principles of MRI	23
1.2.1.2 MRI of prostate cancer	25
1.3 Molecular MR imaging	26
1.3.1 Biological targets for molecular imaging	27
1.3.2 Macrophage marker for molecular imaging	29
2. Aims and Objectives of the Thesis	31
3. Publication I	32
4. Publication II	50
5. Discussion	65
5.1 Molecular MR imaging for diagnosis and characterization of PCa with an elastin-specific molecular probe	65
5.2 Superparamagnetic iron-oxide nanoparticle for visualization of PCa in MRI	67
5.3 Current and future trends in molecular imaging of prostate carcinoma	69
5.4 Limitations	71
6. References	73
7. Publications	98
Danksagung	101
Selbstständigkeitserklärung	102

List of Figures and Tables

List of Figures

- Figure 1.** Schematic representation of zones of the human prostate.
- Figure 2.** Schematic representation of prostate epithelium from human and mouse.
- Figure 3.** Model of prostate cancer progression.
- Figure 4.** Androgen cycle in the prostate cancer cell.
- Figure 5.** Schematic illustration of histological phenotypes classified by Gleason score.
- Figure 6.** Prostate cancer biomarker to differentiate aggressive from non-aggressive tumors.
- Figure 7.** Different prostate cancer mouse models in SCID-mice.

List of Tables

- Table 1.** Classification of prostate cancer stage.

List of Abbreviations

ADC	apparent diffusion coefficients
AR	androgen
CDCA8	cell division cycle associated 8
CDK	cyclin-dependent kinase
CENPA	centromere protein A
CRPC	castration-resistant prostate cancer patients
CRT	conformal radiation therapy
CT	computed tomography
DCE-MRI	dynamic contrast-enhanced MRI
DRE	digital rectal examination
DW	diffusion-weighted imaging
EBPs	elastin-binding proteins
ECM	extracellular matrix
EDB-FN	extra domain B fibronectin
Fe ³⁺	ferric cation
FOXA1	forkhead box A1
fPSA	free prostate-specific antigen
GRP	gastrin-releasing peptide
Gd	gadolinium
Gd-DTPA	gadopentetate dimeglumine
Gd ³⁺	gadolinium chelates
GRPR	gastrin-releasing peptide receptor
h	hour
H ₂ O	water
HIFU	high-intensity focused ultrasound
ICP-AES	inductively coupled plasma atomic emission spectrometry
ICP-MS	inductively coupled plasma mass spectrometry
IL-6	interleukin-6

List of Abbreviations

IMRI	intensity modulated radiation therapy
IONPs	magnetic iron-oxide nanoparticles
kg	kilogram
KIF20A	kinesin family member 20A
LA-ICP-MS	laser ablation-inductively coupled plasma mass spectrometry
mg	milligram
min	minute
MIRB	Molday ION Rhodamine-B carboxyl
miRNA	micro ribonucleic acid
mm ³	cubic millimeter
mmol	millimole
MMPs	matrix metalloproteinases
MNPs	magnetic iron-oxide nanoparticles
mpMRI	multi-paramagnetic magnetic resonance imaging
MR	magnetic resonance
MRI	magnetic resonance imaging
ms	milliseconds
MTMs	breast cancer macrophages
MYC	c-MYC protooncogene
NKX3.1	NK homeobox 1
nm	nanometer
NOD	non-obese diabetic
PARP	poly-ADP-ribose polymerase
PCa	prostate carcinoma
PET	positron emission tomography
PHI	Prostic Health Index
PI-RADS	Prostate Imaging Reporting and Data System
PIN	prostate intraepithelial neoplasia
PSA	prostate-specific antigen
PSMA	prostate-specific membrane antigen

List of Abbreviations

PTEN	phosphatase and tensin homolog
Rb	retinoblastoma protein
RB1	retinoblastoma susceptibility gene
SCID	severe combined immunodeficiency
SI	signal intensity
SNR	signal-to-noise-ratio
SPIONs	superparamagnetic iron-oxide nanoparticles
T	Tesla
TAM	tumor-associated macrophages
TESMA	tropoelastin-binding peptide
TME	tumor microenvironment
TNM	tumor volume; involvement of lymph nodes; metastasis classification
TRUS	transrectal ultrasound examination
uSPIONs	ultra-small superparamagnetic iron-oxide nanoparticles
mM	millimolar
mmol	millimoles
¹ H-MRSI	proton magnetic resonance spectroscopic imaging

Summary

Prostate carcinoma (PCa) is one of the most frequently diagnosed cancers in men worldwide and the second most common cause of cancer death in 2021. The etiology of PCa is still largely unknown, but some factors promote tumor development and progression in the prostate. These factors include environmental factors, genetic predisposition, and especially age. At >65 years, the risk of PCa increases exponentially and the mortality rate can be linked to age. Patients can remain symptom-free in the early PCa stage. As the tumor progresses, symptoms may include bone pain, urinary dysfunction, weight loss, and anemia. In the course, metastases develop in the body, initially in local lymph nodes or bones. PCa is usually diagnosed at an intermediate or terminal stage, which makes it challenging for treatment and recovery.

Human prostate tissue consists of three main types of epithelial cells: luminal, basal, and neuroendocrine. These epithelial cell types are also found in the prostate of male mice, making a mouse model ideal for PCa research. PCa develops mainly from luminal cells, but basal cells can also act as prostate cancer-initiating cells. Several processes are involved in the pathophysiology of PCa progression: precursor intraepithelial neoplasia, followed by localized PCa and advanced PCa. Progression of prostate cancer occurs in several phases and is associated with various genetic, molecular, and cellular changes, e.g. changes in androgens. The prostate-specific antigen (PSA) is involved in the regulation of androgens. PSA is mainly used in oncology as a biomarker for PCa but is criticized for its low specificity. The tumor microenvironment also plays an important role in tumorigenesis, being involved in numerous processes such as tumor development, metastasis, and the development of resistance to therapy. Stromal cells include fibroblasts, macrophages, lymphocytes, mast cells, endothelial cells, pericytes, smooth muscle cells, and extracellular matrix (ECM) proteins.

The current clinical reference standard to diagnose PCa is the histologic evaluation by transrectal ultrasound-guided systematic core needle biopsy. In addition, rectal palpation, biomarker determination in the blood, and different imaging techniques are used in the diagnostic workup. These imaging techniques include transrectal ultrasound (TRUS), computed tomography (CT), positron emission tomography (PET), and conventional magnetic resonance imaging (MRI). For MRI examinations, a gadolinium-based imaging probe is often used to obtain strong contrast images of the tissue structure.

Molecular MRI is an intensively researched field since it allows *in vivo* visualization of biological and biochemical processes at the molecular and cellular levels. This work aimed to apply specific molecular probes in PCa using a probe that specifically binds to elastic fibers and visualizes

Summary

pathological changes quantitatively. Secondly, iron-oxide particles, ferumoxytol, were used, whereby the particles are phagocytosed by macrophages in the tumor and therefore enable the evaluation of cellular characteristics. The experiments were performed in a small animal xenograft prostate tumor model, firstly by investigating the feasibility of each molecular probe and secondly by comparing different tumor volumes. Both imaging probes, the elastin-specific probe, and ferumoxytol, showed a good visualization and enabled an improved differentiation of PCa on MRI compared to an unenhanced scan. The tumor sizes were significantly different from each other, which could be visualized and quantified in the imaging as well as in the pathological and biological examinations.

The studies demonstrate that molecular MR imaging has great potential to improve the diagnosis, cellular characterization, risk assessment, and treatment monitoring of prostate cancer. Additionally, avoiding invasive surgery for obtaining punch biopsies would reduce the risks of complications in patients. Molecular probes improve understanding of tumor development and biology.

Zusammenfassung

Prostatakarzinome (PCa) zählen zu den häufigsten diagnostizierten Krebserkrankungen bei Männern weltweit. PCa gehörte im Jahr 2021 zu den zweithäufigsten Krebstodesursachen. Die Ätiologien für diese Erkrankung sind noch weitestgehend unbekannt, aber es gibt Faktoren, die begünstigend auf eine Tumorentwicklung und die Tumorprogression in der Prostata wirken. Zu den Faktoren gehören Umweltfaktoren, genetische Prädisposition und besonders das Alter spielt eine essenzielle Rolle. Mit fortschreitendem Alter, >65 Jahren, erhöht sich das Risiko für PCa und die Sterblichkeitsrate ist sehr stark davon abhängig. Patienten können im frühen PCa-Stadium symptomfrei bleiben. Mit dem Fortschreiten des Tumors können Symptome, wie Knochenschmerzen, Harnfunktionsstörungen, Gewichtsverlust und Anämien auftreten. Schreitet der Tumor weiter fort, entstehen Metastasen im Körper, zu Anfang in den lokalen Lymphknoten oder im Knochen. PCa wird meistens in einer mittleren oder terminalen Phase diagnostiziert, welches eine Herausforderung für die Behandlung und Genesung darstellt.

Das menschliche Prostatagewebe besteht aus drei Haupttypen von Epithelzellen: luminale, basale und neuroendokrine Zellen. Diese Epithelzelltypen finden sich auch in der Prostata von männlichen Mäusen, wodurch ein Mausmodell ideal für die PCa-Forschung ist. PCa entwickelt sich hauptsächlich aus luminalen Zellen, aber auch basale Zellen können als Prostatakrebs auslösende Zellen fungieren. An der Pathophysiologie der PCa-Progression sind mehrere Prozesse beteiligt: die intraepitheliale Vorläuferneoplasie, gefolgt vom lokalisierten PCa und dem fortgeschrittenen PCa. Das Fortschreiten des Prostatakrebses verläuft in mehreren Phasen und ist mit verschiedenen genetischen, molekularen und zellulären Veränderungen verbunden, z. B. mit Veränderungen der Androgene. Das prostataspezifische Antigen (PSA) ist an der Regulierung der Androgene beteiligt. PSA wird in der Onkologie hauptsächlich als Biomarker für PCa verwendet, wird aber wegen seiner geringen Spezifität kritisiert. Die Mikroumgebung des Tumors spielt ebenfalls eine wichtige Rolle bei der Tumorentstehung und ist an zahlreichen Prozessen wie der Tumorentwicklung, der Metastasierung und der Entwicklung von Therapieresistenz beteiligt. Zu den Stromazellen gehören Fibroblasten, Makrophagen, Lymphozyten, Mastzellen, Endothelzellen, Perizyten, glatte Muskelzellen und Proteine der extrazellulären Matrix (ECM).

Der aktuelle klinische Referenzstandard, um PCa sicher zu diagnostizieren ist die rektale Palpation, Biomarkerbestimmung im Blut, unterschiedliche bildgebende Verfahren und insbesondere die pathologischen Untersuchungen der zuvor gewonnenen Biopsien. Zu den bildgebenden Verfahren gehören unter anderem die transrektale Ultraschalluntersuchung (TRUS), Computertomographie (CT), Positronen-Emissions-Tomographie (PET) und die konventionelle

Zusammenfassung

Magnetresonanztomographie (MRT). Bei MRT-Untersuchungen wird oft ein Gadolinium-haltiges Kontrastmittel verwendet, um einen stärkeren Kontrast in der Gewebestruktur aufzuzeigen.

Die molekulare MR-Bildgebung ist ein intensiv erforschtes Gebiet, da hierdurch eine Visualisierung von biologischen und biochemischen Prozessen *in vivo* auf molekularer und zellulärer Ebene dargestellt werden kann. Das Ziel dieser Studien war die Anwendung von spezifischen molekularen Sonden. Zum einen wurde eine auf Gadolinium basierende molekulare Sonde verwendet, welche spezifisch an elastischen Fasern bindet, pathologische Veränderungen darstellt und quantifiziert werden kann. Zum anderen wurden Eisenoxidpartikel, Ferumoxytol, verwendet, wobei die Partikel im Tumor von Makrophagen phagozytiert werden und somit zelluläre Charakteristika evaluiert werden können. Die Versuche wurden in einem Xenograft-Prostatatumor-Kleintiermodell durchgeführt, indem zum einen die Anwendbarkeit der jeweiligen Kontrastmittel untersucht und zum anderen unterschiedliche Tumorumfänge verglichen wurden. Sowohl die Elastin-spezifische Sonde als auch Ferumoxytol zeigten, dass eine Visualisierung und eine bessere Differenzierung von PCa im MRT mit diesen Sonden möglich war. Die Tumorumfänge unterschieden sich signifikant voneinander, was sowohl in der Bildgebung als auch bei den pathologischen und biologischen Untersuchungen dargestellt und quantifiziert werden konnte.

Die Studien zeigen, dass die molekulare Bildgebung mittels MRT ein großes Potenzial zur Verbesserung der Diagnose, zur zellulären Charakterisierung, Risikobewertung und Therapieüberwachung von Prostatakarzinomen darstellt. Diese neuen Parameter können zu den bereits etablierten Diagnosemöglichkeiten ergänzend wirken. Zudem würde eine molekulare Bildgebung im MRT den Patienten vor Risiken eines invasiven Eingriffes, wie der Gewinnung von Stanzbiopsien, bewahren. Molekulare Sonden verbessern das Verständnis der Tumorentwicklung und -biologie.

1. Introduction

1.1. Prostate cancer

One in eight men is diagnosed with prostate cancer (PCa) at an average age of 66. It is rare for PCa to be diagnosed in men under 40 years of age. PCa was among the second leading causes of cancer death in 2021 [1]. PCa is also expected to be one of the most common causes of death in men in 2022 [2]. In 2018, according to the Robert Koch Institut and Zentrum für Krebsregisterdaten, the PCa incidence in Germany was 65,200 and the prognosis for 2022 will be 70,100 [3].

The prostate is one of the male reproductive organs that produces seminal fluid, which is rich in phosphatase, citrate, prostate-specific antigen (PSA), and glycoproteins [4]. The prostate is a tubuloalveolar gland penetrated by the common ogival tubules of the two vas deferens and the two ducts of the vesicular glands and urethra. It is anatomically divided into four lobes [5].

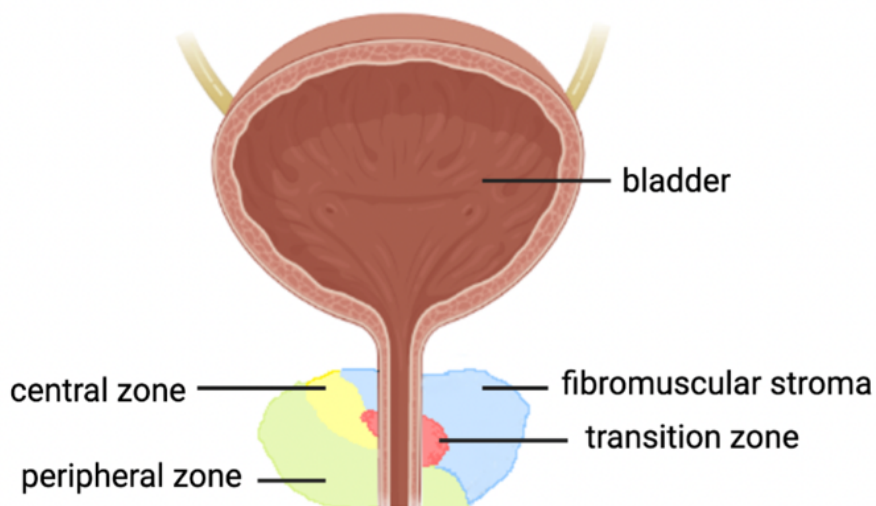


Figure 1. Schematic representation of zones of the human prostate
(modified from Sauer *et al.* [6]).

One of the special characteristics of PCa is that it grows slowly compared to other cancers. The tumor initially develops inside the prostate. As the disease progresses, the tumor cells can break through the connective tissue capsule and migrate into the neighboring tissue. In addition, the risk of metastases in the body, e.g. in the bones, increases with the progression of the disease. Together with age, ethnicity plays an important role in the incidence of PCa [7, 8]. PCa is diagnosed twice as often in dark-skinned men and has a higher mortality rate than in light-skinned men [9]. Other causes of PCa may be related to genetic background, environmental factors, and physiological status [10-12].

1.1.1. Molecular biology of prostate cancer

The development of PCa is still mainly unknown. Several processes are involved in the pathophysiology of PCa: intraepithelial precursor neoplasia, followed by localized PCa, and advanced PCa [13]. Many factors are important in the development of PCa, including androgens (AR). Until recently, high testosterone levels were thought to be among the main factors [14]. However, recent research has shown that testosterone is not responsible for the development of PCa but rather promotes tumorigenesis [15-18].

Human prostate tissue consists of three main types of epithelial cell types: luminal, basal, and neuroendocrine [19, 20]. Luminal epithelial cells are polarized, columnar cells that line the lumen. The lumen and stroma are separated by the elongated basal cells. Neuroendocrine cells are AR-negative and secrete neuropeptides and growth factors for luminal cell growth. Pathologically, the different cell types can be distinguished using cellular markers. These epithelial cell types are also found in the prostate of male mice, which makes a mouse model ideal for PCa research [21].

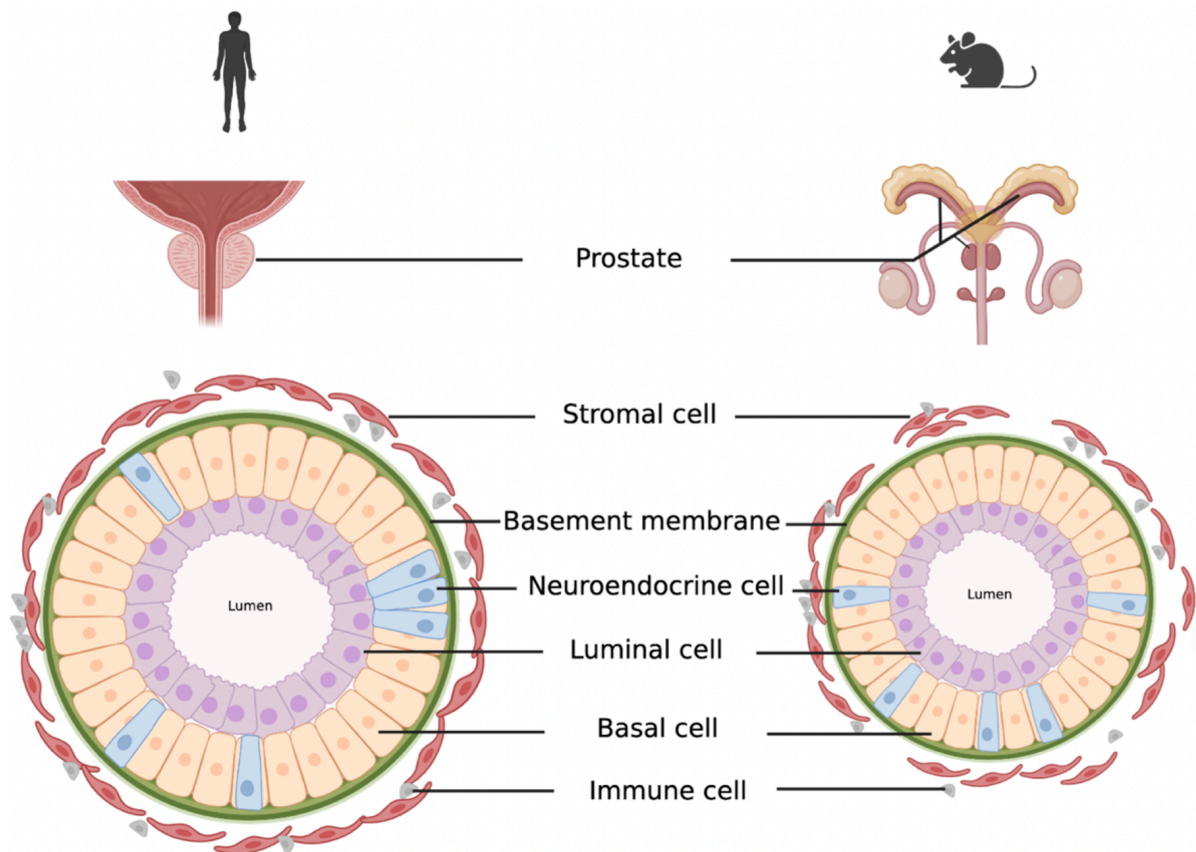


Figure 2. Schematic representation of prostate epithelium from human (left) and mouse (right)
(modified from Crowell *et al.* [22]).

It has long been hypothesized that primary prostate cancer begins in the luminal cells, luminal phenotype, which is characterized by the absence of basal cells [23, 24]. However, murine studies have shown that both basal cells and luminal cells can act as the cell of origin for prostate

Introduction

cancer [25-28]. PCa develops from the existing prostate epithelium through a multistage histological transformation, which is controlled by molecular changes [13]. Loss of phosphatase and tensin homolog (PTEN), NK3 homeobox 1 (NKX3.1), and high expression of c-MYC protooncogene (MYC) result in prostate intraepithelial neoplasia (PIN) lesions [29-33]. If the PIN lesion progresses and there is also loss of retinoblastoma protein (Rb), activation of telomerase, and usually forkhead box A1 (FOXA1) mutation, prostate adenocarcinoma develops [33-39]. Further molecular changes and mutations lead to metastases [40-45].

PTEN is a tumor suppressor. In PCa carcinogenesis, PTEN inactivation is strongly associated with tumor manifestation, through genomic deletion and rearrangement, intragenic breakage, or translocation. Loss of PTEN negatively regulates PI3'K/PKB/Akt signaling, which is involved in survival, proliferation, and energy metabolism [46]. A homeodomain transcription factor, NKX3.1, encodes a transcription factor whose expression is largely restricted to the prostate and controlled by AR [47]. Disruption of NKX3.1 contributes to prostate tumorigenesis by enabling the dedifferentiation of luminal cells [48]. MYC is a master transcription factor and is overexpressed in PCa. This can be observed in the early phase of PCa as well as in the metastatic phase. MYC overexpression has been shown to contribute to tumor initiation and progression by interfering with the AR transcription program [49]. The retinoblastoma susceptibility gene (RB1), a tumor suppressor, plays a key role in repressing the transcriptional activity of the E2F transcription factors (E2F1 and E2F3) [50, 51]. E2Fs regulate a variety of transcription genes required for the cell cycle, involved in DNA replication, nucleotide synthesis, and checkpoint control [52]. FOXA1 regulates gene transcription and is able to open surrounding chromatin and allow other transcription factors such as AR receptors to come close to their target site and exert transcriptional control of gene expression. Molecular and genetic studies have shown that FOXA1 is involved and abnormally expressed in various cancer diseases like myeloid leukemia [53], lung- [54], esophageal- [54], thyroid- [55], breast- [56], and prostate cancers [57, 58]. Human prostate cancer samples have shown that FOXA1 is overexpressed in metastatic and castration-resistant prostate cancer patients (CRPC) compared to normal and neoplastic transition zone tissues [35]. A high FOXA1 level is associated with a poor prognosis for the patient [35, 58], but other studies show that low FOXA1 levels can be found in metastatic and CRPC tumors [59, 60]. These results show that studies are needed to fully understand the role of FOXA1 in PCa. A cell proliferation regulator, p27, also plays an important role in the development of PCa. p27 binds and inhibits cyclin D, E, A, and B cyclin-dependent kinase (CDK) complexes [61].

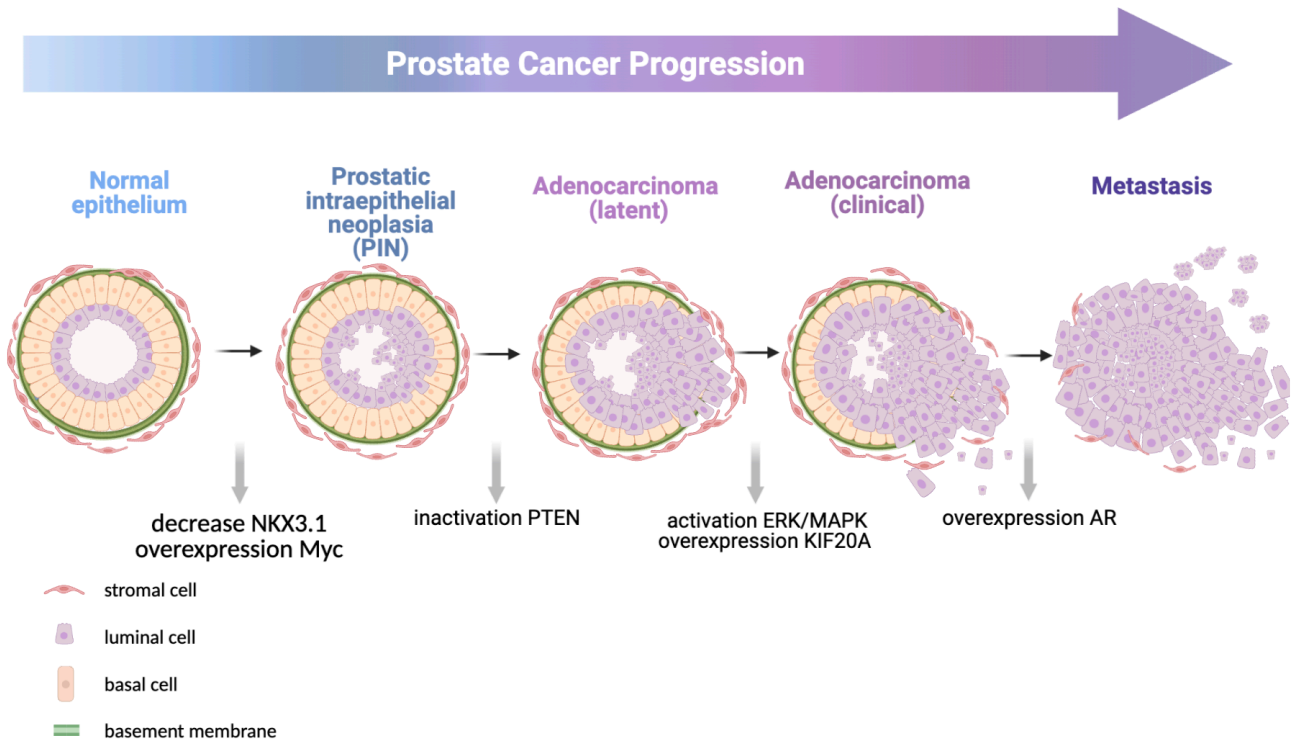


Figure 3. Model of prostate cancer progression (modified from Shen *et al.* [13]). This model shows histological changes associated with important factors in the development and progression of prostate cancer initiation and progression.

Luminal epithelial cells express a high concentration of AR [62]. They are positive for CD57-epitopes for human natural killer-1, NKX3.1, prostate-specific antigen (PSA), and cytokeratin 8 and 18-epithelium-specific filament with 19 subtypes [62, 63]. Basal epithelial cells are positive for cytokines 5 and 14, p63 (prostate basal cell marker of some PCa subtypes [64]), CD44 (a cell surface protein involved in glucose metabolism of PCa cells [65]), and GSTP1 (involved in cell cycle regulation) [62, 63, 66].

PSA is an androgen-regulated serine protease and belongs to the tissue kallikrein family [67]. PSA is mainly used as a biomarker in oncology for PCa [68]. Prostate-specific membrane antigen (PSMA), a unique cell surface marker, is a type II membrane protein that is highly overexpressed in PCa [69]. PSMA, a cell surface marker, is the most widely used biomarker for PCa [70, 71] and it is a membrane-bound glycoprotein that is expressed in healthy prostate cells as well as in prostate cancer cells. Consisting of 750 amino acids, PSMA plays an important role in nutrient uptake, receptor function, signal transduction, and cell migration [70]. In PCa, PSMA is more strongly expressed due to the downregulation of androgen receptors. Data suggest that PSMA and PSA are connected [70, 72-74]. Higher PSA levels in patients are associated with increased PSMA expression [63]. Treatments of tumor cells expressing PSMA have often achieved good therapy outcomes [70].

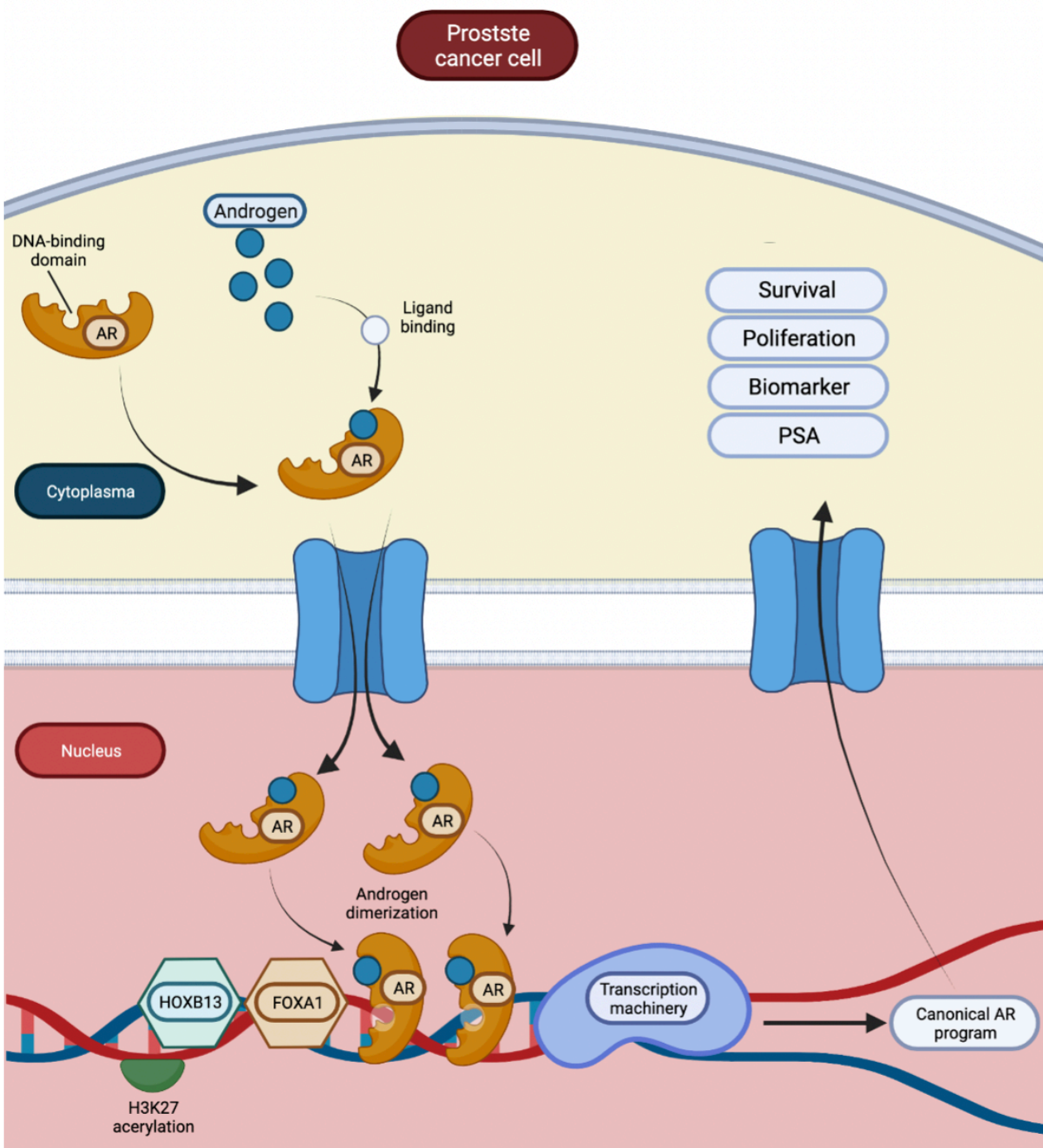


Figure 4. Androgen cycle in the prostate cancer cell (modified from Apad *et al.* [75]). Activation of the androgen receptor (AR) occurs through the binding of androgen ligands. This is followed by dimerization of the AR and translocation to the nucleus. In the nucleus, canonical transcription programs are subsequently activated, which promote cell survival, proliferation, and secretion of prostate-specific antigen (PSA).

Hub genes, such as histones H3 variant centromere protein A (CENPA), kinesin family member 20A (KIF20A), and human cell division cycle-related protein 8 (CDCA8) are overexpressed in PCa development and tumor progression [63, 76]. CENPA, an epigenetic marker, is highly overexpressed in PCa tissue and cell lines, and CENPA levels correlate with the PCa phase [77]. CENPA seems to act as a transcriptional regulator for the expression of proliferation genes, cell

cycle genes, and centromeres [77]. Thus, CENPA plays a significant role in the development of PCa [77]. Different tumor diseases show high expression of KIF20A, a kinesin-like protein [78-80]. KIF20A plays a function in mitosis and the chromosome passenger complex [79]. In addition, high expression of KIF20A correlates with poor patient survival rate [79], which has also been observed with cell division cycle associated 8 (CDCA8) [81]. CDCA8 is a chromosomal complex that is essential for genome transfer during cell division [82].

Stromal cells play a major role in tumor development and tumor progression. Stromal cells include fibroblasts, macrophages, lymphocytes, mast cells, endothelial cells, pericytes, smooth muscle cells, and extracellular matrix (ECM) proteins [83-85]. Fibroblasts, specific connective tissue cells, are involved in the formation and degradation of the ECM [63, 86]. They are particularly common in the prostate and when a tumor produces fibroblasts they can be recruited to cancer-associated fibroblasts [87]. The innate cellular immune system includes macrophages, which develop from peripheral monocytes circulating in the blood and are responsible for tissue homeostasis [88]. In the presence of a tumor, macrophages can be converted to tumor-associated macrophages (TAMs) and are essential in the infiltration of inflammatory cells. Type M1 TAMs have an inhibitory effect on tumor cells in contrast to type 2 TAMs, which have a promoting effect on tumor cells [63, 89]. These effects could also be observed in PCa [90]. Lymphocytes, a subtype of leukocytes, are an important factor in the development of PCa. Low lymphocyte levels are observed in PCa patients [91]. Mast cells influence and promote tumor angiogenesis [92, 93]. Mast cells in PCa promote the proliferation of PCa cells and the occurrence of epithelial-mesenchymal transition, invasion, and metastasis [94, 95]. Endothelial cells secrete C-C motif chemokine ligand 5 and induce autophagy, by suppressing AR expression [63, 96]. Increased autophagy promotes focal adhesion and invasion of PCa [96]. Pericytes are involved in the development and maintenance of vascular systems [97]. They regulate vascular permeability, vascular stability, and blood flow regulation, and they are involved in the interaction of vascular compression and maturation [97]. Pericytes migrate heterogeneously in tumor tissue, are freely bound to the endothelium, and are disorganized during tumor development and tumor angiogenesis [97].

Carcinoma cells can convert fibroblasts into reactive myofibroblasts, which are able to synthesize different ECM components. For the architecture and function of the ECM, protein and glycosaminoglycan fibers like collagen, fibronectin, tenascin, versican, galectin, laminin, and elastin are the most important building blocks [98]. Collagen and fibrillar proteins influence tumor progression, cell survival, apoptosis, and cell invasion [99]. Tenascin-C is a large hexameric multidomain glycoprotein in the ECM. Tenascin expression in PCa stroma and tenascin-C in the

stroma around neoplastic glands is significantly increased, suggesting a possible role for tenascin-C in regulating tumor proliferation, invasion, and metastasis [98, 100, 101]. Galectin interacts with intracellular glycoproteins, cell surface molecules, and the ECM. Galectin is thought to be expressed at a reduced level in carcinoma compared to adjacent peri-tumorous tissue [98]. Laminins are heterotrimeric molecules consisting of an α -, β - and γ -chain that are significantly less expressed in PCa compared to adjacent prostate tissue [102]. Elastin fibers are an important component of tissue stiffness and flexibility and play an important role in tumor invasion, metastasis, cell proliferation, adhesion, apoptosis, and angiogenesis [98, 103, 104]. Elastic fibers and their peptides are significantly involved in tumor invasion. Tumor cells are able to express elastin proteins, adhere, degrade and migrate [105]. The promotion of cross-linking of collagen and elastin in the tissue is determined by lysyl oxidase, a copper-dependent enzyme, and is responsible for the activation of elastin promoters [106, 107]. Interaction between tumor cells and elastin is mediated by two elastin-binding proteins, s-Gal and Galectin-3, and by laminin receptors [105].

The tumor microenvironment (TME) surrounding cancer cells plays an important role in cancer development. However, it is involved in numerous processes, including tumor growth, metastasis, and the development of therapy resistance [108].

1.1.2. Biomarker for PCa and clinical diagnosis

In the early stage of PCa, patients often remain symptom-free. Symptoms like bone pain, urinary dysfunction, weight loss, and anemia usually occur when metastases have already formed, especially in the local lymph nodes or in the skeleton [63, 109]. Most patients are diagnosed with intermediate or terminal PCa, which is a major challenge for treatment and recovery [63]. Although in recent years the diagnosis and treatment of PCa have improved, the mortality of the disease remains high.

The clinical reference standard is accompanied by rectal palpation of the prostate, and if changes in size or consistency are detected, further testing, e.g. PSA screening, is initiated [110, 111]. A high PSA level can indicate a malignant tumor, inflammation of the prostate, or prostatic hyperplasia. This is followed by a digital rectal examination (DRE) and/or a transrectal ultrasound examination (TRUS) [63, 111]. With TRUS, a needle biopsy can be combined with the collection of about twelve tissue samples for pathological-histological examination. However, a biopsy represents only a small part of the total tissue [112]. Additionally, it is an invasive procedure for the patient and involves risks such as bleeding, inflammation, infection, and also spreading of tumor cells, which detach during the biopsy and migrate into the surrounding tissue such as

perirectal or rectal tissue [113, 114]. When diagnosing PCa, a classification called TNM (T= tumor volume; N= involvement of lymph nodes; M= metastasis classification) and the Gleason score is used [115]. These parameters can be used to determine the stage of PCa. If a malignant disease of the prostate has been detected, the body is examined for the spread of the tumor by determining the spread in the body using computed tomography (CT) and/or magnetic resonance imaging (MRI). Other imaging techniques that may also be used include positron emission tomography (PET) and multi-paramagnetic MRI (mpMRI). A mpMRI includes a T2-weighted image, diffusion-directed imaging, and imaging of the prostate by using an imaging probe. This method allows not only to record the prostate volume and localization, but also to evaluate other properties of the prostate, such as cell density, certain metabolic processes, or prostate blood flow. However, there is the problem of different interpretations in reading this data, which is why the Prostate Imaging Reporting and Data System (PI-RADS) was introduced for standardization [63, 116, 117]. So far, the success has been moderate [118].

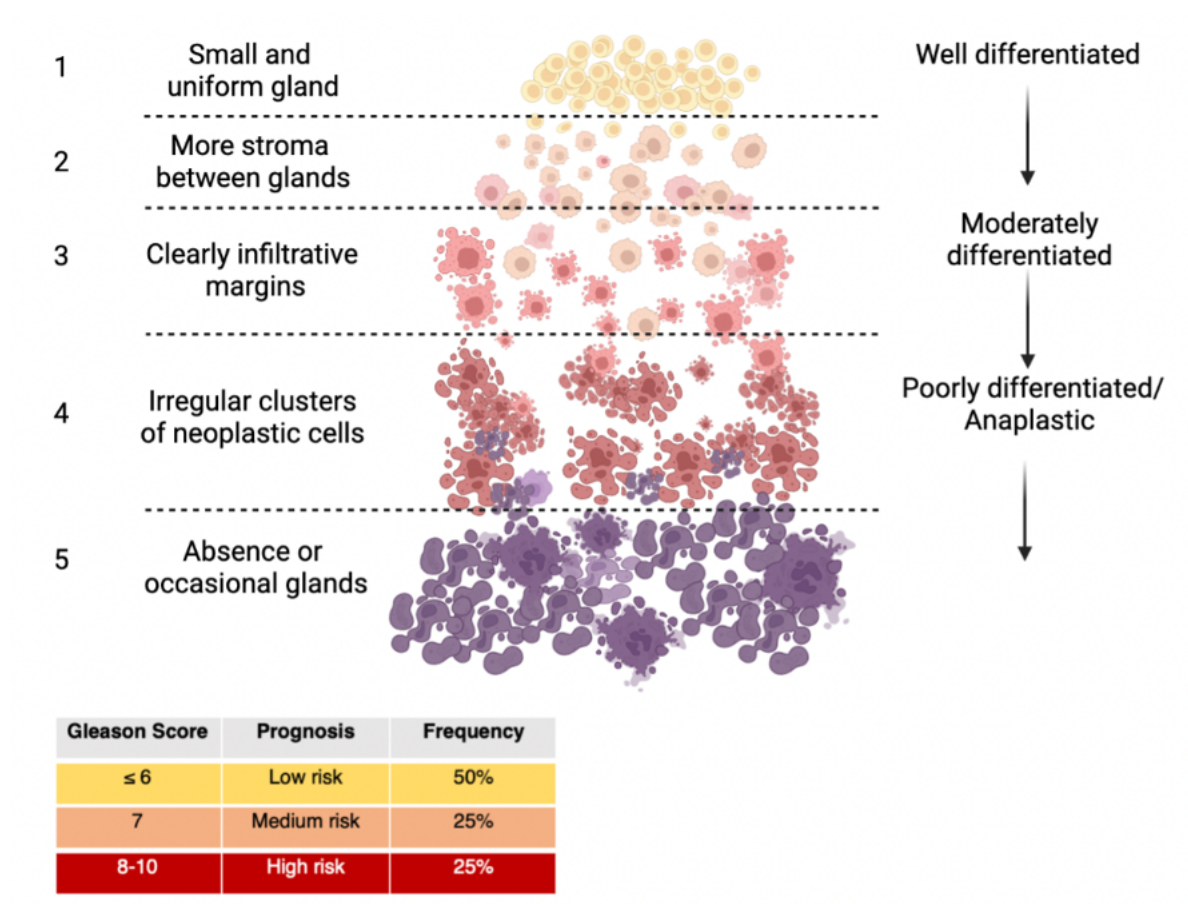


Figure 5. Schematic illustration of histological phenotypes classified by Gleason score (modified from Kim *et al.* [119]).

Table 1. Classification of prostate cancer stage (2002 AJCC TNM).

T	Characteristics
T1	Clinically asymptomatic, non-palpable tumor
T1a	Histological analysis of prostate tissue with < 5% tumorous tissue
T1b	Histological analysis of prostate tissue with >5% tumorous tissue
T1c	Tumor detection by punch biopsy, elevated PSA level
T2	Palpable tumor, localized in the prostate
T2a	Maximal half tumor flap tumorous
T2b	More than half of a prostate lobe is tumorous
T2c	Both prostate lobes affected
T3	Volume of tumor over the prostate capsule
T3a	Tumor spread on one or both sides beyond the prostate capsule, seminal vesicles not affected
T3b	Extension into the seminal vesicle
T4	Tumor is fixed and/ or adjacent tissue involved

N	Characteristics	M	Characteristics
N0	No regional lymph nodes	M0	No metastasis
N1	Regional lymph nodes are existing	M1	Metastasis are existing
NX	Regional lymph nodes cannot be identified	M1a	No regional lymph nodes
		M1b	In bones

***T** = volume of tumor; **N** = involvement of lymph nodes; **M** = metastasis classification

1.1.2.1. Challenges in PCa biomarker screening

For more than 50 years, prostate-specific antigen (PSA) has been used as a biomarker for PCa, although in recent years PSA has been found to have low specificity [120]. Screening ensures overdiagnosis of PCa, resulting in potential patient damage [121]. PSA is a protein of the kallikrein family that is synthesized in the prostate epithelium. It is segregated using seminal fluid. PSA screening is performed by immunoassay.

Not all prostate cancers increase serum PSA levels. Factors such as prostatitis, benign prostatic hyperplasia, prostate biopsies, bacterial infections, and trauma can lead to increased expression of PSA [122, 123]. Meta-analyses show that PSA screening led to an increase in prostate cancer diagnosis, but mortality remained unchanged [121].

PSA screening remains a controversial tool for the diagnosis of PCa, and new prognostic biomarkers have been explored for a while to distinguish the wide spectrum of PCa. The Prostatic Health Index (PHI) has been introduced in the United States, Australia, and European markets to predict PCa risk in addition to PSA screening. For this purpose, the biomarkers PSA, free PSA (fPSA), and [-2]proPSA are analyzed in blood serum [124].

The 4Kscore®-blood test examines four prostate biomarkers, total PSA, fPSA, intact PSA, and human kallikrein-related peptidase 2 in combination with clinical parameters in an algorithm that reflects a percentage risk of high-grade PCa [122, 125]. Higher values indicate a higher probability of tumor cells being identified in a biopsy. This combination of tests seems to be better than the collection of single biomarkers, but surgical intervention is still necessary.

Another non-invasive method is the ExoDx™ Prostate (IntelliScore) Test 18 for the diagnosis of high-grade prostate cancer. Through molecular analysis of urine, exosomal RNA, ERG, PCA3, and SPDEF are extracted [126]. The gene signature of the urine exosome gene expression assay comes from genes known to play a role in the initiation and progression of prostate cancer [126-137].

These new biomarkers appear to be promising, but they are not accessible to the entire population due to the high costs or lack of approval in the country [122].

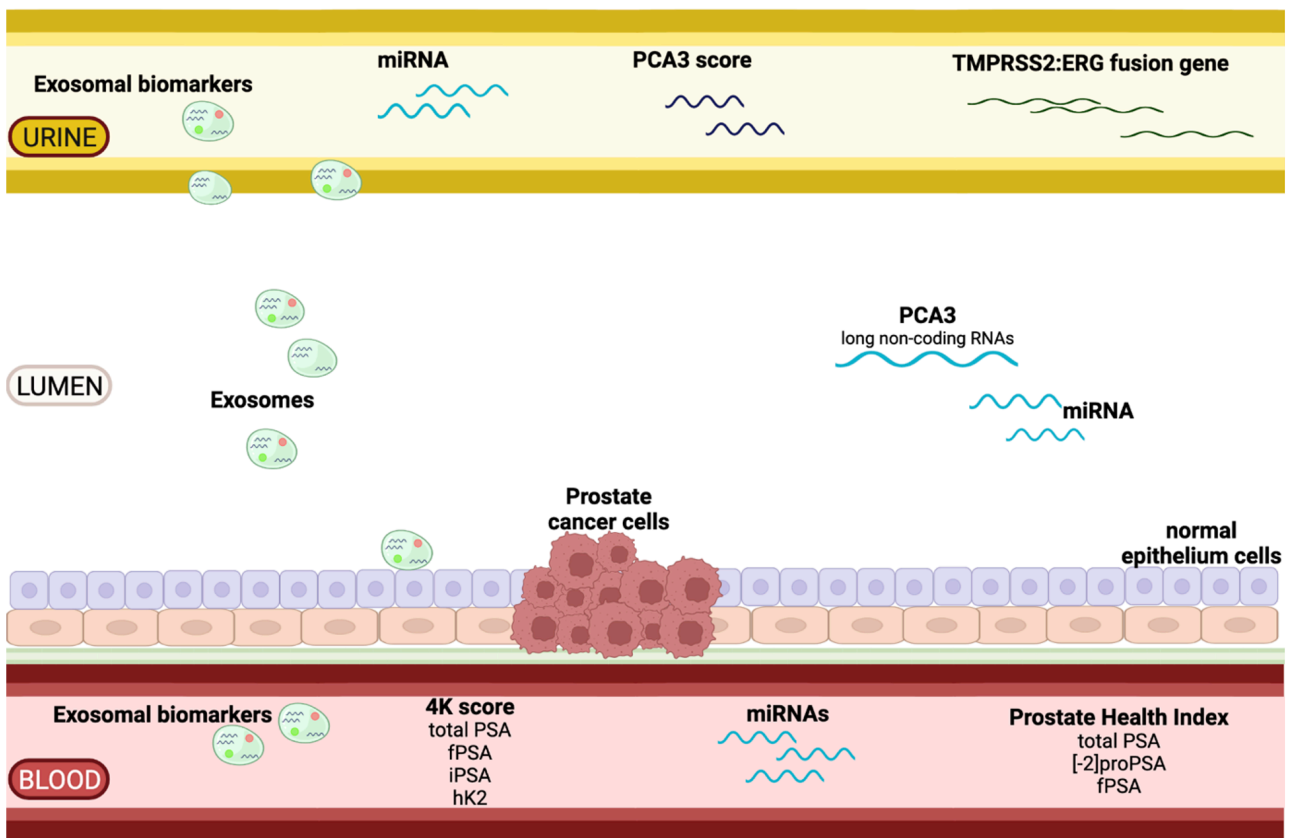


Figure 6. Prostate cancer biomarker to differentiate aggressive from non-aggressive tumors (modified from Simoes *et al.* [122]). The Prostate Health Index and the 4Kscore® are also based on blood tests, making it possible to determine the aggressiveness of the tumor. Urine tests are also suitable as a non-invasive method. Biomarkers in urine include PCA3 score and *TMPRSS2:ERG* fusion gene. microRNA (miRNA) appears to be useful as a biomarker, in urine as well as in blood, to detect PCa.

1.1.3. Treatment of PCa

Depending on the degree of PCa disease, one or more of the following treatments are selected: observation or active surveillance for PCa, surgical removal of the tumor mass, radiation therapy, cryotherapy, hormone therapy, and/or chemotherapy for prostate cancer. The following text explains the forms of therapy briefly.

In active observation, no special measures are required except for regular check-ups. Surgery aims to completely remove the cancerous tissue. The surgical technique is constantly being improved to reduce the risk of complications and side effects of the operation. Radiation therapy is continuously improved by directing the radiation precisely on the tumor tissue and without harming neighboring tissue. New technologies that can be used include conformal radiation therapy (CRT), intensity-modulated radiation therapy (IMRI), and proton radiation, which aim to reduce the side effects of radiation therapy. Early-stage PCa can be treated with high-intensity focused ultrasound (HIFU). It is used as a single treatment or in combination with radiotherapy if areas of tissue have not responded to radiotherapy. In this form of therapy, ultrasound beams are highly focused and generate heat, which destroys cancer cells. Cryotherapy can also be used as a form of treatment. Here, very low temperatures are used specifically to freeze and kill prostate cancer cells. Cryotherapy is usually only considered if the previous radiotherapy has not been successful. Hormone therapy involves suppressing the androgens to reduce the level of androgens in the body. This type of therapy is used when cancer has spread, and no surgery or radiotherapy is promising. It is also employed when surgery and/or radiotherapy have not been effective, in patients at increased risk of PCa, or before radiotherapy to reduce the size of the tumor. Androgen therapy involves medication or surgery (orchiectomy). Chemotherapy is most often used in patients at an advanced stage, by vein injection or by taking cancer drugs orally. Several chemotherapeutical drugs can be used, including Docetaxel, Cabazitaxel, Mitoxantrone, and Estramustine. Immunotherapy is based on drugs that stimulate the patient's immune system to recognize and eliminate cancer cells. A cancer vaccine (sipuleucel-T) is used, which strengthens the immune system. This type of therapy is used for advanced PCa. Targeted therapy involves drugs that identify and attack cancer cells while not harming healthy cells. Poly-APD-ribose polymerase (PARP) inhibitors are used, which block the PARP signaling pathways that are necessary for DNA repair. Targeted drug therapy is applied in advanced castration-resistant PCa. Typically, PCa needs normal testosterone levels, but in castration-resistant prostate cancer, the tumor grows despite low testosterone levels. Once the cancer cells have spread throughout the body, there are several therapy options. The metastases usually form in the bones first, which causes the patient to experience pain.

Therapy aims to prevent cancer from healing or spreading and to reduce pain. Combination therapy such as hormone therapy, chemotherapy, and vaccines could bring a positive therapeutic outcome. Drugs such as bisphosphonates, denosumab, corticosteroids, and radiopharmaceuticals can be combined with additional external radiotherapy, surgery, and/or painkillers.

All forms of therapy: observation or active surveillance for PCa, surgical removal of the tumor mass, radiation therapy, cryotherapy, hormone therapy, and chemotherapy, are recommended by the American Cancer Society [138].

1.1.4. Animal models of prostate cancer

Animal models are essential for research into the etiology, prevention, and treatment of human prostate cancer. In particular, mouse models are popular because of their similarities to the human morphology of the tissue. Additional advantages of the mouse model are handling and reproducibility.

Tissue cultures are useful for understanding the cell biology of PCa. However, they cannot reflect cellular interactions within the tumor microenvironment, so animal models still represent an unavoidable tool in PCa research.

So far, there are only a few available animal models for PCa research:

Rats are able to spontaneously develop prostate tumors [139]. The Dunning rat model is the most commonly used [140]. The Dunning R-33-27 tumor develops spontaneously, grows slowly, is well differentiated, and does not metastasize. The Lobund-Wistar rat strain develops PCa at 26 months of age on average, and when PCa is induced in these rats (using a combination of N-methyl-N-nitrosourea/testosterone treatment), PCa takes approximately 10.5 months to grow [141]. Another possibility is to generate transgenic rats. One advantage in rats over mice is the size of the prostate. Disadvantages include the smaller number of analytical reagents for tumor analysis and transgenic and knockout lines for breeding compared to mice [142].

Dogs very often develop PCa spontaneously and are mostly used to evaluate novel PCa therapies. These spontaneous models are useful, but they are genetically difficult to manipulate, unlike mice.

Mouse models play a central role in PCa research. Very often, the xenograft model is used. Here, mostly human PCa cell lines are implanted either subcutaneously or orthotopically into the prostate of immunocompromised mice, severe combined immunodeficiency (SCID), or nude mice. In 1966, the immunodeficient rodent model was first used for PCa [143]. In 1970, human prostate

cancer tissues were xenografted for the first time and in subsequent years, a spectrum of PCa cells with specific characteristics was developed [144]. The SCID mouse model is deficient in T-and B-lymphocyte functions, but normal natural killer cells and myeloid functions are present and can influence tumor growth and metastasis [145]. In the mouse orthotopic model, where human tumor cell lines are injected into the mouse prostate, it is possible to study the growth of PCa within the prostate microenvironment, tumorigenicity as well as the incidence of metastases [146].

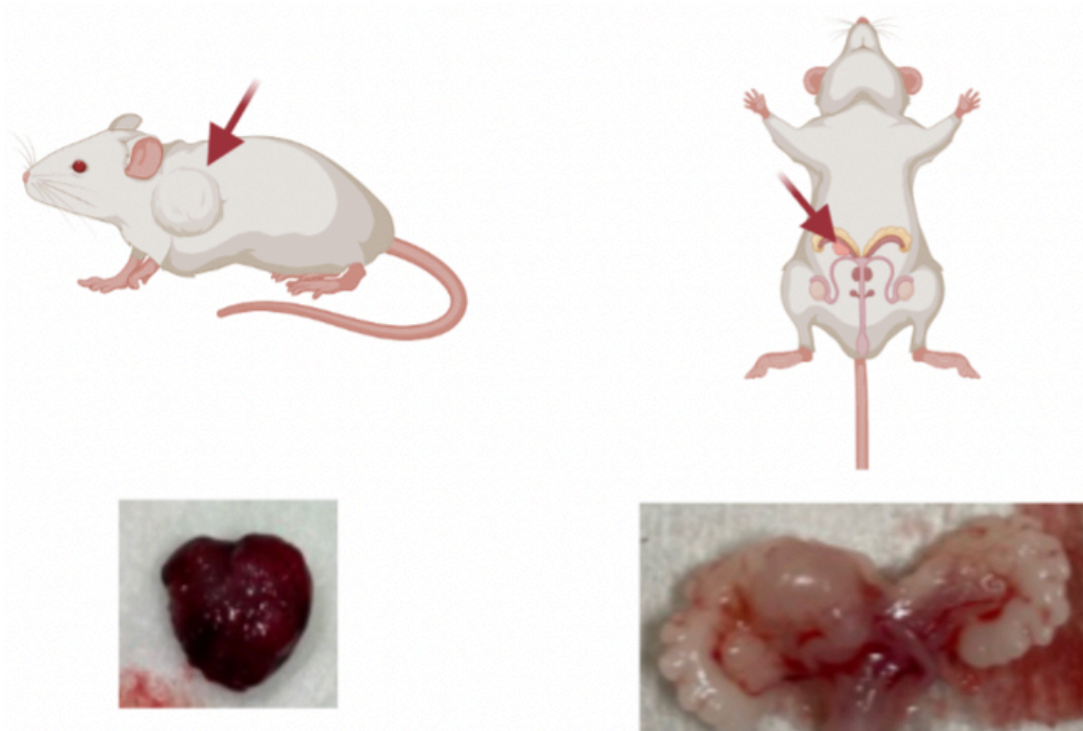


Figure 7. Different prostate cancer mouse models in SCID-mice. (Left side) shows a schematic subcutan xenograft mouse model with a tumor in the right scapula area of the mouse. The red arrow points to the tumor. The lower image shows the tumor which had a size of about 1000 mm³. (Right side) An orthotopic xenograft mouse model with tumor in the dorsal prostate lobe. The red arrow shows the tumor. The lower image shows the mouse male urogenital organs with the PC3 tumor.

In 1995, a new immunodeficient mouse model was established, which is a cross of the SCID and non-obese diabetic (NOD) mouse line [140]. This strain is characterized by the functional deficit in natural killer cells, the absence of circulating complement, and defects in the differentiation and function of antigen-presenting cells, meaning that multiple functional deficits of the adaptive and innate immune systems are present. For the study of human PCa cells, such as PC3, DU145, and LNCaP, this model is suitable for both subcutaneous and orthotopic implantation [147]. In another xenograft model or tissue recombinant model, benign or malignant epithelial cells are implanted subcutaneously or under the kidney capsule together with mesenchymal cells in immunosuppressed mice. This model is particularly well adapted to study epithelial-stromal interaction [148, 149]. There is also a xenograft model, whereby human PCa tissue is produced and

injected into a mouse as xenografts. This is a popular choice for therapeutic research. Mouse PCa xenografts from mouse PCa cell lines can be produced in syngeneic, immunocompetent host mice, which plays a major role in immunotherapy research. In addition, it is possible to use mouse xenografts in immunocompetent mice, which is suitable for studying the tumor microenvironment during tumor progression and therapeutic resistance studies [150].

1.2. Imaging modalities for prostate cancer

An increased PSA level and, in the case of abnormalities, a DRE is not specific or sensitive enough to reliably diagnose PCa. Three-quarters of patients with an elevated PSA level (> 4 ng/ml) are not diagnosed with PCa [151]. Ultrasound examination can only be used to a limited degree to detect PCa, as focal lesions occur in only about 11-35% and the tumor is detected in only about 17-57% [152]. A CT scan shows high specificity, however, there are major disadvantages with this imaging modality, including the lack of soft tissue detail and the lack of molecular information [153]. A PET scan is performed with a tracer fluid to locate cancer cells. Tracers are radioactive and very costly. MRI is a superior method to the imaging modalities mentioned above to reliably detect primary prostate lesions and allows detailed images of soft tissue. A PROMIS study showed a significantly higher sensitivity for identifying cancer compared to TRUS-guided biopsies [152].

1.2.1. Magnetic resonance imaging

Magnetic resonance imaging is a non-ionizing imaging modality based on a strong magnetic field and radio waves [63]. It is a non-invasive and low-risk examination technique that is widely used in clinical practice [154]. MRI makes it easier to detect tumors, which produces high spatial and temporal resolution [155-157].

An MRI scan in PCa patients uses an endorectal coil with a phased array coil of moderate to high field strength in the pelvic region [134, 135]. T2-weighted images provide a morphological representation of the prostate in three dimensions. Axial T1-weighted images are used to identify lymph nodes, post-biopsy hemorrhage, and metastases. However, native T1-weighted images of the prostate show a uniform intermediate signal intensity, which means that the zonal anatomy cannot be clearly differentiated.

The MRI works with a very strong magnetic field, which means that it must be ensured that no magnetic objects are introduced into the examination room. Patients with implants, especially those containing iron, should not be examined in an MRI. A rapid change of MRI fields can cause nerve stimulation in the patient. Closed MRI machines can also cause claustrophobia. The

currently most debated risk in MRI is the use of gadolinium-based contrast media, which contain gadolinium chelates (Gd^{3+}).

1.2.1.1. Principles of MRI

Atomic nuclei are composed of protons and neutrons, which rotate around their own axis. Depending on the composition of the atomic nuclei, the nuclei have a nuclei spin (nuclei spin number $\neq 0$), which generates a magnetic moment and induces a local magnetic field with north as well as south poles. When a strong external magnetic field (B_0) is applied, the nucleus aligns itself either parallel or antiparallel to the external field. These properties apply to the nuclei of hydrogen. By placing hydrogen-containing molecules in the B_0 field, two possible energy states can occur:

1- a low energy state, aligned parallel with the magnetic field, or 2- a high energy state, aligned anti-parallel to the magnetic field [154]. By putting the substance in B_0 usually, there would be a small excess of spins in the low energy state [154]. Additionally, to the alignment to B_0 due to the rotation, the nuclei get angular momentum so that they rotate/advance about the axis of B_0 [154]. The rate of rotation about the field direction is the Larmor frequency. This is proportional to the field strength and is described by the Larmor equation: $\omega_0 = \gamma B_0$ (angular frequency of protons = gyromagnetic ratio x field strength) [154]. Nuclei that have spins can be excited in the magnetic field B_0 by applying a high-frequency magnet field B_1 that is perpendicular to B_0 [154].

High-frequency energy is applied in short pulses, each lasting seconds. The absorption of energy by the core causes a transition from higher to lower energy levels and from lower to higher energy levels (relaxation) [154]. Energy originating from the cores generates a voltage that can be detected by a tuned wire coil, amplified, and displayed as a free induction decay. In the absence of continued high-frequency modulation, relaxation processes will bring the system back to thermal equilibrium [154]. Therefore, each nucleus oscillates at a specific frequency when it is within this magnetic field [154]. Making a transition between energy levels depends on the strength of the B_0 magnetic field to which the nuclei are exposed [154]. The application of a high-frequency pulse at resonance frequency produces a free induction decay. To improve the signal-to-noise ratio, several high-frequency pulses are applied to obtain several free-induction decays, which are then averaged [154]. The averaged field induction decay is a time domain signal and can be resolved by mathematical processes (known as Fourier transform) into either an image (MRI) or a frequency spectrum that provides biochemical information [154].

Introduction

Transmitter and receiver coils are placed on the object e.g., animal, human, or phantom. The receiver coil consists of a wire loop that is placed within the area to be examined or lies within the transmitter coil. Phased array coils contain several coils that receive the MR signal simultaneously and independently of an excitation.

There are two types of relaxation (which describes the process by which a nuclear spin returns to thermal equilibrium after absorption), longitudinal stress, and transverse stress, which are described by the time constant T1 or T2, respectively. T1, also known as spin-lattice relaxation, occurs when the longitudinal voltage dissipates energy into the grid. T1 is the time it takes for the system to return to thermal equilibrium at 63% after a high-frequency pulse as an exponential function of time. T1 manipulation can be done by changing the time between high-frequency pulses defined as the repetition time (TR). T1-weighted images appear dark because water and CSF have a long T1 value, 3000-5000 ms. Fat has a short T1 value, 260 ms, and appears bright in the T1 weighted images [154]. Depending on the field strength, the parameters vary or have to be adjusted. T2 describes spin-spin relaxation. Relaxation processes can also redistribute energy to the nuclei within a spin system without losing the entire spin system [154]. When a high-frequency pulse is applied, the nuclei align predominantly along the axis of the applied energy. During relaxation, a dephasing of the nuclear orientation occurs. T2, which is called the transverse relaxation, indicates how fast the spins exchange energy in the XY plane. Diffusion-weighted imaging (DW) is an MR technique that allows quantification of the motion of water molecules. The principle is based on the principles of Brownian motion.

The currently used diagnostic MRI scanners employ cryogenic superconducting magnets in the range of 0.5 Tesla (T) up to 3 T. Cooling of the magnetic field is usually done with liquid helium. Research MRIs use a field strength of 3 T - 11.7 T, resulting in improved signal-to-noise ratio (SNR), higher spectral, spatial, and temporal resolution as well as better quantification [160, 161]. Disadvantages of MRI include magnetic susceptibility, eddy current artifacts, and magnetic field instability [162, 163].

The use of an imaging probe increases the sensitivity and specificity of diagnostic images in MRI by changing the intrinsic properties of tissues that influence basic contrast mechanisms [164]. Imaging probes affect the relaxation times of tissues. Most clinically allowed imaging probes decrease the T1 relaxation time of protons in tissues. Imaging probes affect the relaxation times of tissues and can be administered to the body in different ways: 1- oral, predominantly for imaging of the gastrointestinal tract, or 2- intravenous, for all other body regions. Imaging probes are differentiated by their chemical composition, magnetic properties, bio-distribution, and use [165].

Gadolinium-based imaging probes are currently used for almost all contrast-enhanced MRI examinations, including vascular imaging [166, 167]. A dose of up to 0.1 mmol/kg can be administered for larger vessels, e.g. the aorta. For imaging, the dose is crucial because, for example, if the concentration is too high, there is a T2 shortening effect which means that the brightness through the gadolinium is lower than in the surrounding tissue [168].

1.2.1.2. MRI of prostate cancer

MR imaging techniques are used to identify the stage of the tumor more accurately. Depending on the clinical goal, such as cancer detection, assessment of tumor aggressiveness, or response to therapy, different techniques or combinations may be considered. For imaging of the prostate, a field intensity of 3 T is recommended. The feasibility of 7 T for clinical examinations is currently being tested [169-173].

The standard prostate examination includes multiplanar T1- and T2-weighted imaging and DW-MRI. T1-weighted images of the entire male pelvis are acquired to assess bleeding in the prostate, and metastases in the pelvic bones and lymph nodes. T2-weighted images depict the zonal anatomy of the prostate, which are essential for the detection, localization, and staging of prostate cancer [174, 175].

Both reduced and increased signal intensities can be observed in PCa in the peripheral zone on T2-weighted images [176]. Tumors are also present in the transition zone. One challenge in detecting the tumor reliably is the over- or under-diagnosis of PCa due to confounding factors such as bleeding after a biopsy. Therefore, it is recommended to perform an MRI examination no earlier than 8 weeks post-biopsy [177]. Another confounding factor is chronic prostatitis, which also shows low signal intensity on T2-weighted images, resulting in images being interpreted as false positives [178]. In most cases, a DW-MRI is also performed, which provides data on the physiological properties of water diffusivity [179-181]. Possible losses of signal intensity due to the interaction between water molecules and other molecules can be quantified using apparent diffusion coefficients (ADC). ADC is a measure of average molecular motion and is a low-range PCa [181, 182]. Dynamic contrast-enhanced MRI (DCE-MRI) shows signal intensity changes after intravenous administration of the imaging probe. Most commonly, gadopentetate dimeglumine (Gd-DTPA) is used, which travels from the intravascular space to the interstitial space [183]. Factors such as perfusion, vascularity, and tissue permeability influence signal accumulation. The longitudinal relaxation time, T1 value, of the blood and interstitial water will change the signal intensity in T1-weighted imaging, by the imaging probe. Up to one minute after the imaging probe

injection, several T1-weighted images are taken to visualize the tissue. Quantitative analysis of parameters reflecting tumor vessel permeability, tumor perfusion, and extracellular-extravascular volume fraction follows [183, 184]. Proton magnetic resonance spectroscopic imaging (^1H -MRSI) indicates the distribution of metabolites, such as choline, creatine, citrate, and polyamines, throughout the prostate. In PCa, choline levels increase, which is normally accompanied by a decrease in citrate and polyamines [176].

In summary, the underlying physical principles of MRI are an important aspect in the investigation of PCa and disease in general.

1.3. Molecular MR imaging

Molecular MR imaging is an intensively researched field that enables the visualization of biological and biochemical processes *in vivo* at the molecular level [63]. Cells are constantly reorganizing and in permanent communication with neighboring cells, with continuous changes in biochemical processes in the organism [63]. Imaging at the molecular level makes it possible to visualize specific characteristics in the organism without invasive procedures. For this, it is necessary to use a specific biomarker that is conjugated to a complex between chelate and paramagnetic metal ions like Gd^{3+} or Fe^{3+} and causes a signal change in the MRI. The probes bind to the target based on the induced fit principle and can be visualized in MR by the MR active complex.

Tumors can be easily detected on MRI due to the high spatial resolution [156, 157, 185]. Diagnostic MRI is dominated by Gd^{3+} based imaging probes, such as Magnevist[®], Omniscan[®], Dotarem[®], Gadovist[®], and Multihance[®] [63, 186, 187]. Since the beginning of 2018, Magnevist[®] and Omniscan[®] are no longer allowed to be used, as studies have shown that Gd is released and deposited in the tissue [63, 188]. When imaging probes are used, the longitudinal T1 relaxation rate and transverse T2 relaxation rate of H_2O molecules change [63, 187]. However, Gd-based imaging probes have been criticized for some time because they have been associated with gadolinium deposition in the brain, skin, heart, bone, and kidney after multiple administrations, especially in patients with renal dysfunction [63, 189-195]. Especially linear imaging probes release Gd-ions in the body due to their unstable form [188, 196]. A distinction is also made between ionic and non-ionic imaging probes. Ionicity is related to osmolarity. This factor (linear or macrocyclic; ionic or non-ionic) plays a role in the patient/organism tolerance of the imaging probe [197]. It is important to pay attention to how often a patient gets an imaging probe dose and whether there are pre-existing health conditions that promote deposition of Gd. A better alternative would be to use stable structures so that few to none of the Gd can be deposited into the organism.

At the onset of the disease, and during progression, cells are constantly changing [198-202]. Tumor diseases are a good example, as tumor cells absorb and use different nutrients than healthy tissue [203, 204]. Due to the modified metabolic processes, it is possible to determine the change in the organism by using specific markers in the region of interest. Under these circumstances, the possibility of imaging cellular and molecular characteristics with specific molecular probes in MRI represents a promising alternative to the current clinical practices [205]. Molecular probes can be categorized into two groups: 1- biological targets, such as proteins, and 2- cellular targets, such as macrophages.

1.3.1. Biological targets for molecular imaging

Specific molecular imaging can be used for the early detection, identification, and treatment processes of diseases. Therefore, in disease overexpressed molecules, like receptors, fibers, or enzymes, can be used as a target. By performing high-throughput screenings against these targets, peptide binders can be found and afterward, modified to obtain specific probes [206, 207]. Overexpressed molecules and receptors can ideally function as optimal biomarkers.

A major advantage of using a peptide-based molecular probe is their small size and often good physiological compatibility. Therefore, they can diffuse into extracellular areas and have a fast blood clearance. For MR activity, the peptides are normally bound to a gadolinium (III) complex, which causes a positive signal change in T1-weighted MR images. Based on the tissue, the administration of the Gd-containing imaging probe results in changes/enhancement of the longitudinal relaxation time, as the seven unpaired electrons of the paramagnetic Gd^{3+} have a high longitudinal relaxivity, which can be further enhanced by the correct choice of chelating ligands.

Additionally, to peptide-based probes, peptides can be coupled to a protein carrier. Thereby, the protein carrier uses modified metal ion binding sites for the complexation of gadolinium. The advantage of such a protein carrier is the longer blood retention time and due to the decreased mobility of the gadolinium complex, the T1 relaxivity will be increased [206]. Wei *et al.* modified this imaging probe by adding a gastrin release sequence, which allowed for better targeting [208]. Gastrin-releasing peptide (GRP) binds specifically to the surface receptors of GRPR, which are abundant in PCa [208]. The binding affinity is due to the loop structure of the C-terminus. Experiments were performed in different cell experiments with PCa tumor cells and studied *in vivo* in a xenograft mouse model. 140 mM of imaging probe were injected into the mouse.

Pu *et al.* developed an imaging agent targeting GRPR with a Gd^{3+} binding site (PRoCA1.GRPR) [209]. GRPR is differentially expressed on the surfaces of different diseased cells. The imaging agent

shows a strong binding affinity to GRPR as well as a high relaxivity and a strong Gd^{3+} selectivity towards physiological metal ions. The *in vivo* experiments were performed in a mouse model with PC3 and H441 tumors. Higher signal intensity was achieved after imaging agent administration, using eight times lower compared to the clinical injection dose [209]. Several studies suggest that gastrin-releasing peptides promote tumor growth [210, 211]. GRPR is not only overexpressed in PCa but has also been found to be overexpressed in breast cancer, pancreatic cancer, colorectal cancer, and lung cancer [210]. For molecular imaging, GRPR is a promising target and a good indicator of PCa, which could play an important role in early detection and treatment monitoring. However, the different tumors need to be widely analyzed at a more molecular level, as different GRPR intensities were shown in the two PCa cell lines that Pu *et al.* used in the study.

Another study by Pu *et al.* developed a molecular probe targeting PSMA (protein MRI molecular probe, named ProCA32) [70]. It showed high Gd^{3+} binding affinity and metal selectivity, relaxation ability, and strong PSMA targeting [70]. The molecular probe was investigated in the xenograft tumor mouse model. PSMA is well suited as a target for PCa as it is expressed ten times more than in healthy tissues and is also specific for PCa [70].

Heckl *et al.* developed an intravital and intracellular molecular probe that consists of peptide nucleic acid and a transmembrane carrier peptide conjugated with a c-myc-specific Gd^{3+} complex [212]. The molecular probe was first tested *in vitro* using HeLa cells, and signal intensity was detected in 1.5 T MRI after only 10 min and the maximum was reached after 1 h. For the control group, the non-specific imaging probe, Magnevist[®], was used. After incubation with the specific molecular probe, relaxation increased more than threefold compared with the non-specific probe. Subsequently, the imaging probe could be studied in the rat model, Dunning R-3327. The intravenously administered dose was 0.25 $\mu\text{mol/kg}$ and a maximum was reached after 30 min. A high expression level of c-myc mRNA was confirmed in the cytoplasm of the rat prostate primary tumor [212].

Another molecular probe for imaging is targeted at fibronectin. Fibronectin is highly expressed in malignant PCa and is a feature of the epithelial-mesenchymal transition [213]. Wu *et al.* synthesized a molecular probe targeting the fibrin-fibronectin complex by solid-phase peptide synthesis [214]. It was studied in an orthotopic mouse model and strong signal enhancement was observed after 5 min post-injection with a dose of 0.03 mmol Gd/kg for at least 30 min. Measurements were performed on a Bruker Biospec 7 T MRI scanner, which is specifically designed for small animals. The control group received a non-specific imaging probe, KAREC-dL-(DOTA-Gd)₄,

at the same dose. The fibronectin molecular probe shows high water solubility, high relaxation, small size, tumor specificity, and strong signal enhancement [214].

Tan *et al.* also modified a molecular probe targeting the fibrin-fibronectin complex based on the cyclic peptide CLT1 (CGIIQKNEC) [215]. It contains the nanoglobular Gd-DOTA monoamide conjugate, CLT1-G2-(Gd-DOTA) [215]. Since the size of the probe is very small, it can diffuse better into tumor tissue. The specific binding of the CLT1 peptide was investigated in an orthotopic tumor mouse model. A dose of 30 $\mu\text{mol Gd/kg}$ was used. The specific binding of the molecular probe could be shown in this study.

Four peptides, GVK, IGK, SGV, and ZD2 have been identified that are specific for extra domain B fibronectin (EDB-FN) for tumor targeting and can be used for molecular imaging as peptide-Gd-DOTA conjugates [216]. The four macrocyclic peptide-Gd-DOTA conjugates were investigated in a prostate cancer xenograft mouse model. All synthesized molecular probes resulted in tumor contrast enhancement in MR imaging [216]. They showed high relaxation and high water solubility [216]. EDB-FN-specific molecular probes may become an important component in the identification of aggressive tumors, but this is also a limitation [63].

1.3.2. Macrophage marker for molecular imaging

Magnetic iron-oxide nanoparticles (IONPs) demonstrate a unique magnetic characteristic that can be used in a variety of biomedical applications, such as drug administration [217], magnetic hyperthermia [218, 219], magnetic particle imaging [220], and also in MRI [221-225]. The particle size is key for the magnetic property of IONPs, which results from the magnetic domain structure [223, 226]. Superparamagnetic iron-oxide nanoparticles (SPION) are magnetic iron particles and have a size of 1-100 nm [227-229]. SPIONs exhibit no remanent magnetization without an external magnetic field at room temperature. SPIONs are very popular as iron-oxide-based T2 molecular probes due to their relatively good biocompatibility [230-232]. In the diagnosis or tumor treatment, SPIONs are used as MRI imaging probe in the clinic. In most cases, SPION imaging probes act as negative imaging probe because the accumulation of iron results in hypointense contrast on MRI. Following intravenous injection, the molecular probe enters the bloodstream and the particles are phagocytosed by macrophages [233]. SPIONs, in contrast to Gd-containing imaging probes, shorten the relaxation time of T1- and T2-weighted images [234].

Bates *et al.* linked a commercially available superparamagnetic iron-oxide-containing molecular probe, MIRB- Molday ION Rhodamine-B carboxyl, to a deimmunized mouse monoclonal antibody, muJ591: muJ591:MIRB [235], targeting PSMA. The experiments have only been performed *in vitro*

up to now. In addition to flow cytometry and immunofluorescence, inductively coupled plasma atomic emission spectrometry (ICP-AES) showed that the modified molecular probe had a loading concentration of 1958 ± 611 (n=8) elemental iron per antibody, which was covalently bound. The results indicate specific binding of the molecular probe to PSMA-expressing cells. However, *in vivo* experiments in animal models are needed, to assess the feasibility of this approach.

The nano pharmaceutical ferumoxytol was modified for use in PCa so that it binds specifically to PSMA [236]. This created a cyclic PSMA-targeting peptide, allowing the functional state of the androgen receptor to be assessed by MRI and used therapeutically [236]. The experiments were performed *in vitro* in cell experiments and subsequently, the nano pharmaceutical was investigated for its therapeutic potential in the mouse xenograft model (*in vivo*) [236].

In the study by Zhu *et al.*, a polypeptide CQKHHNYLC-SPION molecular probe was conjugated, which binds specifically to PSMA [237]. The *in vitro* experiments showed that LNCaP cells took up more polypeptide SPIONs than the reference cells. The *in vivo* experiments in the tumor-induced mouse model showed a significant decrease in T2 tumor signal intensity. This observation could be confirmed in histological examinations.

Biocompatible magnetic iron-oxide nanoparticles (MNPs) can also be modified to obtain better contrast on MRI for PCa. Tse *et al.* developed an MNP-J591 molecular probe [238]. J591 is an antibody against an extracellular epitope of PSMA. In both *in vitro* cell experiments and orthotopic tumor-bearing mice, the conjugate was able to enhance the magnetic resonance contrast of tumors [238]. A non-targeting MNP was used as a reference. Ultimately, this study demonstrates the potential of improving MRI signals in the detection/localization of PCa using specific conjugated MNPs.

2. Aims and Objectives of the Thesis

This thesis aims to evaluate a murine *in vivo* xenograft prostate cancer model via molecular magnetic resonance imaging by testing the following hypotheses:

Hypothesis 1: An elastin-specific molecular probe enables the diagnosis and characterization of different tumor volumes of prostate cancer in a mouse model.

Hypothesis 2: A superparamagnetic iron-oxide probe allows the visualization of different tumor volumes of prostate cancer in a mouse model.

3. Publication I

Title: Visualization and Quantification of the Extracellular Matrix in Prostate Cancer Using an Elastin Specific Molecular Probe

Authors: Avan Kader, Julia Brangsch, Carolin Reimann, Jan O. Kaufmann, Dilyana B. Mangarova, Jana Moeckel, Lisa C. Adams, Jing Zhao, Jessica Saatz, Heike Traub, Rebecca Buchholz, Uwe Karst, Bernd Hamm, Marcus R. Makowski

Year: 2021

Journal: Biology

Impact factor: 5.079

DOI: <https://doi.org/10.3390/biology10111217>

Authors' contribution: I was responsible for the conception and design of the study. I developed the theory and the experimental design. I performed animal experiments, MRI examinations, as well as histological analyses. I wrote the manuscript independently. Each author discussed the results and contributed to the final version of the publication. A detailed list of the contributions of the other authors can be found in the published version of the paper.

Article

Visualization and Quantification of the Extracellular Matrix in Prostate Cancer Using an Elastin Specific Molecular Probe

Avan Kader ^{1,2,*}, Julia Brangsch ¹, Carolin Reimann ¹, Jan O. Kaufmann ^{1,3,4}, Dilyana B. Mangarova ^{1,5}, Jana Moeckel ¹, Lisa C. Adams ¹, Jing Zhao ¹, Jessica Saatz ⁶, Heike Traub ⁶, Rebecca Buchholz ⁷, Uwe Karst ⁷, Bernd Hamm ¹ and Marcus R. Makowski ^{1,8,9}

- ¹ Department of Radiology, Institute of Integrative Neuroanatomy, Charité—Universitätsmedizin Berlin, Corporate Member of Freie Universität Berlin, Humboldt-Universität zu Berlin, and Berlin Institute of Health, Charitéplatz 1, 10117 Berlin, Germany; julia.brangsch@charite.de (J.B.); carolinreimann1990@web.de (C.R.); jan-ole.kaufmann@charite.de (J.O.K.); dilyana.mangarova@charite.de (D.B.M.); jana.moeckel@charite.de (J.M.); lisa.adams@charite.de (L.C.A.); jing.zhao@charite.de (J.Z.); bernd.hamm@charite.de (B.H.); marcus.makowski@tum.de (M.R.M.)
 - ² Department of Biology, Chemistry and Pharmacy, Institute of Biology, Freie Universität Berlin, Königin-Luise-Str. 1-3, 14195 Berlin, Germany
 - ³ Division 1.5 Protein Analysis, Bundesanstalt für Materialforschung und-Prüfung (BAM), Richard-Willstätter-Str. 11, 12489 Berlin, Germany
 - ⁴ Department of Chemistry, Humboldt-Universität zu Berlin, Brook-Taylor-Str. 2, 12489 Berlin, Germany
 - ⁵ Department of Veterinary Medicine, Institute of Veterinary Pathology, Freie Universität Berlin, Robert-von-Ostertag-Str. 15, Building 12, 14163 Berlin, Germany
 - ⁶ Division 1.1 Inorganic Trace Analysis, Bundesanstalt für Materialforschung und-Prüfung (BAM), Richard-Willstätter-Str. 11, 12489 Berlin, Germany; jessica.saatz@bam.de (J.S.); heike.traub@bam.de (H.T.)
 - ⁷ Institute of Inorganic and Analytical Chemistry, Westfälische Wilhelms-Universität Münster, 48419 Münster, Germany; rebecca.buchholz@uni-muenster.de (R.B.); uk@uni-muenster.de (U.K.)
 - ⁸ School of Biomedical Engineering and Imaging Sciences, King's College London, St Thomas' Hospital Westminster Bridge Road, London SE1 7EH, UK
 - ⁹ Department of Diagnostic and Interventional Radiology, Technical University of Munich, Ismaninger Str. 22, 81675 Munich, Germany
- * Correspondence: avan.kader@charite.de



Citation: Kader, A.; Brangsch, J.; Reimann, C.; Kaufmann, J.O.; Mangarova, D.B.; Moeckel, J.; Adams, L.C.; Zhao, J.; Saatz, J.; Traub, H.; et al. Visualization and Quantification of the Extracellular Matrix in Prostate Cancer Using an Elastin Specific Molecular Probe. *Biology* **2021**, *10*, 1217. <https://doi.org/10.3390/biology10111217>

Academic Editor: Guo-Chang Fan

Received: 29 September 2021

Accepted: 18 November 2021

Published: 22 November 2021

Publisher's Note: MDPI stays neutral with regard to jurisdictional claims in published maps and institutional affiliations.



Copyright: © 2021 by the authors. Licensee MDPI, Basel, Switzerland. This article is an open access article distributed under the terms and conditions of the Creative Commons Attribution (CC BY) license (<https://creativecommons.org/licenses/by/4.0/>).

Simple Summary: One of the most commonly diagnosed cancers in men is prostate cancer (PCa). Understanding tumor progression can help diagnose and treat the disease at an early stage. Components of the extracellular matrix (ECM) play a key role in the development and progression of PCa. Elastin is an essential component of the ECM and constantly changes during tumor development. This article visualizes and quantifies elastin in magnetic resonance imaging (MRI) using a small molecule probe. Results were correlated with histological examinations. Using an elastin-specific molecular probe, we were able to make predictions about the cellular structure in relation to elastin and thus draw conclusions about the size of the tumor, with smaller tumors having a higher elastin content than larger tumors.

Abstract: Human prostate cancer (PCa) is a type of malignancy and one of the most frequently diagnosed cancers in men. Elastin is an important component of the extracellular matrix and is involved in the structure and organization of prostate tissue. The present study examined prostate cancer in a xenograft mouse model using an elastin-specific molecular probe for magnetic resonance molecular imaging. Two different tumor sizes (500 mm³ and 1000 mm³) were compared and analyzed by MRI in vivo and histologically and analytically ex vivo. The T1-weighted sequence was used in a clinical 3-T scanner to calculate the relative contrast enhancement before and after probe administration. Our results show that the use of an elastin-specific probe enables better discrimination between tumors and surrounding healthy tissue. Furthermore, specific binding of the probe to elastin fibers was confirmed by histological examination and laser ablation–inductively coupled plasma–mass spectrometry (LA-ICP-MS). Smaller tumors showed significantly higher signal intensity ($p > 0.001$), which correlates with the higher proportion of elastin fibers in the histological evaluation than in larger tumors. A strong correlation was seen between relative enhancement (RE)

and Elastica–van Gieson staining ($R^2 = 0.88$). RE was related to inductively coupled plasma–mass spectrometry data for Gd and showed a correlation ($R^2 = 0.78$). Thus, molecular MRI could become a novel quantitative tool for the early evaluation and detection of PCa.

Keywords: magnetic resonance imaging; molecular imaging; prostate cancer

1. Introduction

Prostate cancer (PCa) accounts for one in five cancer diagnoses in men, making it one of the most commonly diagnosed carcinomas in men in the Western world [1]. It can be a highly malignant tumor disease, and represents one of the most common fatal cancers in men [1]. The causes of the disease are yet not fully understood. Risk factors include age, ethnic origin, geographical location, and genetic predisposition [2–5]. In the last few years, both the diagnosis and treatment of PCa have improved due to medical advances.

Early-stage prostate-specific antigen (PSA) screening is considered practical for decision-making and treatment in PCa [2]. The laboratory-chemical survey determination of the PSA level is well established in Western countries, but this method also shows significant limitations. Due to its relatively low specificity and a low sensitivity, it leads to many false positive diagnoses [6,7]. As a result, many patients undergo unnecessary prostate biopsy [7]. In patients with a normal PSA level, PCa could be diagnosed in 30% of cases, with 10% being assigned to aggressive PCa [6]. The PSA value therefore does not necessarily provide any information about the aggressiveness of the tumor. Other factors can also affect PSA level, such as bacterial prostatitis and acute urinary retention [8]. PSA screening also leads to over-diagnosis of PCa and thus initiates unnecessary surgical procedures to collect tissue samples [9].

Another diagnostic option is transrectal ultrasound (TRUS) [10], which is now well established in clinical practice. TRUS can help determine the volume of the prostate and is used as a supplementary diagnostic test.

An indispensable method for the diagnosis of PCa is magnetic resonance imaging (MRI). Diffusion-weighted apparent diffusion coefficient (ADC) imaging, T2-weighted imaging, and dynamic intravenous contrast-enhanced (DCE) imaging with unspiced contrast agents are among the standard MRI examinations in PCa, referred to as multiparametric MRI (mpMRI) [11,12]. Some of the advantages of MRI are the high-resolution spatial imaging of tissue with strong soft tissue contrast, the quantitative imaging technique, and the lack of invasiveness and radiation. mpMRI has a high sensitivity and specificity, but it has a low positive predictive value (PPV) [13]. The Prostate Imaging Reporting and Data System (PI-RADS) helps to detect PCa in a standardized form. The main challenge is the different interpretation of the PI-RADS results by clinicians and medical staff [13]. PCa mpMRI diagnosis must finally be verified by biopsy. Therefore, it is necessary to develop a non-invasive screening method with high specificity.

To improve MRI contrast, the paramagnetic lanthanide metal ion gadolinium (III) (Gd^{3+}) can be used in a complex with organic chelates, like the macrocyclic DOTA (2,2',2'',2'''-(1,4,7,10-Tetraazacyclododecane-1,4,7,10-tetrayl)tetraacetic acid) or the linear DTPA (2,2',2'',2'''-[[[(Carboxymethyl)azanediyl]bis(ethane-2,1-diylnitrilo)]tetraacetic acid) as contrast media. Thereby, the unpaired electrons in the Gd-ion will shorten the T1 relaxivity of the neighboring water protons and thus, the signal intensity of the T₁-weighted image will be increased [14].

To further improve tissue differentiation, molecular probes could be used as opposed to the currently available unspecific extracellular Gd-based contrast agents [15]. In addition, molecular imaging could be used as an added tool to current diagnostic techniques.

A possibility to use appropriate small molecule biomarkers for the detection of malignant diseases would be to target extracellular matrix (ECM) components. These can be coupled with MRI-compatible elements. The ECM architecture plays a main role during

the development and progression of PCa [16]. Palumbo et al. showed strong stimulation of the proliferation and migration of tumor cells (LNCaP) by the ECM, but also inhibition of apoptosis and deregulation of the expression of several genes [16].

The main matrix macromolecule components are elastin, collagen, fibronectin, laminin, and proteoglycan [17–19]. The interaction between tumor cells and elastic fibers is controlled by a 67 kDa receptor [20,21]. Although the signal mediation of the receptor in tumor cells is not yet fully elucidated, a different extensive binding of tumor cell lines to elastin has been observed in Lewis lung carcinoma cells [22]. Tumor cells are able to express, adhere, degrade, and migrate elastin proteins [23]. Lysyl oxidase, a copper-dependent aminodase, promotes the cross-linking of collagen and elastin in tissue and is responsible for the activation of the elastin promoters [24,25]. This is a determining factor in the stiffness and structural stability of ECM [24]. An interaction between the tumor cells and the ECM protein elastin is mediated by two elastin-binding proteins (S-gal and galectin-3) and two laminin receptors [23].

The expression of elastin-binding proteins is strongly related to the metastatic potential of the tumor [23]. One possible explanation is that cancer cells are able to synthesize elastin and express lysyl oxidase [23]. Calderón et al. showed that PCa contains more elastic fibers than normal tissue [26]. Elastin fibers are implicated in tumor invasion and metastasis, cell proliferation, adhesion, apoptosis, and angiogenesis [26–28]. Finally, elastin represents a novel promising molecular biomarker also in the field of cardiovascular diseases [29,30]. Additionally, hepatic cancer [31] could be evaluated using an elastin-specific MRI molecular probe.

Despite the advances in the diagnosis of PCa over the course of time, further studies are needed to clarify the onset and mechanism of PCa progression.

We therefore analyzed the role of elastin in conjunction with molecular MR imaging in a xenograft mouse model, comparing two different tumor sizes. This study aimed to use a low-molecular elastin-specific probe in MRI examinations and, thus, to obtain information on changes in the ECM during prostate cancer development for a better differentiation between tumor tissue and healthy tissue.

2. Materials and Methods

2.1. Cell Culture

Human PC3 cells were obtained from ATCC[®] CRL-1435[™] (Manassas, VA, USA) and cultured in Roswell Park Memorial Institute (RPMI) 1640 Medium (Gibco[™], Thermo Fischer Scientific, Waltham, MA, USA) supplemented with 10% fetal calf serum (FCS) (Gibco[™], Thermo Fischer Scientific, Waltham, MA, USA). Cells were cultured in 150 cm² tissue culture flasks until they reached about 80% confluence. Cells were washed with phosphate buffered saline (PBS) (Gibco[™], Thermo Fischer Scientific, Waltham, MA, USA), trypsinized, and subsequently re-suspended in 1 mL RPMI-medium and counted with 0.4% Tryptan blue solution (Gibco[™], Thermo Fischer Scientific, Waltham, MA, USA).

2.2. Xenograft Mouse Model

This study was performed corresponding to the local guidelines and provisions for the implementation of the Animal Welfare Act and the regulations of the Federation of Laboratory Animal Science Associations (FELASA). This animal study was approved by the regulatory authority of the Regional Office for Health and Social Affairs Berlin (LAGeSo) (G0094/19). Male, eight-week-old SCID-mice (CB17/1cr-Prkdcscid/1cr1coCr1) were obtained from Charles River Laboratories (Sulzfeld, Germany) (N = 28). The animals were randomly assigned to two different groups (n = 14).

For anesthesia, the mice were intraperitoneally injected with medetomidin (500 µg/kg), midazolam (5 mg/kg), and fentanyl (50 µg/kg). Cell suspension with 2×10^6 PC3-cells was injected subcutaneously (s.c.) in the area of the right scapula. Anesthesia was subsequently antagonized with atipamezol (750 µg/kg), flumazenil (0.5 mg/kg), and naloxon (1200 µg/kg).

MR imaging was performed on a tumor size of 500 mm³ (n = 14) or 1000 mm³ (n = 14). The size of the tumor was determined using calipers. Following MRI, mice were euthanized and tumor tissue was removed for ex vivo examination.

2.3. In Vivo MRI

MR imaging was performed using a 3.0 Tesla MR scanner (MAGNETOM Lumina, Siemens, Erlangen, Germany) and a 4-channel receive-coil array for mouse body applications (mouse scapula array, P-H04LE-030, Version1, Rapid Biomedical GmbH, Germany). Following s.c. anesthesia as described above, mice were positioned on the MRI patient table in a prone position. A venous access through the tail vein was established for administration of the contrast agent during the MR imaging. The body temperature (37 °C) was monitored with the use of an MR-compatible heating system (Model 1025, SA Instruments Inc, Stony Brook, NY, USA) to avoid rapid cooling.

2.4. Elastin-Specific Contrast Agent for the MRI

A contrast agent that specifically binds to elastin was used for the experiments (ESMA; Lantheus Medical Imaging, North Billerica, MA, USA). It is a low-molecular-weight gadolinium-based contrast agent with a molecular mass of 856 g/mol [30]. The highest binding is achieved after 30 to 45 min [30,32]. The longitudinal relaxivity of $4.68 \pm 0.13 \text{ mM}^{-1}\text{s}^{-1}$ and $8.65 \pm 0.42 \text{ mM}^{-1}\text{s}^{-1}$ [30,32] is known. The contrast agent was administered intravenously via the tail vein in a clinical dose of 0.2 mmol/kg.

2.5. Elastin Imaging Using T1 Weighted Sequences

MR imaging was realized with a 3.0 Tesla MR scanner. The mice were imaged in prone position with a 4-channel receive-coil array for mouse body applications. For the localization of the tumor, a low-resolution three-dimensional localizer scan was used, which was performed in sagittal, coronal, and transverse orientation with the following parameters: field-of-view (FOV) = 280 × 280 mm, matrix = 320, slice thickness = 1.5 mm, repetition time (TR) = 11.0 ms, echo time (TE) = 5.39 ms, flip angle = 20°, and slices = 10. Anatomic images were captured using a T2-weighted sequence with the following parameters: FOV = 150 mm, matrix = 201, slice thickness = 1.2 mm, TR = 3200.0 ms, TE = 77.0 ms, flip angle = 140°, and slices = 25. To visualize the gadolinium-based contrast agent, a T1-weighted sequence was performed with the following parameters: FOV = 70 mm, matrix = 131, slice thickness = 0.4 mm, TR = 833.8 ms, TE = 6.34 ms, flip angle = 30°, and slices = 30.

2.6. MRI Measurements

MR images were analyzed using Visage 7.1 (Version 7.1, Visage Imaging, Germany). The T1-weighted images were compared before and after the administration of the contrast agent (signal intensity = *SI*). For relative enhancement (*RE*) assessment, 2D regions of interest (ROIs) were drawn around the respective areas in pre-contrast and post-contrast MR images. The following formula was used to calculate the relative enhancement (*RE*):

$$RE = \frac{(SI_{postcontrast} - SI_{precontrast})}{SI_{precontrast}}$$

2.7. Competition Experiment

Three mice were used for the competition experiment (n = 3). After a tumor size of 1000 mm³ was reached, the animals were anesthetized and examined in an MRI (MAGNETOM Lumina, Siemens, Erlangen, Germany). On day one, imaging without a contrast agent was followed by an intravenous injection of the elastin-specific contrast agent (0.2 mmol/kg). Additional MRI images were acquired as described above (*Elastin imaging using T1 weighted sequences*) and the animals were then antagonized. On day two, following a native MRI scan, a 5-fold higher dose of an elastin-specific europium-coupled contrast

agent was administered through the tail vein. After this imaging, the Gd-containing elastin-specific contrast agent was administered and imaged in an MRI. The data obtained were compared for signal changes.

2.8. Histological Analysis

Frozen samples were cut into 9 μm -thick serial sections at $-20\text{ }^{\circ}\text{C}$. The sections were then fixed with cold acetone ($\geq 99\%$, Fisher Scientific, Hampton, VA, USA) for 6 min at $-20\text{ }^{\circ}\text{C}$. Miller's Elastica-van Gieson-stain (EvG) was performed. EvG was used to visualize elastic fibers. In addition, immunofluorescence staining was conducted using an anti-elastin antibody (Rabbit anti-Mouse pAb Elastin, abcam[®], Cambridge, United Kingdom) that was diluted 1:100 with Dako REAL[™] Antibody Diluent (DAKO, Glostrup Denmark), and incubated overnight at $4\text{ }^{\circ}\text{C}$. The sections were washed three times with PBS (pH = 7.4), followed by a 1 h incubation with the secondary antibody (1:200, donkey anti-rabbit IgG, Invitrogen, Carlsbad, CA, USA). The samples were washed again three times with PBS and covered with DAPI staining solution (ROTI[®] Mount FluorCare DAPI, Carl Roth, Karlsruhe, Germany). Last, the sections were analyzed using a Keyence microscope (BZ-x800 Series, Osaka Prefecture, Japan).

2.9. Quantification of the EvG Stain and Immunofluorescence

The quantification of the staining area of the EvG and immunofluorescence sections was measured with the image analysis software BZ-X800 Analyzer (Keyence, Osaka prefecture, Japan). Three representative areas (two different peripheral areas and one central region) were analyzed for each probe. The mean value was calculated in each case. First, the entire region of interest was marked. Consecutively, all elastic fibers were identified and the relation of the elastic fibers to the entire marked tumor region was calculated using marked pixels.

2.10. Laser Ablation-Inductively Coupled Plasma-Mass Spectroscopy (LA-ICP-MS)

LA-ICP-MS was performed for localization of gadolinium (Gd) in the tumor tissue ($n = 3$ per group). Tumor samples were cut into 9 μm cryosections at $-20\text{ }^{\circ}\text{C}$ and mounted on SuperFrost Plus adhesion slides (Thermo Scientific, Waltham, MA, USA).

The analysis was performed by continuously scanning the thin sections and transport of the aerosol via He-gas flow to the ICP-MS. Two different LA-ICP-MS systems were used, which are described in the Supplementary Materials. Matrix matched gel standards were used for drift control and calibration of ^{158}Gd .

2.11. Inductively Coupled Plasma-Mass Spectrometry (ICP-MS)

ICP-MS was used to determine total gadolinium concentrations in tumor samples. A piece of the tumor sample was prepared ($n = 5$ per group) and dried under a vacuum atmosphere (vacuum pumping unit, vacubrand[®], Wertheim, Germany). One mL of 66% nitric acid was added to each sample and incubated at room temperature until the tissue was completely dissolved. Deionized water was then added to each sample. Digested samples were diluted in 1% HNO_3 sub-boiling (s.b.) and analyzed with an iCAP Qc ICP quadrupole mass spectrometer (Thermo Fisher Scientific, Bremen, Germany) in combination with the autosampler 4DXF-73A (ESI Elemental Service & Instruments GmbH, Mainz, Germany) using a 200 μL PFA nebulizer and a cyclonic spray chamber (see Table 1 for more details). Calibration was carried out using diluted Gadolinium ICP Standard CertiPUR (Merck KGaA, Darmstadt, Germany) and using rhodium as the internal standard. More details can be found in the Supplementary Materials.

Table 1. Experimental parameters of iCAP Qc.

Parameter	Value
Power (W)	1550
Nebulizer gas flow rate (L min ⁻¹)	1.08
Aux gas flow rate (L min ⁻¹)	0.65
Cool gas flow rate (L min ⁻¹)	14
Sample flow rate (mL min ⁻¹)	0.40
Dwell time [ms]	0.01
Isotopes monitored	¹⁰³ Rh, ¹⁵⁵ Gd, ¹⁵⁶ Gd, ¹⁵⁷ Gd, ¹⁵⁸ Gd, ¹⁶⁰ Gd,

2.12. Western Blot

For protein isolation from the tissue, a tumor piece was first homogenized in RIPA buffer (n = 3 per group). For this purpose, 50 mM Tris-HCl (Carl Roth GmbH, Karlsruhe, Germany), 150 mM NaCl (Carl Roth GmbH, Karlsruhe, Germany), 0.1% SDS (Carl Roth GmbH, Karlsruhe, Germany), 1% sodium deoxycholate (Carl Roth GmbH, Karlsruhe, Germany), and 1% Triton X-100 (Merck, Darmstadt, Germany) were mixed with protease inhibitor I and protease inhibitor II (Thermo Fisher Scientific, Waltham, MA, USA). The samples were shaken shortly and shaken for 2 h at 4 °C. This was followed by centrifugation at 12,000 rpm for 20 min at 4 °C. Samples were filtered using tip filters (1 µm, 0.45 µm, 0.1 µm). The sample concentration was determined using the BC assay method (Pierce™ BCA Protein Assay Kit, Thermo Fisher Scientific, Waltham, MA, USA). The manufacturer's protocol was used. The same protein amount (50 µg) was loaded into the wells of the gel under unreduced conditions (SERVAGel™ TG 8% PRiME™, Heidelberg, Germany) and separated in the running gel system (SERVA™ Heidelberg, Germany) at a voltage of 70 V for 60 min and then at 160 V for 60 min in running buffer (250 mM TrisBase (Carl Roth GmbH, Karlsruhe, Germany), 1.92 M glycine (Carl Roth GmbH, Karlsruhe, Germany), and 1% SDS (Carl Roth GmbH, Karlsruhe, Germany)). Subsequently, the proteins were transferred from sodium dodecyl sulphate (SDS) gel to a nitrocellulose membrane (Trans-Blot® Turbo™ RTA Mini PVDF Transfer Kit, Bio-Rad Laboratories, Hercules, CA, USA). The blot system Trans-Blot® Turbo™ (Bio-Rad, Laboratories, Hercules, CA, USA) was used. A 5% skim milk powder (Carl Roth GmbH, Karlsruhe, Germany) in 0.05% PBS-Tween20 (PBS-T) (Carl Roth GmbH, Karlsruhe, Germany) solution was used to block non-specific antibody binding. Incubation was performed at room temperature for 1 h. Blots were incubated with a mouse monoclonal anti-elastin antibody (sc-166543, Santa Cruz Biotechnology, Dallas, TX, USA) diluted 1:1000 in 5% milk solution overnight at 4 °C. After washing the membrane three times with PBS-T, the blots were incubated with HRP-coupled mouse IgGκlight chain binding protein diluted 1:5000 in PBS-T for 60 min. The band was detected using the membrane substrate (SeramunBlau® prec, Seramun Diagnostica GmbH, Heidesee, Germany). GAPDH (Invitrogen, Carlsbad, CA, USA) was used for charge control.

The intensity of the bands was measured with the software Image J (ImageJ software, Version 1.53).

2.13. Statistical Analysis

A mean bet was calculated and presented from all the data. The significance was compared by unpaired and bilateral t-test analysis and significance was shown at $p < 0.05$. Statistics were performed with Microsoft Excel.

3. Results

In this study, a gadolinium-based elastin-specific probe was used to examine ECM changes during PCa development. Two different tumor sizes were examined. For a detailed study setup please see Figure 1.

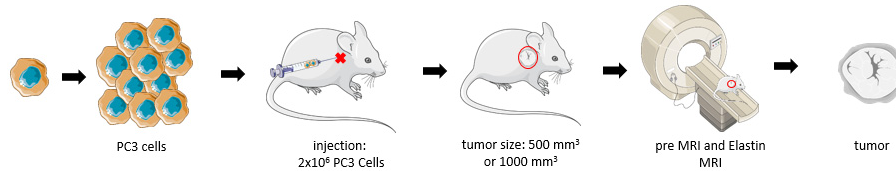


Figure 1. Overview of the experiment. Human PC3 cells were cultured in a cell-culture flask. A total of 2×10^6 cells were subcutaneously injected into male SCID mice. Two different tumor sizes were achieved: 500 mm^3 and 1000 mm^3 . After obtaining the desired tumor size, MR imaging was performed using an elastin-specific contrast agent. Tumor tissue was excised for ex vivo analysis.

All animals developed a tumor. Tumor growth at the same injection time was heterogeneous. The final size of the tumor was determined by daily tumor measurement. The final tumor size of 1000 mm^3 was reached after 36 to 50 days. In the other group, which developed a tumor volume of 500 mm^3 , the target volume was reached after 30 and 64 days. One animal had to be withdrawn from the trial early because of poor general condition ($n = 1$) (was replaced by another mouse).

3.1. Molecular Characterization in T1-Weighted MR Imaging Using Gd-Based Elastin-Specific Contrast Agent

The intravenous administration of the elastin-specific contrast agent resulted in a significant MR signal increase ($p \leq 0.001$) in the area of the subcutaneous tumor in all examined mice. Figure 3B shows a pre-contrast image and Figure 3C shows an image with a contrast medium. A good difference between the two groups can already be seen here. Mice with a tumor size of 1000 mm^3 showed a twofold increased SI, whereas mice with 500 mm^3 tumors showed an even higher (threefold) increased SI (Figure 2A). In the group with a tumor volume of 1000 mm^3 , the SI was 3037 after contrast agent administration (pre-contrast SI of 897) ($p \leq 0.001$). In mice with a tumor size of 500 mm^3 , after application of the elastin-specific contrast agent an SI of 3819 was determined (pre-contrast SI of 907) ($p \leq 0.001$).

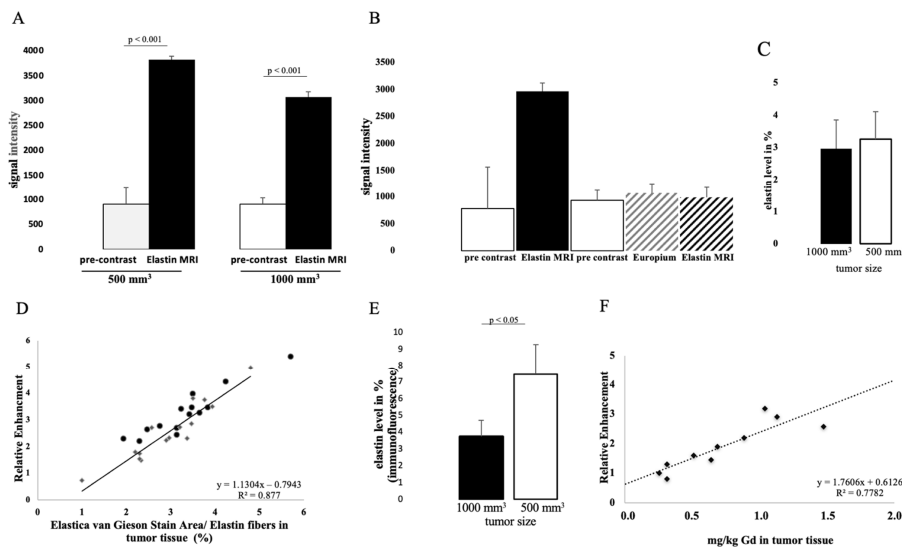


Figure 2. In vivo molecular MR imaging evaluation and quantification of prostate cancer using an elastin-specific contrast

agent. (A) MRI measurements show the evaluation of MRI images (T1-weighted sequence) before and after contrast agent administration in two tumor volumes (1000 mm³ and 500 mm³). A total of 14 animals were examined per group (n = 14). After the elastin-specific contrast agent was administered, the value increased to an RE of 3037 (1000 mm³) and 3819 (500 mm³). The data are significant ($p \leq 0.001$). (B) A competition experiment was performed to show the specific binding of the elastin-specific contrast agent. Three mice were used for this experiment (n = 3). On day 1, images were taken before and after the elastin-specific contrast agent administration. After 24 h (day 2) the animals were examined again. First a pre-contrast image was taken, then an elastin-specific probe with europium was administered (instead of Gd³⁺, it was conjugated with europium), and finally the elastin-specific contrast agent was applied. There was very little to no signal change. The data therefore show specific binding of the elastin-specific contrast agent. (C) Elastin levels of n = 14 animals per group were analyzed by histology. (D) The dot plot shows the correlation between MRI data (relative enhancement) and histological data. The Elastica-van Gieson stain was used to stain elastin fibers in the tumor tissue. The R-squared value is 0.88. (E) Elastin levels of n = 4 animals per group were analyzed by immunofluorescence. The data are significant ($p \leq 0.05$). (F) shows the correlation between MRI data and Gd content in tumor tissue measured with ICP-MS. The R-squared value is 0.78.

The specific binding of the contrast agent was demonstrated by a competition experiment. The administration of a europium-coupled elastin-specific probe did not provide sufficient signal enhancement, as shown in Figure 2B. These data from the previous day (pre-scan and after elastin-specific contrast agent administration) were compared with the second-day data (pre-scan, europium-coupled probe and elastin-specific contrast agent). On the first day, an SI of around 3000 was obtained after elastin-specific contrast agent administration. On the second day, the data from native imaging, the europium-coupled probe, and the elastin-specific contrast agent showed no change in RE.

To show signal enhancement within a mouse, a fusion map was created (Figure 3D) that shows the SI between the T2 and T1 sequences after contrast administration in the same mouse.

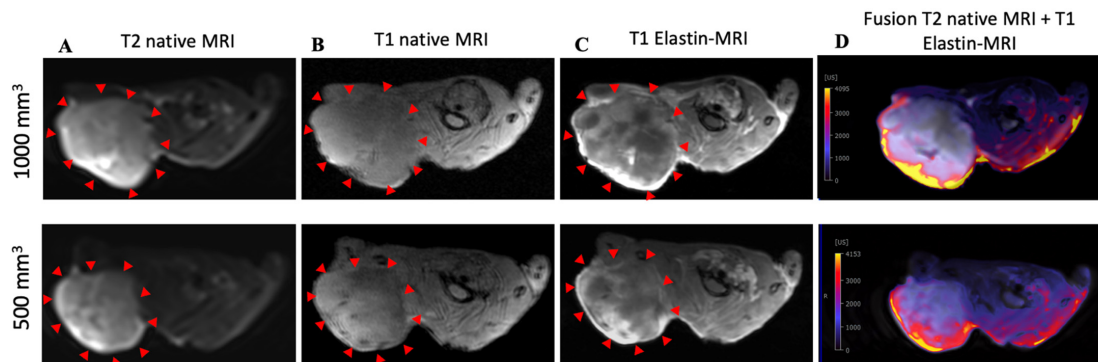


Figure 3. MRI and histological images of prostate cancer: histological characterization of elastin distribution in 1000 mm³ and 500 mm³ PC3 tumors. (A) shows a representative native MRI image of a T2-weighted sequence from the scapula area of a mouse that developed a tumor with a volume of 1000 mm³ (top) and 500 mm³ (bottom). The red arrows indicate the tumor. (B) shows a representative native MRI image of a T1-weighted sequence from the scapula area of a SCID mouse that developed a tumor volume of 1000 mm³ (top) and 500 mm³ (bottom). (C) shows an MRI image of a T1-weighted sequence with administration of the elastin-specific contrast agent. A signal change in the tumor area after contrast agent administration is visible. The red arrows mark the total area of the tumor. In this region there are clear white/bright areas showing the signal change from the previous image (1000 mm³ (top) and 500 mm³ (bottom)). (D) shows a fusion of a native T2-weighted sequence and a T1-weighted sequence after administration of the elastin-specific contrast agent in the same mouse (1000 mm³ (top) and 500 mm³ (bottom)).

3.2. Detection of Elastin Fibers in Tumor Tissue with Histological Analysis

In both tumor sizes, elastin fibers were observed in the entire tumor tissue, as shown in Figure 4A. The elastin fibers were dyed blue to purple. To determine the elastin content of a sample, three areas were selected for each slide and the percentage of elastin content was determined with the analyzer. The evaluation showed a difference between the two groups: Fewer elastic fibers were detected in 1000 mm³ tumors compared to 500 mm³. The mean value of n = 14 was 3.3% (σ = 0.9) in the 500 mm³ and 3.0 % (σ = 0.9) in the 1000 mm³ tumors (n = 14) (Figure 2C). In addition, the detected values (percentage of elastin) of each tumor strongly correlated with the RE data of in vivo MRI imaging (T1-weighted MR sequences) (Figure 2D, $y = 1.1304x - 0.7943$, $R = 0.877$).

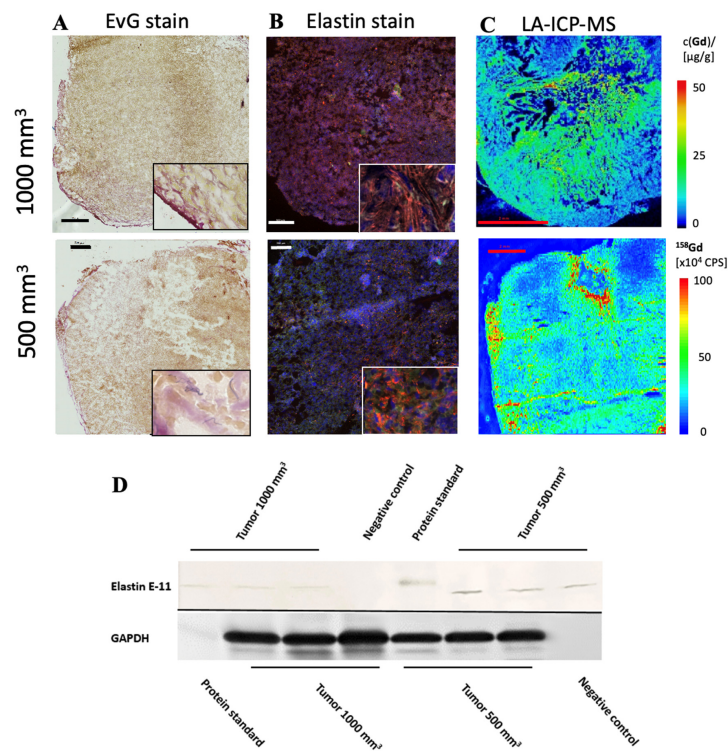


Figure 4. Histological characterization of elastin distribution in 1000 mm³ and 500 mm³ PC3 tumors. (A) shows Elastica–van Gieson staining in frozen sections with a slice thickness of 10 µm from 1000 mm³ (top) and 500 mm³ (bottom) PC3 tumors. Elastic fibers are blue-violet. Elastin fibers were detected especially in the marginal area. In the lower right corner is an enlarged section of the image of the peripheral area of the tumor. Scale bar = 500 µm. (B) A parallel section of the same tumor (thickness 10 µm) as in A was prepared with an anti-elastin antibody (specific for immunofluorescence). The elastic fibers are visible in red. Staining of the cell nuclei was achieved using Dapi (blue). Scale bar = 500 µm; 1000 mm³ (top) and 500 mm³ (bottom) PC3 tumors. (C) The element gadolinium was detected by LA-ICP-MS. The scale shows the intensity of the detected gadolinium (cps) (red—high to blue—low). Scale bar = 2 mm; 1000 mm³ (top) and 500 mm³ (bottom) PC3 tumors. (D) For each group, 3 tumors (n = 3 per group) were used for Western blot analysis to detect the expression of elastin E-11. Here, a different antibody was used than for immunofluorescence, as the antibody is specific for Western blot analyses. GAPDH was included to control protein levels.

The *in vivo* MRI images showed an irregular distribution of the elastin fibers. This observation was also confirmed in the *ex vivo* histological analysis (Figure 4A).

To further evaluate the distribution of elastic fibers in the PC3 tumor, an immunofluorescence staining with an anti-elastin antibody was performed (Figure 4B). This showed an irregular distribution of the elastin fibers in the tissue. The mean value of $n = 4$ was 7.5% ($\sigma = 1.8$) in 500 mm³ and 3.7% ($\sigma = 0.9$) in 1000 mm³ tumors ($p < 0.05$).

The Western blot showed a lower elastin expression in the 1000 mm³ group compared to the 500 mm³ group (Figure 4D) (full WB can be found in Supplementary Materials). For each group, $n = 3$ animals were evaluated. The antibody used for the Western blot was different than that used for immunofluorescence, as the respective antibodies had to be applied specifically to one method.

3.3. Elemental Analysis of Tumor Tissue with Specific Regard to Gadolinium

LA-ICP-MS measurements were used to localize gadolinium in PC3 tumor tissue. Three tumor sections were analyzed for each group ($n = 3$). Strong colocalization of gadolinium with elastic fibers was shown (Figure 4C). Here it can be seen that the peripheral area of the tumor, as well as the intra-tumoral space, contained gadolinium.

The gadolinium concentration in the tumor was quantified by ICP-MS after dissolution of the samples. The concentration of gadolinium with elastic fibers was correlated with *in vivo* RE data and showed a strong correlation ($y = 1.7606x + 0.6126$; $R^2 = 0.78$; $p \leq 0.001$) (Figure 2E). Measurements by ICP-MS were performed in $n = 5$ for each group.

4. Discussion

This study shows the feasibility of an elastin-specific MRI molecular probe for the characterization of a PC3 tumor in a SCID mouse model. The results indicate that elastic fibers have an irregular distribution across the entire PC3 tumor tissue. In all examined tumors, a high number of elastic fibers was measured, especially in the marginal area, regardless of the tumor size. Thus, a better distinction between healthy tissue and tumorous tissue was feasible. In addition, smaller tumors were found to express more elastin than larger tumors.

ECM proteins play an essential role in tumor development, cell behavior, and microenvironment. The ECM is responsible for the architecture of the tumor [33] and can change continuously [34]. The structure of the ECM in tumor diseases is essential for understanding tumor development and therefore for developing diagnostic and therapeutic options. Not only does the elasticity of a tumor depend on the ECM but also the stiffness, and it is responsible for the homeostasis of the tissue [33].

In many types of cancer, such as liver cell carcinoma, the elastin content is a major factor. The elasticity of a tumor depends on the ECM and the stiffness and is responsible for tissue homeostasis [35]. In colorectal cancer (CRC), elastin gene expression was recently examined and it was found that elastin decisively regulates tumor development and the microenvironment [36]. In this study, elastin gene expression was compared in CRC tumors from patients with adjacent non-tumorous colon tissue and healthy tissue (control). Elastin gene expression was found to be increased in patients with CRC tumors compared to the control group and adjacent non-tumor colon tissue. Metalloproteinase (MMP) 9 and 12 and TIMP3 were increased in the colon cancer cells. Another example is breast cancer, where elastin promotes the invasiveness of breast cancer cells [37].

The interaction between the tumor cells and the matrix protein elastin is mediated by elastin-binding proteins (EBPs), S-Gal, and Galectin-3 through the expression and release of elastases [23]. Comparing our two groups, 500 mm³ and 1000 mm³, showed that the group with smaller tumor volumes had a higher SI using the elastin-specific contrast agents. It can be concluded that smaller tumors can be detected particularly well due to a clear distinction from surrounding tissue. In contrast, tumors with a larger volume have fewer elastic fibers, which could be a clear signal of metastasis [23].

The expression level of elastin was not reflected in the Western blot (Figure 4D), as expected from the MRI images. In the Western blot we detected weak bands expressing elastin. The weak bands can be explained by the fact that elastin fibers are insoluble. Elastin is a cross-linked polymer whose cross-linking is difficult to break. Before cross-linking, the soluble precursor tropoelastin forms self-associated aggregates (coacervation) after expression [15]. Only these non-cross-linked aggregates can be broken down back into the small soluble tropoelastin proteins that can be detected in the Western blot. Thus, the Western blot showed the expression of tropoelastin and the coacervated elastin. The band intensity showed a higher expression of new elastin in the 500 mm³ compared to the 1000 mm³ tumors. This correlates to the higher amount of elastin in the immunofluorescence staining (Figure 2E) and the higher MRI signal (Figure 2A) in the 500 mm³ tumors. Since both MRIs showed a high increase in contrast in the T1 measurement after applying the elastin-specific probe, a high elastin density, especially in the periphery of the probe, could be estimated. The immunofluorescence staining against elastin as well as the EvG staining (Figure 4A,B) supports this thesis.

Through cell–matrix interaction, the extracellular matrix is constantly remodeled. The remodeling of the ECM creates a new microenvironment that promotes tumorigenesis and metastasis [38]. Elastin-derived matrikines promote tumor progression (for example, Val-Gly-Val-Ala-Pro-Gly or Ala-Gly-Val-Pro-Gly-Leu-Gly-Val-Gly) [38]. The degradation of elastin produces various proteolytic enzymes, elastases, and MMPs. Matrikines are able to activate the expression of MMPs, which positively promotes the tumor [38]. Elastin can help to detect a tumor or metastases at an early stage by morphologically changing the tumor and initiate appropriate therapy [23]. In addition, a therapy that specifically targets elastin peptides would be a possibility to reduce tumor growth and invasion.

Molecular imaging provides precise information about the tumor but also about the structural characteristics of the tumor. An important step is the use of molecular imaging techniques to make predictions about the molecular characteristics of the tumor to prevent invasive surgery. Currently, molecular imaging methods are based on cell metabolism, hormone receptors, and membrane proteins [39]. The cell metabolism of tumor cells differs from surrounding healthy cells, which can be exploited in molecular imaging. Current research is being conducted on radiolabeled analogs of the metabolic substrates choline, acetate, glucose, amino acids, and nucleosides [39]. These are not specific to the detection of malignant diseases. Specific imaging for PCa can also be achieved using androgen receptors and membrane proteins. For the development of such biomarkers, it is important that they be of low molecular weight and can therefore be released faster in the blood. Pu et al. (2016) showed the targeting of prostate-specific membrane antigen (PSMA) with a protein MRI contrast agent (ProCA) [40]. The 100 kDa glutamate carboxypeptide PSMA is involved in signal transduction, receptor function, nutrient uptake, and cell migration. It is overexpressed in epithelial cells of prostate cancer. PSMA can be detected in primary, secondary, and metastatic prostate cancer, which makes it a good marker [41]. Pu et al. demonstrated that the targeted MRI contrast agent has good Gd³⁺ binding affinity, metal selectivity, and relaxivity, and strong PSMA targeting ability [40]. The contrast agent (ProCA32.PSMA) showed a signal change in T1-weighted images in tumor-bearing mice (xenograft model), but also in the T2-weighted images [40]. The experiments were performed on a 7 Tesla MRI. The results are promising and can be implemented for early detection, but still need to be tested in an orthotopic model first.

Our results show the detection of tumors with components of the ECM in a clinical MRI, which can generate statements about tumor volume and enable predictions about the further course of a tumor. With the help of molecular imaging methods, it is possible to make individual disease predictions without taking tissue samples from the organism. Molecular imaging would be a good addition to existing commercial diagnostic possibilities. The main advantage of molecular MRI is to generate a non-invasive assessment at cellular level. An elastin-specific contrast agent has not only shown good results in cardiovascular diseases [42–44] but could also be used for the detection of malignant liver tumors. In a

recent study, an elastin-specific contrast agent was used to visualize VX2-hepatic tumors in a rabbit model, and the use of the molecular agent to differentiate specific tumor and peritumoral regions based on its ECM composition was confirmed [31]. In addition, Sun et al. were able to demonstrate the usefulness of the probe even in kidney fibrosis [45].

A combination of available diagnostic techniques and molecular imaging would allow specific statements about the stage of disease in a non-invasive manner. If therapy is initiated at an early stage, the chances of survival for the affected patient will increase.

Limitations

This study was conducted in a xenograft mouse model. This allows the tumor to grow in the organism outside the organ. An orthotopic mouse model would allow the tumor to grow in its natural microenvironment.

5. Conclusions

Our study demonstrates that molecular imaging using an elastin-specific gadolinium-containing contrast agent is feasible in prostate cancer. The study also confirms an apparent loss of elastin-specific ECM components in larger tumors. Such an imaging approach could be useful, for example, in predicting the metastatic potential of the tumor.

Supplementary Materials: The following are available online at <https://www.mdpi.com/article/10.3390/biology10111217/s1>. Reference [46] is cited in the supplementary materials.

Author Contributions: Conceptualization, A.K. and M.R.M.; methodology, A.K. and M.R.M.; performed experiments, A.K., J.B., J.O.K., C.R., J.S., R.B. and H.T.; writing original draft preparation, A.K.; writing review and editing, J.B., D.B.M., J.O.K., C.R., L.C.A., J.Z., J.M., J.S., H.T., R.B., U.K., B.H. and M.R.M.; project administration, M.R.M.; funding acquisition, M.R.M., B.H. and H.T. All authors have read and agreed to the published version of the manuscript.

Funding: This research was funded by the Sonderforschungsbereich (SFB), Deutsche Forschungsgemeinschaft (DFG, German Research Foundation)—SFB 1340/1 2018, B01 and C02 (BAM).

Institutional Review Board Statement: This study was performed corresponding to the local guidelines and provisions for the implementation of the Animal Welfare Act and regulations of the Federation of Laboratory Animal Science Associations (FELASA). This animal study was approved by the regulatory authority of the Regional Office for Health and Social Affairs Berlin (LAGeSo) (G0094/19; 04.04.2019).

Informed Consent Statement: Not applicable.

Data Availability Statement: Data are available from the corresponding author upon reasonable request.

Acknowledgments: We are grateful for the financial support from the DFG—German Research Foundation.

Conflicts of Interest: The authors declare no conflict of interest.

References

1. Siegel, R.L.; Miller, K.D.; Jemal, A. Cancer statistics, 2019. *CA Cancer J. Clin.* **2019**, *69*, 7–34. [[CrossRef](#)]
2. Forrest, M.S.; Edwards, S.M.; Houlston, R.; Kote-Jarai, Z.; Key, T.; Allen, N.; Knowles, M.A.; Turner, F.; Arden-Jones, A.; Murkin, A.; et al. Association between Hormonal Genetic Polymorphisms and Early-Onset Prostate Cancer. *Prostate Cancer Prostatic Dis.* **2005**, *8*, 95–102. [[CrossRef](#)]
3. Breslow, N.; Breslow, N.; Chan, C.W.; Dhom, G.; Drury, R.A.B.; Franks, L.M.; Gellei, B.; Lee, Y.S.; Lundberg, S.; Sparke, B.; et al. Latent carcinoma of prostate at autopsy in seven areas. *Int. J. Cancer* **1977**, *20*, 680–688. [[CrossRef](#)] [[PubMed](#)]
4. Shimizu, H.; Ross, R.K.; Bernstein, L.; Yatani, R.; Henderson, B.E.; Mack, T.M. Cancers of the Prostate and Breast among Japanese and White Immigrants in Los-Angeles-County. *Br. J. Cancer* **1991**, *63*, 963–966. [[CrossRef](#)]
5. Steinberg, G.D.; Carter, B.S.; Beauty, T.H.; Childs, B.; Walsh, P.C. *Family History and the Risk of Prostate Cancer*; Wiley-Liss, Inc.: Hoboken, NJ, USA, 1990.
6. Kim, J.H.; Hong, S.K. Clinical utility of current biomarkers for prostate cancer detection. *Investig. Clin. Urol.* **2021**, *62*, 1–13. [[CrossRef](#)]

7. Mistry, K.; Cable, G. Meta-Analysis of Prostate-Specific Antigen and Digital Rectal Examination as Screening Tests for Prostate Carcinoma. *J. Am. Board Fam. Pract.* **2003**, *16*, 95–101. [[CrossRef](#)] [[PubMed](#)]
8. Oesterling, J.E. Prostate Specific Antigen: A Critical Assessment of the Most Useful Tumor Marker for Adenocarcinoma of the Prostate. *J. Urol.* **1991**, *145*, 907–923. [[CrossRef](#)]
9. Roobol, M.J.; Carlsson, S.V. Risk stratification in prostate cancer screening. *Nat. Rev. Urol.* **2013**, *10*, 38–48. [[CrossRef](#)]
10. Watanabe, H.; Igari, D.; Tanahashi, Y.; Harada, K.; Saitoh, M. Transrectal ultrasonotomography of the prostate. *J. Urol.* **1975**, *114*, 734–749.
11. Hegde, J.V.; Mulkern, R.V.; Panych, L.P.; Fennessy, F.M.; Fedorov, A.; Maier, S.E.; Tempny, C.M. Multiparametric MRI of prostate cancer: An update on state-of-the-art techniques and their performance in detecting and localizing prostate cancer. *J. Magn. Reson. Imaging* **2013**, *37*, 1035–1054. [[CrossRef](#)]
12. Ahmed, H.U.; El-Shater Bosaily, A.; Brown, L.C.; Gabe, R.; Kaplan, R.; Parmar, M.K.; Collaco-Moraes, Y.; Ward, K.; Hindley, R.G.; Freeman, A.; et al. Diagnostic accuracy of multi-parametric MRI and TRUS biopsy in prostate cancer (PROMIS): A paired validating confirmatory study. *Lancet* **2017**, *389*, 815–822. [[CrossRef](#)]
13. Westphalen, A.C.; McCulloch, C.E.; Anaokar, J.M.; Arora, S.; Barashi, N.S.; Barentsz, J.O.; Bathala, T.K.; Bittencourt, L.K.; Booker, M.T.; Braxton, V.G.; et al. Variability of the Positive Predictive Value of PI-RADS for Prostate MRI across 26 Centers: Experience of the Society of Abdominal Radiology Prostate Cancer Disease-focused Panel. *Radiology* **2020**, *296*, 76–84. [[CrossRef](#)] [[PubMed](#)]
14. Xiao, Y.D.; Paudel, R.; Liu, J.; Ma, C.; Zhang, Z.S.; Zhou, S.K. MRI contrast agents: Classification and application (Review). *Int. J. Mol. Med.* **2016**, *38*, 1319–1326. [[CrossRef](#)]
15. Zhao, J.; Kader, A.; Mangarova, D.B.; Brangsch, J.; Brenner, W.; Hamm, B.; Makowski, M.R. Dynamic Contrast-Enhanced MRI of Prostate Lesions of Simultaneous [(68)Ga]Ga-PSMA-11 PET/MRI: Comparison between Intraprostatic Lesions and Correlation between Perfusion Parameters. *Cancers* **2021**, *13*, 1404. [[CrossRef](#)] [[PubMed](#)]
16. Palumbo, A., Jr.; Ferreira, L.B.; Reis de Souza, P.A.; Oliveira, F.L.; Pontes, B.; Viana, N.B.; Machado, D.E.; Palmero, C.Y.; Alves, L.M.; Gimba, E.R.; et al. Extracellular matrix secreted by reactive stroma is a main inducer of pro-tumorigenic features on LNCaP prostate cancer cells. *Cancer Lett.* **2012**, *321*, 55–64. [[CrossRef](#)]
17. Jones, P.A.; DeClerck, Y.A. Destruction of Extracellular Matrices Containing Glycoproteins, Elastin, and Collagen by Metastatic Human Tumor Cells. *Cancer Res.* **1980**, *40*, 3222–3227. [[PubMed](#)]
18. Salarian, M.; Ibhagui, O.Y.; Yang, J.J. Molecular imaging of extracellular matrix proteins with targeted probes using magnetic resonance imaging. *Wiley Interdiscip. Rev. Nanomed. Nanobiotechnol.* **2020**, *12*(4), e1622. [[CrossRef](#)]
19. Chaffey, N.; Alberts, B.; Johnson, A.; Lewis, J.; Raff, M.; Roberts, K.; Walter, P. Molecular Biology of the Cell, 4th ed.; In *Annals of Botany*, Garland Science: New York, NY, USA, 2003; Volume 91, p. 401.
20. Hinek, A.; Wrenn, D.S.; Mecham, R.P.; Barondes, S.H. The elastin receptor: A galactoside-binding protein. *Science* **1988**, *239*, 1539–1541. [[CrossRef](#)]
21. Mecham, R.; Hinek, A.; Entwistle, R.; Wrenn, D.; Griffin, G.; and Senior, R. Elastin Binds to a Multifunctional 67-Kilodalton Peripheral Membrane Protein. *Biochemistry* **1989**, *28*, 3716–3722. [[CrossRef](#)]
22. Timar, J.; Lapis, K.; Fulop, T.; Varga, Z.S.; Tixier, J.M.; Robert, L.; Homebeck, W. Interaction between elastin and tumor cell lines with different metastatic potential; in vitro and in vivo studies. *J. Cancer Res. Clin. Oncol.* **1991**, *117*, 232–238. [[CrossRef](#)]
23. Lapis, K.; Timár, J. Role of elastin–matrix interactions in tumor progression. *Semin. Cancer Biol.* **2002**, *12*, 209–217. [[CrossRef](#)]
24. Wang, T.H.; Hsia, S.M.; Shieh, T.M. Lysyl Oxidase and the Tumor Microenvironment. *Int. J. Mol. Sci.* **2016**, *18*, 62. [[CrossRef](#)] [[PubMed](#)]
25. Siegel, R.C.; Pinnell, S.R.; Martin, G.R. Cross-linking of collagen and elastin. Properties of lysyl oxidase. *Biochemistry* **1970**, *9*, 4486–4492.
26. Calderón, L.G.R.; Kobayashi, P.E.; Vasconcelos, R.O.; Fonseca-Alves, C.E.; Laufer-Amorim, R. Characterization of Collagen Fibers (I, III, IV) and Elastin of Normal and Neoplastic Canine Prostatic Tissues. *Vet. Sci.* **2019**, *6*, 22. [[CrossRef](#)] [[PubMed](#)]
27. Scandola, A.; Odoul, L.; Salesse, S.; Guillot, A.; Blaise, S.; Kawecky, C.; Maurice, P.; El Btaouri, H.; Romier-Crouzet, B.; Martiny, L.; et al. The Elastin Receptor Complex: A Unique Matricellular Receptor with High Anti-tumoral Potential. *Front. Pharmacol.* **2016**, *7*, 32. [[CrossRef](#)]
28. Kruslin, B.; Ulamec, M.; Tomas, D. Prostate cancer stroma: An important factor in cancer growth and progression. *Bosn. J. Basic Med. Sci.* **2015**, *15*, 1–8. [[CrossRef](#)] [[PubMed](#)]
29. Heeneman, S.; Cleutjens, J.P.; Faber, B.C.; Creemers, E.E.; van Suylen, R.J.; Lutgens, E.; Cleutjens, K.B.; Daemen, M.J. The dynamic extracellular matrix: Intervention strategies during heart failure and atherosclerosis. *J. Pathol.* **2003**, *200*, 516–525. [[CrossRef](#)]
30. Makowski, M.R.; Wiethoff, A.J.; Blume, U.; Cuello, F.; Warley, A.; Jansen, C.H.; Nagel, E.; Razavi, R.; Onthank, D.C.; Cesati, R.R.; et al. Assessment of atherosclerotic plaque burden with an elastin-specific magnetic resonance contrast agent. *Nat. Med.* **2011**, *17*, 383–388. [[CrossRef](#)]
31. Keller, S.; Borde, T.; Brangsch, J.; Reimann, C.; Kader, A.; Schulze, D.; Buchholz, R.; Kaufmann, J.O.; Karst, U.; Schellenberger, E.; et al. Assessment of the hepatic tumor extracellular matrix using elastin-specific molecular magnetic resonance imaging in an experimental rabbit cancer model. *Sci. Rep.* **2020**, *10*, 20785. [[CrossRef](#)]
32. Von Bary, C.; Makowski, M.; Preissel, A.; Keithahn, A.; Warley, A.; Spuentrup, E.; Buecker, A.; Lazewatsky, J.; Cesati, R.; Onthank, D.; et al. MRI of coronary wall remodeling in a swine model of coronary injury using an elastin-binding contrast agent. *Circ. Cardiovasc. Imaging* **2011**, *4*, 147–155. [[CrossRef](#)]

33. Bonnans, C.; Chou, J.; Werb, Z. Remodelling the extracellular matrix in development and disease. *Nat. Rev. Mol. Cell Biol.* **2014**, *15*, 786–801. [[CrossRef](#)]
34. Hynes, R.O. The extracellular matrix: Not just pretty fibrils. *Science* **2009**, *326*, 1216–1219. [[CrossRef](#)] [[PubMed](#)]
35. Murphy, G. The ADAMs: Signalling scissors in the tumour microenvironment. *Nat. Rev. Cancer* **2008**, *8*, 929–941. [[CrossRef](#)]
36. Li, J.; Xu, X.; Jiang, Y.; Hansbro, N.G.; Hansbro, P.M.; Xu, J.; Liu, G. Elastin is a key factor of tumor development in colorectal cancer. *BMC Cancer* **2020**, *20*, 217. [[CrossRef](#)]
37. Salesse, S.; Odoul, L.; Chazee, L.; Garbar, C.; Duca, L.; Martiny, L.; Mahmoudi, R.; Debelle, L. Elastin molecular aging promotes MDA-MB-231 breast cancer cell invasiveness. *FEBS Open Bio.* **2018**, *8*, 1395–1404. [[CrossRef](#)] [[PubMed](#)]
38. Winkler, J.; Abisoye-Ogunniyan, A.; Metcalf, K.J.; Werb, Z. Concepts of extracellular matrix remodelling in tumour progression and metastasis. *Nat. Commun.* **2020**, *11*, 5120. [[CrossRef](#)] [[PubMed](#)]
39. Wibmer, A.G.; Burger, I.A.; Sala, E.; Hricak, H.; Weber, W.A.; Vargas, H.A. Molecular Imaging of Prostate Cancer. *Radio Graph.* **2016**, *36*, 142–161. [[CrossRef](#)]
40. Pu, F.; Salarian, M.; Xue, S.; Qiao, J.; Feng, J.; Tan, S.; Patel, A.; Li, X.; Mamouni, K.; Hekmatyar, K.; et al. Prostate-specific membrane antigen targeted protein contrast agents for molecular imaging of prostate cancer by MRI. *Nanoscale* **2016**, *8*, 12668–12682. [[CrossRef](#)] [[PubMed](#)]
41. Zhao, J.; Mangarova, D.B.; Brangsch, J.; Kader, A.; Hamm, B.; Brenner, W.; Makowski, M.R. Correlation between Intraprostatic PSMA Uptake and MRI PI-RADS of [(68)Ga]Ga-PSMA-11 PET/MRI in Patients with Prostate Cancer: Comparison of PI-RADS Version 2.0 and PI-RADS Version 2.1. *Cancers* **2020**, *12*, 3523. [[CrossRef](#)]
42. Makowski, M.R.; Preissel, A.; von Bary, C.; Warley, A.; Schachoff, S.; Keithan, A.; Cesati, R.R.; Onthank, D.C.; Schwaiger, M.; Robinson, S.P.; et al. Three-Dimensional Imaging of the Aortic Vessel Wall Using an Elastin-Specific Magnetic Resonance Contrast Agent. *Investig. Radiol.* **2012**, *47*, 438–444.
43. Reimann, C.; Brangsch, J.; Kaufmann, J.O.; Adams, L.C.; Onthank, D.C.; Thone-Reineke, C.; Robinson, S.P.; Hamm, B.; Botnar, R.M.; Makowski, M.R. Dual-probe molecular MRI for the in vivo characterization of atherosclerosis in a mouse model: Simultaneous assessment of plaque inflammation and extracellular-matrix remodeling. *Sci. Rep.* **2019**, *9*, 13827. [[CrossRef](#)] [[PubMed](#)]
44. Brangsch, J.; Reimann, C.; Kaufmann, J.O.; Adams, L.C.; Onthank, D.C.; Thone-Reineke, C.; Robinson, S.P.; Buchholz, R.; Karst, U.; Botnar, R.M.; et al. Concurrent Molecular Magnetic Resonance Imaging of Inflammatory Activity and Extracellular Matrix Degradation for the Prediction of Aneurysm Rupture. *Circ. Cardiovasc. Imaging* **2019**, *12*, e008707. [[CrossRef](#)] [[PubMed](#)]
45. Sun, Q.; Baues, M.; Klinkhammer, B.M.; Ehling, J.; Djudjaj, S.; Drude, N.I.; Daniel, C.; Amann, K.; Kramann, R.; Kim, H.; et al. Elastin imaging enables noninvasive staging and treatment monitoring of kidney fibrosis. *Sci. Transl. Med.* **2019**, *11*, 486. [[CrossRef](#)] [[PubMed](#)]
46. Stärk, H.-J.; Wennrich, R. A new approach for calibration of laser ablation inductively coupled plasma mass spectrometry using thin layers of spiked agarose gels as references. *Anal. Bioanal. Chem.* **2011**, *399*, 2.

Article

Supporting Information

Elastin specific contrast agent for MRI to characterize prostate cancer

Avan Kader ^{1,2}, Julia Brangsch ¹, Carolin Reimann ¹, Jan O. Kaufmann ^{1,4,5}, Dilyana B. Mangarova ^{1,3}, Jana Moeckel ¹, Lisa Adams ¹, Jing Zhao ¹, Jessica Saatz ⁶, Heike Traub ⁶, Rebecca Buchholz ⁷, Uwe Karst ⁷, Bernd Hamm ¹, Marcus R. Makowski ^{1,8,9}

- ¹ Charité – Universitätsmedizin Berlin, corporate member of Freie Universität Berlin, Humboldt-Universität zu Berlin, and Berlin Institute of Health, Charitéplatz 1, 10117 Berlin, Germany; julia.brangsch@charite.de (J.B.); carolin.reimann@charite.de (C.R.); jan-ole.kaufmann@charite.de (J.O.K.); dilyana.mangarova@charite.de (D.B.M.); jana.moeckel@charite.de (J.M.); lisa.adams@charite.de (L.C.A.); jing.zhao@charite.de (J.Z.); bernd.hamm@charite.de (B.H.); marcus.makowski@tum.de (M.R.M)
- ² Department of Biology, Chemistry and Pharmacy, Institute of Biology, Freie Universität Berlin, Königin-Luise-Str. 1-3, 14195 Berlin, Germany
- ^{*} Department of Veterinary Medicine, Institute of Veterinary Pathology, Freie Universität Berlin, Robert-von-Ostertag-Str. 15, Building 12, 14163 Berlin, Germany
- ⁴ Bundesanstalt für Materialforschung und -prüfung (BAM), Division 1.5 Protein Analysis, Richard-Willstätter-Str. 11, 12489 Berlin, Germany
- ⁵ Humboldt-Universität zu Berlin, Department of Chemistry, Brook-Taylor-Str. 2, 12489 Berlin, Germany
- ⁶ Bundesanstalt für Materialforschung und -prüfung (BAM), Division 1.1 Inorganic Trace Analysis, Richard-Willstätter-Str. 11, 12489 Berlin, Germany; jessica.saatze@bam.de (J.S.); heike.traub@bam.de (H.T.)
- ⁷ Institute of Inorganic and Analytical Chemistry, Westfälische Wilhelms-Universität Münster, Münster, Germany (rebecca.buchholz@uni-muenster.de) (R.B.); uk@uni-muenster.de (U.K.)
- ⁸ King's College London, School of Biomedical Engineering and Imaging Sciences, United Kingdom, St Thomas' Hospital Westminster Bridge Road, London SE1 7EH, United Kingdom
- ⁹ Technical University of Munich, Department of Diagnostic and Interventional Radiology, Ismaninger Str.22, 81675 Munich, Germany
- ^{*} Correspondence: avan.kader@charite.de

2.10. Laser ablation-inductively coupled plasma-mass spectroscopy (LA-ICP-MS)

System 1

A LSX 213 G2+ laser system (CETAC Technologies, Omaha, NE, USA) with a two volume HelEx II cell connected *via* Tygon tubing to an ICPMS-2030 (Shimadzu, Kyoto, Japan) were used for the measurement of the 1000 mm³ PC3-tumor sample. The samples were scanned at points with a size of 30 µm at a speed of 90 µm/s and 800 mL/min He as the transport gas. Standards were used for the quantification of ¹⁵⁸Gd, which are based on a gelatine standard (10% w/w) and are set at different concentrations of Gd from 1 to 500 µg/g. Three more isotopes, ³¹P, ⁵⁷Fe and ⁶⁴Zn were measured in addition to the Gd in collision gas mode with He as the collision gas and an integration time of 100 ms. The limit of detection and the limit of quantification calculated with the 3σ- and 10σ-criteria, were 33 ng/g and 110 ng/g Gd.

System 2

LA-ICP-MS analysis of the 500 mm² PC3-tumor sample was performed on a commercial LA system (NWR-213, ESI, Bozeman, MT, USA) equipped with a two-volume sample

chamber coupled to a sector field ICP-MS (Element XR, Thermo Fisher Scientific, Bremen, Germany).

Helium was used as carrier gas with 1000 mL/min transporting the sample aerosol to the sector field ICP-MS, which was using the following parameters: sample time 0.002 s⁻¹, samples per peak 100, segment duration per isotope 0.01 s⁻¹, mass window per isotope 5%, search window 0%, integration window 5%. The samples were scanned with a spot size of 80 µm, 50 µm line spacing and a scan speed of 100 µm/s. The isotopes ³¹P, ³⁴S, ⁵⁷Fe, ⁶⁵Cu, ⁶⁶Zn, ¹⁵³Eu, ¹⁶⁰Gd were measured in addition to ¹⁵⁸Gd.

Matrix-matched agarose gel standards cast on glass slides were used for drift control and calibration.[1] These standards contain Gd concentrations between 26.6 pg mm⁻² and 600.1 pg mm⁻². Intensities of six line scans per standard were averaged for calibration.

Figure 5: Western Blot analyse

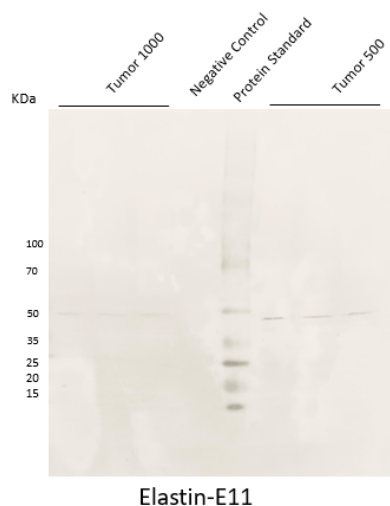


Figure 5.1: Western Blot analyse for Elastin-E11. For each group, 3 tumors ($n = 3$ per group) were used for western blot analysis to detect the expression of elastin E-11. Intensity signal: Tumor 1000: left line 10.252, middle line 10.212 and right line 10.259; Tumor 500: left line 29.392, middle line 22.351 and 17.535.

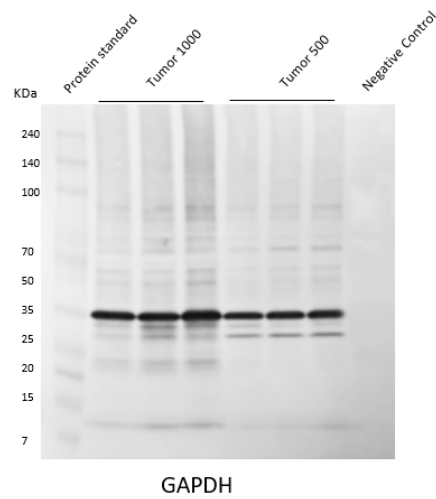


Figure 5.2: Western Blot analyse for GAPDH. For each group, 3 tumors ($n = 3$ per group) were used for western blot analysis to control protein levels. Intensity signal: Tumor 1000: left line 18.874, middle line 17.081 and right line 17.516; Tumor 500: left line 15.588, middle line 15.394 and 15.547.

1. Stärk, H.-J.; Wennrich, R. A new approach for calibration of laser ablation inductively coupled plasma mass spectrometry using thin layers of spiked agarose gels as references. *Anal. Bioanal. Chem.* **2011**, *399*, 2.

4. Publication II

Title: Iron Oxide Nanoparticles for Visualization of Prostate Cancer in MRI

Authors: Avan Kader, Jan O. Kaufmann, Dilyana B. Mangarova, Jana Moeckel, Julia Brangsch, Lisa C. Adams, Jing Zhao, Carolin Reimann, Jessica Saatz, Heike Traub, Rebecca Buchholz, Uwe Karst, Bernd Hamm and Marcus R. Makowski

Year: 2022

Journal: Cancers





Impact factor: 6.102

DOI: <https://doi.org/10.3390/cancers14122909>

Authors' contribution: I developed the concept and design of the study. I designed the theory and the experimental plan. The animal experiments, the MRI examinations, and the histological analysis were carried out by me. The manuscript was written independently by me. Every author discussed the results and contributed to the final version of the publication. For a detailed list of the other author's contributions, see the published version of the paper.

Article

Iron Oxide Nanoparticles for Visualization of Prostate Cancer in MRI

Avan Kader ^{1,2,3,*} , Jan O. Kaufmann ^{1,4,5}, Dilyana B. Mangarova ^{1,6}, Jana Moeckel ¹, Julia Brangsch ¹ , Lisa C. Adams ¹, Jing Zhao ¹ , Carolin Reimann ¹, Jessica Saatz ⁷, Heike Traub ⁷, Rebecca Buchholz ⁸, Uwe Karst ⁸ , Bernd Hamm ¹ and Marcus R. Makowski ^{1,3,9}

- ¹ Charité—Universitätsmedizin Berlin, Corporate Member of Freie Universität Berlin, Humboldt-Universität zu Berlin, and Berlin Institute of Health, Charitéplatz 1, 10117 Berlin, Germany; jan-ole.kaufmann@charite.de (J.O.K.); dilyana.mangarova@charite.de (D.B.M.); jana.moeckel@charite.de (J.M.); julia.brangsch@charite.de (J.B.); lisa.adams@charite.de (L.C.A.); jing.zhao@charite.de (J.Z.); carolinreimann1990@web.de (C.R.); bernd.hamm@charite.de (B.H.); marcus.makowski@tum.de (M.R.M.)
- ² Department of Biology, Chemistry and Pharmacy, Institute of Biology, Freie Universität Berlin, Königin-Luise-Str. 1-3, 14195 Berlin, Germany
- ³ Department of Diagnostic and Interventional Radiology, Technical University of Munich, Ismaninger Str. 22, 81675 Munich, Germany
- ⁴ Division 1.5 Protein Analysis, Bundesanstalt für Materialforschung und-Prüfung (BAM), Richard-Willstätter-Str. 11, 12489 Berlin, Germany
- ⁵ Department of Chemistry, Humboldt-Universität zu Berlin, Brook-Taylor-Str. 2, 12489 Berlin, Germany
- ⁶ Department of Veterinary Medicine, Institute of Veterinary Pathology, Freie Universität Berlin, Robert-von-Ostertag-Str. 15, Building 12, 14163 Berlin, Germany
- ⁷ Division 1.1 Inorganic Trace Analysis, Bundesanstalt für Materialforschung und-Prüfung (BAM), Richard-Willstätter-Str. 11, 12489 Berlin, Germany; jessica.saatz@bam.de (J.S.); heike.traub@bam.de (H.T.)
- ⁸ Institute of Inorganic and Analytical Chemistry, Westfälische Wilhelms-Universität Münster, 48149 Münster, Germany; rebecca.buchholz@uni-muenster.de (R.B.); uk@uni-muenster.de (U.K.)
- ⁹ School of Biomedical Engineering and Imaging Sciences, King's College London, St Thomas' Hospital Westminster Bridge Road, London SE1 7EH, UK
- * Correspondence: avan.kader@charite.de



Citation: Kader, A.; Kaufmann, J.O.; Mangarova, D.B.; Moeckel, J.; Brangsch, J.; Adams, L.C.; Zhao, J.; Reimann, C.; Saatz, J.; Traub, H.; et al. Iron Oxide Nanoparticles for Visualization of Prostate Cancer in MRI. *Cancers* **2022**, *14*, 2909. <https://doi.org/10.3390/cancers14122909>

Academic Editor: Leonardo Pace

Received: 12 April 2022

Accepted: 11 June 2022

Published: 13 June 2022

Publisher's Note: MDPI stays neutral with regard to jurisdictional claims in published maps and institutional affiliations.



Copyright: © 2022 by the authors. Licensee MDPI, Basel, Switzerland. This article is an open access article distributed under the terms and conditions of the Creative Commons Attribution (CC BY) license (<https://creativecommons.org/licenses/by/4.0/>).

Simple Summary: Magnetic resonance imaging (MRI) is a non-invasive method and can be used to diagnose prostate cancer (PCa). Due to their high biological safety, iron oxide nanoparticles are becoming increasingly important as contrast agents for MRI. Macrophages are able to take up these iron particles, which leads to a loss of signal in T2- and T2*-weighted images during MRI. Macrophages play an important role in the development and progression of prostate cancer. In this article, ferumoxytol is visualized at two different PCa volumes on MRI in a xenograft mouse model. Ferumoxytol is a superparamagnetic iron oxide probe and was used here as a contrast agent. The in vivo data were correlated with histological data. When using ferumoxytol, we found that small tumors took up more ferumoxytol than larger tumor volumes. These results were obtained in vivo as well as ex vivo.

Abstract: Prostate cancer (PCa) is one of the most common cancers in men. For detection and diagnosis of PCa, non-invasive methods, including magnetic resonance imaging (MRI), can reduce the risk potential of surgical intervention. To explore the molecular characteristics of the tumor, we investigated the applicability of ferumoxytol in PCa in a xenograft mouse model in two different tumor volumes, 500 mm³ and 1000 mm³. Macrophages play a key role in tumor progression, and they are able to internalize iron-oxide particles, such as ferumoxytol. When evaluating T2*-weighted sequences on MRI, a significant decrease of signal intensity between pre- and post-contrast images for each tumor volume ($n = 14$; $p < 0.001$) was measured. We, furthermore, observed a higher signal loss for a tumor volume of 500 mm³ than for 1000 mm³. These findings were confirmed by histological examinations and laser ablation inductively coupled plasma-mass spectrometry. The 500 mm³ tumors had 1.5% iron content ($n = 14$; $\sigma = 1.1$), while the 1000 mm³ tumors contained only 0.4% iron ($n = 14$; $\sigma = 0.2$). In vivo MRI data demonstrated a correlation with the ex vivo data ($R^2 = 0.75$). The results of elemental analysis by inductively coupled plasma-mass spectrometry correlated strongly with the

MRI data ($R^2 = 0.83$) ($n = 4$). Due to its long retention time in the blood, biodegradability, and low toxicity to patients, ferumoxytol has great potential as a contrast agent for visualization PCa.

Keywords: molecular imaging; prostate cancer; iron oxide nanoparticle

1. Introduction

Prostate cancer (PCa) is a malignant and heterogeneous tumor disease, being one of the most common fatal cancers in men [1]. Biomarker testing is often used as a screening test, whereby the prostate-specific antigen (PSA) value is determined from a blood sample. In addition, determination of the prostate health index (PHI) and 4K score can help distinguish between indolent and progressive prostate tumors [2]. Magnetic resonance examinations provide a non-invasive and non-ionizing method to diagnose PCa [3].

Early and reliable detection of tumors based on non-invasive methods is one of the main goals of current tumor research. Multifunctional magnetic nanoparticles can be used in different therapies but also for imaging methods, including magnetic resonance imaging (MRI) [4]. MRI has a high-spatial resolution, is noninvasive, and can be performed in vivo. Iron-containing contrast agents, such as iron oxide nanoparticles, show high biosafety and can be visualized in T2 and T2*-weighted images [4].

After administration of superparamagnetic iron oxide nanoparticles (SPIONs), SPIONs accumulate in the tissue, decreasing the transverse relaxation time of T2, which leads to increased magnetic susceptibility and signal loss in T2 and T2*-weighted images [5–7].

Compared to other SPIONs, Feraheme[®] (ferumoxytol) shows high stability due to reduced carboxymethyl dextran, uniform particle size, and an improved safety profile. Ferumoxytol exhibits a core size of 3 nm to 12 nm [4,8] and a particle size of 17–30 nm. When these particles enter the blood circulation, they will be internalized by activated macrophages. Macrophages have one of the most important functions of the innate immune response and can be involved in the development of tumors [9]. Due to the microenvironment, macrophages can be pro-inflammatory (M1) or anti-inflammatory (M2). The distinction between M1 and M2 can always be clearly differentiated by the variability in the molecular expression profile. In tumors, tumor-associated macrophages (TAMs) also play a key role. Circulating monocytes mature into macrophages. When these migrate in the tumor microenvironment they can be recruited to TAMs [10]. During tumor progression, they influence various processes, such as angiogenesis, tumor cell proliferation, and metastasis [11]. Several research groups have shown a correlation between the uptake of ferumoxytol by TAMs, therapeutic response, and cancer stage [12,13]. The uptake of ferumoxytol by TAMs could be an important step for molecular imaging. The phagocytic cells store the ferumoxytol nanoparticles in secondary lysosomes [14,15]. The carboxymethyl dextran coating is cleaved by dextranase and can be completely excreted by the kidneys. The iron nucleus is integrated into the body's iron store and is used for cell metabolism and hemoglobin synthesis [15].

Biocompatible magnetic iron oxide nanoparticles (MNPs) have the potential to improve tumor evaluation. Tse et al. developed an MNP conjugated with J591 [16]. J591 is an antibody against an extracellular epitope of prostate-specific membrane antibody (PSMA). It was shown that tumors in vivo enhanced magnetic resonance contrast of tumors with PSMA targeting MNPs. Conjugated superparamagnetic iron oxide particles to target PSMA showed promising results in in vitro tests [17]. Zhu et al. synthesized a PSMA-targeting polypeptide CQKHHNYLC conjugated with SPIONs [18].

In vivo studies enhanced the MRI signal in PSMA-expressing tumors. Histological examination showed heterogeneous deposition of SPIONs in prostate tumor tissue. Modified SPIONs indicate tumor-specific targeting, but not all tumors express these antibodies or proteins, e.g., PSMA [19].

This study investigated the applicability of ferumoxytol for MRI imaging in a xenograft prostate cancer mouse model. Two tumor sizes, 500 mm³ and 1000 mm³, were investigated. The imaging results were analyzed and compared with histological and biochemical measurements.

2. Materials and Methods

2.1. Cell Culture

PC3 cells were purchased from ATCC[®] CRL-1435[™] (Manassas, VA, USA) and grown in Roswell Park Memorial Institute (RPMI) 1640 medium (Gibco[™], Thermo Fischer Scientific, Waltham, MA, USA) and supplemented with 10% fetal calf serum (FCS) (Gibco[™], Thermo Fischer Scientific, Waltham, MA, USA). The genetic information of the cell line are available on the website from ATCC[®]. Cells were cultured in 150 cm³ tissue culture flasks until they were about 80% confluent. Then, the cells were washed with phosphate-buffered saline (PBS) (Gibco[™], Thermo Fischer Scientific, Waltham, MA, USA), trypsinized and resuspended in 1 mL RPMI medium. Cells were grown at 37 °C and 5% CO₂. To count the cells, 0.4% trypan blue solution (Gibco[™], Thermo Fischer Scientific, Waltham, MA, USA) was used.

2.2. Xenograft Mouse Model and In Vivo Study Design

Experiments were performed in accordance with the local guidelines and regulations for the implementation of the Animal Welfare Act and the regulations of the Federation of Laboratory Animal Science Associations (FELASA). Animal experiments were approved by the supervisory authority of the Berlin State Office for Health and Social Affairs (LAGeSo) (G0094/19). Eight-week-old male SCID mice (CB17/Icr-Prkdcscid/IcrIcoCrI) were obtained from Charles River Laboratories (Sulzfeld, Germany) ($n = 28$). The animals were randomly divided into two separate groups ($n = 14$).

For anesthesia, medetomidine (500 µg/kg), midazolam (5 mg/kg), and fentanyl (50 µg/kg) were injected intraperitoneally into the mice for anesthesia. A cell suspension containing 2×10^6 PC3 cells was injected subcutaneously into the right scapula area. Anesthesia was subsequently antagonized with atipamezole (750 µg/kg), flumazenil (0.5 mg/kg), and naloxone (1200 µg/kg).

In vivo MR imaging was performed when the tumor size reached 500 mm³ ($n = 14$) or 1000 mm³ ($n = 14$), respectively. Tumor size was measured with a caliper. The in vivo imaging was obtained on two consecutive days. On day one, first a native MRI acquisition took place followed by the administration of the contrast agent, ferumoxytol, via the tail vein. Subsequently, the anesthesia was antagonized. A second MRI was performed for the detection and imaging of the accumulation of ferumoxytol 24 h later on day two. After MRI, mice were euthanized, and tumor tissues were collected for ex vivo studies. Figure 1 demonstrates the study design.

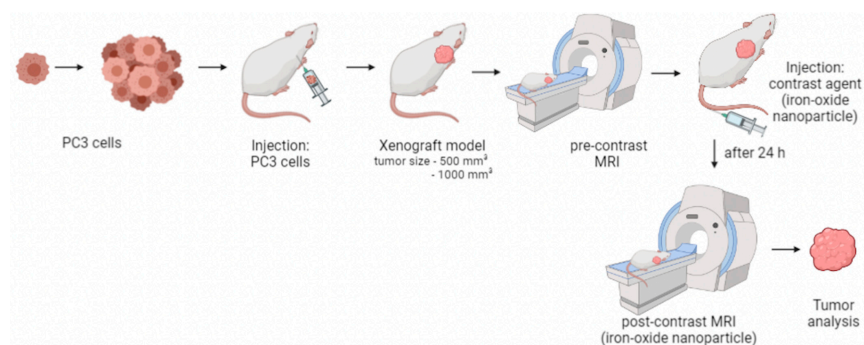


Figure 1. Study design. After reaching the desired tumor size, a pre-contrast image of the tumor was taken. MRI examination was followed by iron-oxide particle injection (ferumoxytol) into the tail vein of the mouse. After 24 h, a post-contrast MRI scan was taken. After in vivo imaging, the tumor was removed and examined.

2.3. In Vivo MRI

In vivo MR imaging was performed using a 3.0 Tesla MR scanner (MAGNETOM Lumina, Siemens, Erlangen, Germany) and a 4-channel receive coil array for mouse body applications (Mouse scapula Array, P-H04LE-030, version1, Rapid Biomedical GmbH, Rimpfing, Germany). Following intraperitoneal anesthesia, we positioned the mice on the MRI patient table in the prone position. For administration of the contrast agent during MR imaging, venous access was established via the tail vein. Body temperature (37 °C) was monitored using an MR-compatible heating system (model 1025, SA Instruments Inc., Stony Brook, NY, USA) to prevent rapid cooling.

2.4. Ferumoxytol as a Contrast Agent for MRI

Feraheme® (Ferumoxytol) (AMAG Pharmaceuticals, Waltham, MA, USA) is a super-paramagnetic iron-oxide particle preparation used in adult patients for the treatment of iron deficiency anemia. The preparation can also be used off-label as a contrast agent in MRI examinations [20]. Ferumoxytol was commercially purchased and used for this study. In this study, it was used as a contrast agent for MRI, leading to a large decrease in T1, T2, and T2* relaxation times [15,21]. Feraheme® has a prolonged blood pool phase with a plasma half-life of 14–21 h. The iron particles are taken up intracellularly with a time delay, which allows MR imaging after 24 h. Mice were administered a clinical dose of 4 mg/kg ferumoxytol via the tail vein.

2.5. Ferumoxytol Imaging Using T2* Weighted Sequences

MR imaging was performed with a 3.0 Tesla MR scanner. Following anesthesia, the mice were positioned in the prone position and examined using a 4-channel receive-coil array. For the localization of the tumor in low resolution, a three-dimensional localizer scan was used, which was performed in sagittal, coronal, and transverse orientation with the following parameters: field-of-view (FOV) = 280 × 280 mm, matrix = 320, slice thickness = 1.5 mm, repetition time (TR) = 11.0 ms, echo time (TE) = 5.39 ms, flip angle = 20°, and number of slices = 10. T1-weighted anatomical images were acquired using the following parameters: FOV = 70 mm, matrix = 131, slice thickness = 0.4 mm, TR = 833.8 ms, TE = 6.34 ms, flip angle = 30°, and number of slices = 30. To visualize the iron-oxide-based contrast agent, a T2*-weighted sequence with the following parameters: FOV = 150 mm, matrix = 201, slice thickness = 1.2 mm, TR = 3200.0 ms, TE = 77.0 ms, flip angle = 140°, and number of slices = 25.

Native MRI acquisition took place on day one and contrast-enhanced MRI on day two. After the first MRI pre-contrast session, the contrast agent was administered via the tail vein. Subsequently, the anesthesia was antagonized, and a second MRI was performed 24 h later.

2.6. MRI Measurements

MR images were evaluated using Visage 7.1 (Version7.1, Visage Imaging, Berlin, Germany). The T2*-weighted images were analyzed before and 24 h after the administration of the contrast agent (signal loss = *SI*). For relative reduction (*RR*) assessment, 2D regions of interests (ROIs) were drawn around the respective areas in pre-contrast and post-contrast MR images. The following formula was used to calculate the relative reduction (*RR*):

$$RR = \frac{(SI_{precontrast} - SI_{postcontrast})}{SI_{precontrast}}$$

2.7. Histological Analysis

Frozen tumor samples were cut in 9 µm thick serial sections at −20 °C. Sections were then fixed with cold acetone (>99%, Fisher scientific, Hampton, VA, USA) for 6 min at −20 °C. To visualize the iron ions, a Perls' Prussian blue stain was performed. Immunofluorescence staining was used to assess the localization and density of macrophages. The tumor tissue was cut in 9 µm thick serial sections at −20 °C on SuperFrost Plus adhesion

slides (Thermo Scientific, Waltham, MA, USA). The sections were incubated overnight at 4 °C with a monoclonal CD68 antibody (1:100) (rat anti-mouse CD68, clone FA-11, Bio-Rad, Hercules, CA, USA) diluted in Dako REAL™ Antibody Diluent (Dako, Denmark). Following, slides were washed three times with PBS (pH = 7.4). For macrophage visualization, slides were incubated for one hour with AlexaFluor 568 polyclonal secondary antibody diluted 1:200 (goat versus rat IgG, Thermo Fisher Scientific, Massachusetts, USA), then counterstained, and mounted with Roti®-Mount FlourCare (Carl Roth, Karlsruhe, Germany). In conclusion, the sections were analyzed using a Keyence microscope (BZ-X800 Series, Osaka Prefecture, Japan).

2.8. Quantification of the Iron and Macrophages in Immunofluorescence

Quantification of staining of iron and immunofluorescence sections was measured using BZ-X800 Analyzer image analysis software (Keyence, Osaka Prefecture, Japan). Three representative areas (two peripheral areas and one central area) were analyzed for each sample. The mean value was calculated in each case. First, the entire region of interest was marked. Then, all stained iron particles or macrophages were identified, and this ratio to the total labeled tumor region was calculated using the labeled pixels.

2.9. Laser Ablation-Inductively Coupled Plasma-Mass Spectroscopy (LA-ICP-MS)

Localization of iron in tumor tissue was performed by LA-ICP-MS ($n=3$ per group). The tumor samples were cut into 9 µm cryosections at −20 °C and mounted on SuperFrost Plus slides (Thermo Scientific, Waltham, MA, USA). LA-ICP-MS analysis was performed with a LSX 213 G2+ laser system (CETAC Technologies, Omaha, NE, USA) equipped with a two volume HelEx II cell connected via Tygon tubing to an ICPMS-2030 (Shimadzu, Kyoto, Japan). Line-by-line scanning of the samples was used with a spot size of 30 µm, a scan speed of 90 µm/s, and 800 mL/min. He was used as the transport gas. The analysis was performed in collision gas mode with He as the collision gas and 50 ms integration time for the ⁵⁷Fe isotope. For the quantification of Fe, matrix-matched standards based on gelatin were used. Nine gelatin standards (10% *w/w*), including a blank, were spiked with different Fe concentrations, ranging from 7 to 1300 µg/g. Averaged intensities of the scanned lines of the standards showed good linear correlation with the regression coefficient, $R^2 = 0.996$, within this concentration range. Limit of detection (LOD) and limit of quantification (LOQ), calculated with the 3σ - and 10σ -criteria, were 3.4 µg/g and 11.4 µg/g Fe, respectively. The quantification and visualization were performed with an in-house developed software (written by Robin Schmid, University of Münster, Münster, Germany).

2.10. Inductively Coupled Plasma-Mass Spectrometry (ICP-MS)

ICP-MS was used to determine the total iron (Fe) concentration in the tumor samples. A section of tumor probe was prepared ($n = 6$ per group) and dehydrated under a vacuum atmosphere (vacuum-pumping device, vacuubrand, Wertheim, Germany). To each of the samples, 1 mL of 66% nitric acid was added, followed by incubation at room temperature until the tissue was completely dissolved. Afterwards, deionized water was then added to each sample.

The digested samples were diluted in nitric acid (sub-boiled) 1% and analyzed with an iCAP Qc ICP quadrupole mass spectrometer (Thermo Fisher Scientific, Bremen, Germany) in combination with the autosampler, SC4-DX (ESI Elemental Service & Instruments GmbH, Mainz, Germany), using a 200 µL PFA nebulizer and a cyclone spray chamber. Measurements of the isotopes ⁵⁶Fe, ⁵⁷Fe were performed in KED mode using a nebulizer gas flow rate of 1.08 L/min and a helium flow rate of 5 mL/min as the collision gas. Calibration was carried out in the concentration range of 0.1–50 ng/L with the diluted iron ICP standard CertiPUR (Merck KGaA, Darmstadt, Germany); rhodium was used as the internal standard.

2.11. Western Blot

For the western blot, tumor pieces ($n = 3$ per group) were first homogenized in RIPA buffer (50 mM Tris·HCl (Carl Roth GmbH, Karlsruhe, Germany), 150 mM NaCl (Carl Roth GmbH, Karlsruhe, Germany), 0.1% SDS (Carl Roth GmbH, Karlsruhe, Germany), 1% sodium deoxycholate (Carl Roth GmbH, Karlsruhe, Germany), 1% Triton X-100 (Merck, Darmstadt, Germany), and Protease Inhibitor I and Protease Inhibitor II (Thermo Fisher Scientific, Waltham, MA, USA). The samples were shaken for 2 h at 4 °C followed by centrifugation at 12,000 RPM for 20 min at 4 °C. The samples were filtered using syringe filters (1 μ m, 0.45 μ m and 0.1 μ m). The concentration was determined using the BC assay protocol (Pierce™ BCA Protein Assay Kit, Thermo Fisher Scientific, Waltham, MA, USA). The same protein amount (50 μ g) was loaded into the wells of the gel under unreduced conditions (SERVAGel™ TG 8% PRiME™, Heidelberg, Germany) and separated in the running gel system (SERVA™ Heidelberg, Germany) at a voltage of 70 V for 60 min followed by 60 min at 160 V in running buffer (250 mM TrisBase (Carl Roth GmbH, Karlsruhe, Germany), 1.92 M glycine (Carl Roth GmbH, Karlsruhe, Germany), and 1% SDS (Carl Roth GmbH, Karlsruhe, Germany)). Subsequently, the proteins were transferred from sodium dodecyl sulphate (SDS) gel to a nitrocellulose membrane (Trans-Blot® Turbo™ RTA Mini PVDF Transfer Kit, Bio-Rad Laboratories, Hercules, CA, USA). The blot system, Trans-Blot® Turbo™ (Bio-Rad, Laboratories, Hercules, CA, USA), was used. A 5% skimmed milk powder (Carl Roth GmbH, Karlsruhe, Germany) in 0.05% PBS-Tween20 (PBS-T) (Carl Roth GmbH, Karlsruhe, Germany) solution was used to block non-specific antibody binding. Incubation was performed at room temperature for 1 h. Blots were incubated with an antibody marker for macrophages, CD68 (Bio-rad MCA1957, Hercules, CA, USA), diluted 1:500 in 5% milk solution overnight at 4 °C. After washing the membrane three times with PBS-T, the blots were incubated with HRP-coupled Mouse IgGκlight chain binding protein diluted 1:5000 in PBS-T for 1 h. The band was detected using the membrane substrate (SeramunBlau® prec, Seramun Diagnostica GmbH, Heidesee, Germany). GAPDH (Invitrogen, Carlsbad, CA, USA) was used for charge control.

The intensity of the bands was measured with the software Image J (version: 1.53k).

2.12. Statistical Analysis

From all data, a mean inset was calculated and presented. The significance was compared by unpaired and bilateral t-test analysis and was indicated at $p < 0.05$. Statistics were performed using Microsoft Excel (version: 16.57; Microsoft, Washington, DC, USA).

3. Results

In this study, an iron-containing contrast agent was applied to mice with PCa to visualize macrophages in vivo on MRI. Two tumor sizes, 500 mm³ and 1000 mm³, were studied and compared. Figure 1 shows the study design.

All animals developed a tumor ($n = 28$). Although the amounts of cells and the time frame of the study were standardized, the animals developed the target tumor volume at different time points. To determine tumor size, the tumors were measured daily with a caliper or palpatory and documented. The final tumor size of 500 mm³ was reached between 30–58 days after surgery. The tumor size of 1000 mm³ was reached after 44–61 days after cell implantation.

3.1. Characterization in T2*-Weighted MR Imaging Using Superparamagnetic Iron-Oxide Particle

After a pre-scanning of the mouse in MRI, intravenous administration of 4 mg/kg ferumoxytol was performed via the tail vein. After 24 h, a second MRI examination was performed. The comparison between the pre-contrast and post-contrast images (Figure 2A,B) showed a signal loss after administration of ferumoxytol in the tumor tissue. Mice with a 500 mm³ tumor showed a higher signal loss than mice with a 1000 mm³ tumor after administration of ferumoxytol. In the group with a tumor volume of 500 mm³, the pre-contrast imaging demonstrated a signal loss (SI) of 721. After the administration of ferumoxytol, a

SI of 139 ($p < 0.001$) was shown (Figure 2C). In 1000 mm³ tumors, the SI before ferumoxytol administration was 521 compared to 204 after 24 h ($p < 0.001$) (Figure 2C). The RR was 0.8 in 500 mm³ tumors ($n = 14$) compared to a RR of 0.6 in 1000 mm³ tumors ($n = 14$).

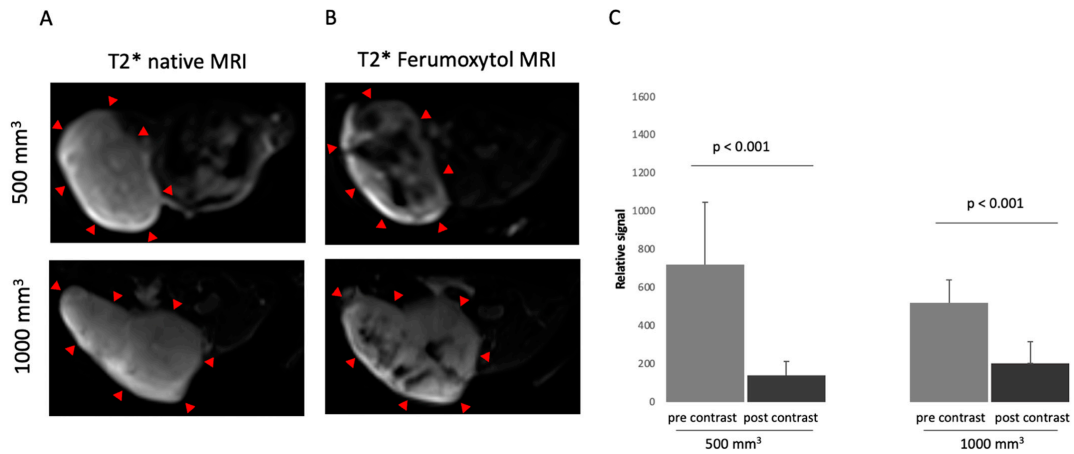


Figure 2. MRI images of prostate cancer in xenograft model of two different tumor sizes, 500 mm³ and 1000 mm³. (A) shows a representative native MRI image of a T2*-weighted sequence from the mouse that developed a tumor with a volume of 500 mm³ (top) and 1000 mm³ (bottom) in the scapula area of the mouse. Red arrows are pointing at the tumor. (B) shows a post-contrast T2*-weighted sequence with ferumoxytol from a tumor-bearing mouse after 24 h. Top: 500 mm³. Bottom: 1000 mm³. Red arrows show the tumor. (C) shows the analysis of MRI images (T2*-weighted sequence) before and after contrast agent administration (ferumoxytol) in two different tumor volumes (500 mm³ and 1000 mm³). A total of 14 animals per group were studied ($n = 14$).

3.2. Ex Vivo Analysis

In both tumor sizes, iron particles were detected in the tissue using Perls' Prussian blue stain (Figure 3A). The iron particles are shown in blue. To determine the iron content, three different areas were selected for each slide and the percentages of the presence of iron were determined using the analyzer. The analysis revealed a different amount of iron between the two tumor sizes. The 500 mm³ tumors had an average of 1.5% iron ($\sigma = 1.1$, $n = 14$), and the 1000 mm³ tumors showed only 0.4% iron ($\sigma = 0.2$, $n = 14$) (Figure 3D). The iron particles were distributed differently in the tumor tissues.

In addition, immunofluorescence staining by using antibodies to CD68 was performed (Figure 3B) to confirm the results. This showed that in 500 mm³ tumors the mean value was 9.6% CD68 ($\sigma = 1.1$, $n = 3$) and in 1000 mm³ tumors 5.2% ($\sigma = 0.9$; $n = 3$). Additional Western blot analysis was conducted in which the previous results were confirmed. A stronger expression of CD68 was detected in the 500 mm³ tumors, mean value of 703.7 ($n = 3$), than in the 1000 mm³ tumors, mean value of 304.8 ($n = 3$) (Figure 3E). The intensities of each band can be seen in the Supplementary Material. GAPDH was included as a control.

The in vivo MRI data (T2-weighted MR sequences) were correlated with the ex vivo data (percent Fe by Perls' Prussian staining). A correlation was found ($y = 0.025x + 0.76$; $R^2 = 0.74$) (Figure 4A).

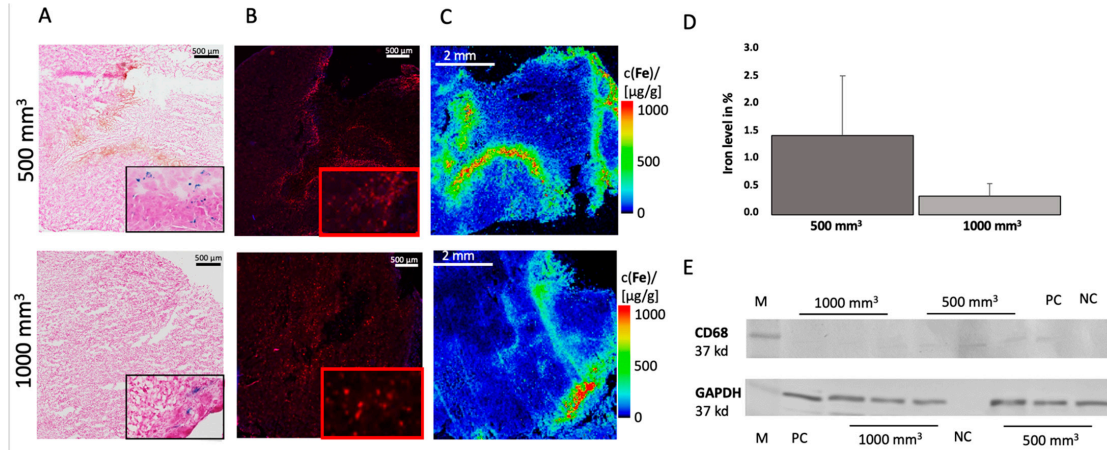


Figure 3. Ex vivo analysis of iron and CD68 in 500 mm³ and 1000 mm³ tumors. Top: 500 mm³. Bottom: 1000 mm³. (A) shows a Perls' Prussian blue stain from 500 mm³ tumor (top) and 1000 mm³ (bottom). Blue colored areas indicate iron particle. (B) shows immunofluorescence staining of CD68. Counterstaining was performed with DAPI. (C) LA-ICP MS was performed to localize iron particles. (D) The percentage of iron in the histological Perls' Prussian stain was determined. Three areas per slide were calculated and graphically displayed. Per group, *n* = 14 animals were analyzed. (E) A Western blot was performed for *n* = 3 tumors per group to detect the expression of CD68, 500 mm³ mean value of 703.7 and 1000 mm³ mean value of 304.8. A CD38 antibody was used, and GAPDAH was included as a control. M = marker, NC = negative control, PC = positive control. All the whole western blot figures can be found in the Figure S1.

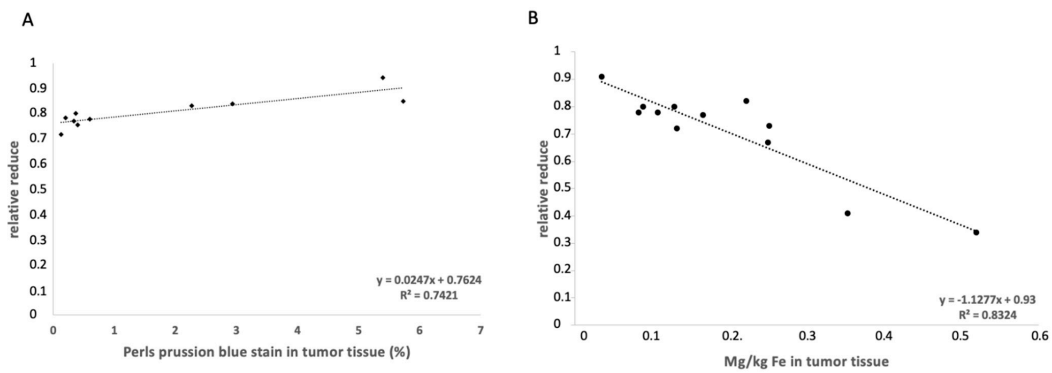


Figure 4. Correlation of the MRI data and the histological and elemental analysis. (A) The correlation between the Perls' Prussian blue staining percentage and the relative enhancements show a correlation ($y = 0.025x + 0.76$; $R^2 = 0.74$). (B) shows a correlation between the relative enhancement and the ICP-MS analyses for Fe. A correlation is shown ($y = -1.13x + 0.93$; $R^2 = 0.83$).

3.3. Elemental Analysis of Tumor Tissue with Specific Regard to Fe

LA-ICP-MS analysis was performed to localize Fe in the tumor tissue. For each tumor size, *n* = 3 animals were visualized. The LA-ICP-MS data showed good colocalization of the iron-oxide nanoparticles with the histological data, as shown in Figure 3C. Iron could be detected in the intra-tumoral space as well as in the peripheral region of the tumor.

There is an overlap between the immunofluorescence staining of CD68 and the LA-ICP-MS measurement for Fe (Figure 3A,B).

To accurately determine the concentration of Fe in the tissue, a quantitative ICP-MS analysis was conducted. The determined iron content in the tumor tissue was correlated with the MRI RR data, which showed a correlation ($y = -1.13x + 0.93$; $R^2 = 0.83$) (Figure 4B). For each group, $n = 6$ measurements were performed.

4. Discussion

This study investigated the feasibility of using a clinically applicable iron-based probe for molecular MRI as a signal-reducing substance (off-label) to image and characterize a PC3 tumor in vivo in a SCID mouse model. Two tumor volumes were compared, 500 mm³ and 1000 mm³. The results show that more iron particles were assimilated in the smaller tumor volume than in the larger ones. Regardless of tumor volume, both tumor volumes were found to take up iron. A clear differentiation between healthy and tumorous tissues was possible. The results could be confirmed by ex vivo examination methods.

In our study, we note a heterogeneous distribution of the iron-oxide particles in the tumor during MRI, which means that iron-oxide particles were not specifically found only in the periphery or in a specific area of the tumor. The histological results confirm this assumption. We could detect an overlap of the CD68 positive areas in the immunofluorescence with the positive Fe areas in the LA-ICP-MS measurement. Thus, it can be said that macrophages are able to take up ferumoxytol. We have already been able to show this in other diseases [21–23]. Some publications indicate that tumor-associated macrophages (TAMs) are able to take up administered nanoparticles [24,25]. TAMs account for about 50% of the total tumor mass [26]. They promote tumor growth by suppressing immunocompetent cells, inducing neovascularization, and supporting cancer stem cells [27]. TAMs can invade and distribute in the tumor mass so that they may be instrumental in diagnosis, treatment, and therapy. Daldrup-Link et al. demonstrated that ferumoxytol can be used to detect TAMs in MRI in a breast carcinoma mouse model [25].

In this study, a lower uptake of iron-oxide particles in the group with the tumor volume of 1000 mm³ was observed. A possible explanation for this is provided by a study by Franklin et al. [28]. They studied macrophages during growth in breast tumors. Among other things, a distinction between TAMs and breast tissue macrophages (MTMs) was investigated using different methods. This showed a correlation between increase in tumor volume with decrease in MTMs [28,29]. Further studies could prove that there is a correlation between the aggressiveness of the prostate tumor and an increased occurrence of TAMs [11,30]. The exact role of TAMs in different types of cancers has not been fully clarified. The role of TAMs in PCa progression is multifactorial, including involved in tumor invasion, increase tumor angiogenesis, tumor proliferation, tumor metastasis, and immune suppression [31,32]. Thus, our results suggest that although TAMs are able to initialize foreign particles, other functions take precedence in increasing tumor volume. Further research is needed to fully understand the role of TAMs in PCa progression and to determine which functions TAMs prioritize at which stage of tumor progression.

Another reason for the lower uptake of iron particles in tumors with a larger volume can be due to necrosis inside a tumor. With the progression of tumor growth, necrosis plays an important role. An important aspect is tumor necrosis factor- α (TNF- α), which influences tumorigenesis and tumor progression [33,34]. High TNF and interleukin-6 (IL-6) levels, which are known to be responsible for the proliferation and metastatic potential of tumor cells, indicate a negative prognosis for the patient [35]. Maolake et al. were able to demonstrate a TNF- α loop in PC3 cells in their study [36]. A high TNF- α concentration inhibited PC3 proliferation, a low TNF- α concentration caused an upregulation of C-C chemokine receptor, which is significantly associated with lymph node metastasis [37,38]. Our study did not investigate these factors, which is a limitation. Further studies are needed to fully investigate the tumor microenvironment after ferumoxytol administration.

Magnetic iron-oxide particles can be used as off-label MRI contrast agents in the clinical setting. In particular, ferumoxytol is currently used as an MRI contrast agent because it has all the positive properties of iron-oxide nanoparticles, including long blood-retention time, biodegradability, and low toxicity [39]. Additionally, the surface coating of iron-oxide nanoparticles can be modified to achieve specific binding. Thus, conjugation of specific tumor binders to iron-oxide nanoparticles can yield to targeted tumor contrast agents. In addition to magnetic and crystalline properties, the essential properties of iron-oxide nanoparticles must also be considered, such as size, surface charge, and lipophilicity [40]. Iron is a physiologically ubiquitous element in the mammalian body and is more easily metabolized than the conventionally used gadolinium-based contrast agents [41].

Ferumoxytol is mainly used as a replacement therapy in the treatment of anemia. In addition, it can also be used in MRI. In a study by Zanganeh et al., the therapeutic effect of the iron-oxide nanoparticles on the growth of early breast cancer and lung cancer metastases in liver and lung was also investigated [24]. The in vivo experiments showed inhibition of subcutaneous adenocarcinoma growth in mice by administration of ferumoxytol. Intravenous administration of ferumoxytol prevented development of liver metastases. An increased presence of M1 macrophages in tumor tissue was determined [24]. The study shows that ferumoxytol can be used in a variety of medical applications.

The tumor microenvironment is essential for progression and metastasis [24,42,43]. Elemental iron plays an important role in this process. In cancers, iron supply, export, and storage are usually impaired [42]. Targeted iron metabolism could be an innovative approach to treat cancer [42].

Ferumoxytol is not only used in imaging techniques for tumor diseases but may also have applications in cardiovascular diseases [21,22,44] and the central nervous system [15]. Different studies have investigated the molecular properties of cardiovascular disease with a combined approach using iron-oxide nanoparticles and a gadolinium-based contrast agent [21,22,44]. A limitation that needs to be considered regarding ferumoxytol is that it is not prostate tumor specific or even tumor specific. A possible solution would be a conjugation with a disease- or tumor-specific antibody [45]. This would require determining the appropriate targeting ligands for PCa, possible examples being the PSA antigen, alpha-methylacyl-CoA racemase [46], or prostate stem cell antigen [47].

In this context, our study shows that MRI visualization with ferumoxytol is possible in PCa and that there is a heterogeneous distribution in the tumor. This method could be used in combination with other diagnostic methods for non-invasive assessment of the molecular nature of PCa.

5. Limitations

The study was performed in a xenograft model. An orthotopic mouse model would allow the tumor in the target tissue and thus in a natural microenvironment to be studied. Ferumoxytol is not prostate cancer specific and can also be used as an MRI-contrast agent for other diseases. In addition, this study only investigated the feasibility of ferumoxytol in PCa, and a full investigation of the tumor microenvironment after administration of the contrast agent would have to follow.

6. Conclusions

Our study demonstrates a visualization with ferumoxytol, an iron-oxide nanoparticle probe, is feasible for prostate cancer. The study shows that macrophages in smaller tumors take up more iron than in larger tumors. This non-invasive method could help to detect tumors and to identify molecular characteristics.

Supplementary Materials: The following supporting information can be downloaded at: <https://www.mdpi.com/article/10.3390/cancers14122909/s1>, Figure S1. Western Blot analysis.

Author Contributions: Conceptualization, A.K. and M.R.M.; methodology, A.K. and M.R.M.; performed experiments, A.K., J.B., J.O.K., J.S., R.B. and H.T., writing original draft preparation, A.K.; writing–review and editing J.O.K., D.B.M., L.C.A., J.B., C.R., J.Z., J.M., J.S., H.T., R.B., U.K., B.H. and M.R.M.; project administration, M.R.M.; funding acquisition, M.R.M., B.H. and H.T. All authors have read and agreed to the published version of the manuscript.

Funding: This research was partly funded by the Sonderforschungsbereich (SFB), Deutsche Forschungsgemeinschaft (DFG, German Research Foundation)—SFB 1340/1 2018, B01 and C02 (BAM).

Institutional Review Board Statement: This study was performed corresponding the local guidelines and provisions for the implementation of the Animal Welfare Act and regulations of the Federation of Laboratory Animal Science Associations (FELASA). This animal study has been approved by the regulatory authority of the Regional Office for Health and Social Affairs Berlin (LAGeSo) (G0094/19; 04.04.2019).

Informed Consent Statement: Not applicable.

Data Availability Statement: The data presented in this study are available on request from the corresponding author.

Acknowledgments: All authors are grateful for financial support from the DFG–German Research Foundation.

Conflicts of Interest: The authors declare no conflict of interest.

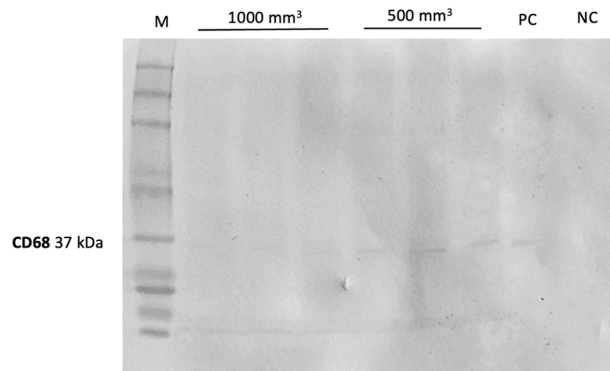
References

1. Siegel, R.L.; Miller, K.D.; Fuchs, H.E.; Jemal, A. Cancer Statistics, 2021. *CA Cancer J. Clin.* **2021**, *71*, 7–33. [\[CrossRef\]](#)
2. Duffy, M.J. Biomarkers for prostate cancer: Prostate-specific antigen and beyond. *Clin. Chem. Lab. Med.* **2020**, *58*, 326–339. [\[CrossRef\]](#) [\[PubMed\]](#)
3. Zhao, J.; Mangarova, D.B.; Brangsch, J.; Kader, A.; Hamm, B.; Brenner, W.; Makowski, M.R. Correlation between Intraprostatic PSMA Uptake and MRI PI-RADS of [(68)Ga] Ga-PSMA-11 PET/MRI in Patients with Prostate Cancer: Comparison of PI-RADS Version 2.0 and PI-RADS Version 2.1. *Cancers* **2020**, *12*, 3523. [\[CrossRef\]](#) [\[PubMed\]](#)
4. Zhao, S.; Yu, X.; Qian, Y.; Chen, W.; Shen, J. Multifunctional magnetic iron oxide nanoparticles: An advanced platform for cancer theranostics. *Theranostics* **2020**, *10*, 6278–6309. [\[CrossRef\]](#) [\[PubMed\]](#)
5. Figuerola, A.; Di Corato, R.; Manna, L.; Pellegrino, T. From iron oxide nanoparticles towards advanced iron-based inorganic materials designed for biomedical applications. *Pharmacol. Res.* **2010**, *62*, 126–143. [\[CrossRef\]](#)
6. Gazeau, F.; Lévy, M.; Wilhelm, C. Optimizing magnetic nanoparticle design for nanothermotherapy. *Nanomedicine* **2008**, *3*, 831–844. [\[CrossRef\]](#)
7. Gupta, A.K.; Gupta, M. Synthesis and surface engineering of iron oxide nanoparticles for biomedical applications. *Biomaterials* **2005**, *26*, 3995–4021. [\[CrossRef\]](#)
8. Wang, G.; Serkova, N.J.; Groman, E.V.; Scheinman, R.I.; Simberg, D. Feraheme (Ferumoxytol) Is Recognized by Proinflammatory and Anti-inflammatory Macrophages via Scavenger Receptor Type AI/II. *Mol. Pharm.* **2019**, *16*, 4274–4281. [\[CrossRef\]](#)
9. Lin, Y.; Xu, J.; Lan, H. Tumor-associated macrophages in tumor metastasis: Biological roles and clinical therapeutic applications. *J. Hematol. Oncol.* **2019**, *12*, 76. [\[CrossRef\]](#)
10. Zhou, J.; Tang, Z.; Gao, S.; Li, C.; Feng, Y.; Zhou, X. Tumor-Associated Macrophages: Recent Insights and Therapies. *Front. Oncol.* **2020**, *10*, 188. [\[CrossRef\]](#)
11. Lissbrandt, I.F.; Stattin, P.; Wikström, P.; Damber, J.-E.; Egeva, L.; Bergh, A. Tumor associated macrophages in human prostate cancer: Relation to clinicopathological variables and survival. *Int. J. Oncol.* **2000**, *17*, 445–496. [\[CrossRef\]](#)
12. Ramanathan, R.K.; Korn, R.L.; Raghunand, N.; Sachdev, J.C.; Newbold, R.G.; Jameson, G.; Fetterly, G.J.; Prey, J.; Klinz, S.G.; Kim, J.; et al. Correlation between Ferumoxytol Uptake in Tumor Lesions by MRI and Response to Nanoliposomal Irinotecan in Patients with Advanced Solid Tumors: A Pilot Study. *Clin. Cancer Res.* **2017**, *23*, 3638–3648. [\[CrossRef\]](#)
13. Harisinghani, M.; Ross, R.W.; Guimaraes, A.R.; Weissleder, R. Utility of a New Bolus-injectable Nanoparticle for Clinical Cancer Staging. *Neoplasia* **2007**, *9*, 1160–1165. [\[CrossRef\]](#)
14. McConnell, H.L.; Schwartz, D.L.; Richardson, B.E.; Woltjer, R.L.; Muldoon, L.L.; Neuwelt, E.A. Ferumoxytol nanoparticle uptake in brain during acute neuroinflammation is cell-specific. *Nanomedicine* **2016**, *12*, 1535–1542. [\[CrossRef\]](#)
15. Toth, G.B.; Varallyay, C.G.; Horvath, A.; Bashir, M.R.; Choyke, P.L.; Daldrup-Link, H.E.; Dosa, E.; Finn, J.P.; Gahramanov, S.; Harisinghani, M.; et al. Current and potential imaging applications of ferumoxytol for magnetic resonance imaging. *Kidney Intern.* **2017**, *92*, 47–66. [\[CrossRef\]](#)
16. Tse, B.W.-C.; Cowin, G.J.; Soekmadji, C.; Jovanovic, L.; Vasireddy, R.S.; Ling, M.-T.; Khatri, A.; Liu, T.; Thierry, B.; Russell, P.J. PSMA-targeting iron oxide magnetic nanoparticles enhance MRI of preclinical prostate cancer. *Nanomedicine* **2015**, *10*, 375–386. [\[CrossRef\]](#)

17. Bates, D.; Abraham, S.; Campbell, M.; Zehbe, I.; Curiel, L. Development and characterization of an antibody-labeled superparamagnetic iron oxide contrast agent targeting prostate cancer cells for magnetic resonance imaging. *PLoS ONE* **2014**, *9*, e97220. [[CrossRef](#)]
18. Zhu, Y.; Sun, Y.; Chen, Y.; Liu, W.; Jiang, J.; Guan, W.; Zhang, Z.; Duan, Y. In Vivo Molecular MRI Imaging of Prostate Cancer by Targeting PSMA with Polypeptide-Labeled Superparamagnetic Iron Oxide Nanoparticles. *Int. J. Mol. Sci.* **2015**, *16*, 9573–9587. [[CrossRef](#)]
19. Nagesh, P.K.B.; Johnson, N.R.; Boya, V.K.N.; Chowdhury, P.; Othman, S.F.; Khalilzad-Sharghi, V.; Hafeez, B.B.; Ganju, A.; Khan, S.; Behrman, S.W.; et al. PSMA targeted docetaxel-loaded superparamagnetic iron oxide nanoparticles for prostate cancer. *Colloids Surf. B Biointerfaces* **2016**, *144*, 8–20. [[CrossRef](#)]
20. Knobloch, G.; Colgan, T.; Wiens, C.N.; Wang, X.; Schubert, T.; Hernando, D.; Sharma, S.D.; Reeder, S.B. Relaxivity of Ferumoxytol at 1.5 T and 3.0 T. *Investig. Radiol.* **2018**, *53*, 257–263. [[CrossRef](#)]
21. Brangsch, J.; Reimann, C.; Kaufmann, J.O.; Adams, L.C.; Onthank, D.C.; Thone-Reineke, C.; Robinson, S.P.; Buchholz, R.; Karst, U.; Botnar, R.M.; et al. Concurrent Molecular Magnetic Resonance Imaging of Inflammatory Activity and Extracellular Matrix Degradation for the Prediction of Aneurysm Rupture. *Circ. Cardiovasc. Imaging* **2019**, *12*, e008707. [[CrossRef](#)]
22. Mockel, J.; Brangsch, J.; Reimann, C.; Kaufmann, J.O.; Sack, I.; Mangarova, D.B.; Kader, A.; Taupitz, M.; Adams, L.C.; Keller, S.; et al. Assessment of Albumin ECM Accumulation and Inflammation as Novel In Vivo Diagnostic Targets for Multi-Target MR Imaging. *Biology* **2021**, *10*, 964. [[CrossRef](#)]
23. Reimann, C.; Brangsch, J.; Kaufmann, J.O.; Adams, L.C.; Onthank, D.C.; Thone-Reineke, C.; Robinson, S.P.; Hamm, B.; Botnar, R.M.; Makowski, M.R. Dual-probe molecular MRI for the in vivo characterization of atherosclerosis in a mouse model: Simultaneous assessment of plaque inflammation and extracellular-matrix remodeling. *Sci. Rep.* **2019**, *9*, 13827. [[CrossRef](#)]
24. Zanganeh, S.; Hutter, G.; Spittler, R.; Lenkov, O.; Mahmoudi, M.; Shaw, A.; Pajarinen, J.S.; Nejadnik, H.; Goodman, S.; Moseley, M.; et al. Iron oxide nanoparticles inhibit tumour growth by inducing pro-inflammatory macrophage polarization in tumour tissues. *Nat. Nanotechnol.* **2016**, *11*, 986–994. [[CrossRef](#)]
25. Daldrup-Link, H.E.; Golovko, D.; Ruffell, B.; Denardo, D.G.; Castaneda, R.; Ansari, C.; Rao, J.; Tikhomirov, G.A.; Wendland, M.F.; Corot, C.; et al. MRI of tumor-associated macrophages with clinically applicable iron oxide nanoparticles. *Clin. Cancer Res.* **2011**, *17*, 5695–5704. [[CrossRef](#)]
26. Cendrowicz, E.; Sas, Z.; Bremer, E.; Rygiel, T.P. The Role of Macrophages in Cancer Development and Therapy. *Cancers* **2021**, *13*, 1946. [[CrossRef](#)]
27. Serguei, V.; Galya, W.; Xin, W. Macrophages associated with tumors as potential targets and therapeutic intermediates. *Nanomedicine* **2014**, *9*, 695–707.
28. Franklin, R.A.; Liao, W.; Sarkar, A.; Kim, M.V.; Bivona, M.R.; Liu, K.; Pamer, E.G.; Li, M.O. The cellular and molecular origin of tumor-associated macrophages. *Science* **2014**, *344*, 921–925. [[CrossRef](#)]
29. Nielsen, S.R.; Schmid, M.C. Macrophages as Key Drivers of Cancer Progression and Metastasis. *Mediat. Inflamm.* **2017**, *2017*, 9624760. [[CrossRef](#)]
30. Nonomura, N.; Takayama, H.; Kawashima, A.; Mukai, M.; Nagahara, A.; Nakai, Y.; Nakayama, M.; Tsujimura, A.; Nishimura, K.; Aozasa, K.; et al. Decreased infiltration of macrophage scavenger receptor-positive cells in initial negative biopsy specimens is correlated with positive repeat biopsies of the prostate. *Cancer Sci.* **2010**, *101*, 1570–1573. [[CrossRef](#)]
31. Yuri, P.; Shigemura, K.; Kitagawa, K.; Hadibrata, E.; Risan, M.; Zulfiqar, A.; Soeroharjo, I.; Hendri, A.Z.; Danarto, R.; Ishii, A.; et al. Increased tumor-associated macrophages in the prostate cancer microenvironment predicted patients' survival and responses to androgen deprivation therapies in Indonesian patients cohort. *Prostate Int.* **2020**, *8*, 62–69. [[CrossRef](#)]
32. Lewis, C.E.; Pollard, J.W. Distinct role of macrophages in different tumor microenvironments. *Cancer Res.* **2006**, *66*, 605–612. [[CrossRef](#)]
33. Wu, S.; Boyer, C.M.; Whitaker, R.S.; Berchuck, A.; Wiener, J.R.; Weinberg, J.B.; Bast, R.C. Tumor Necrosis Factor as an Autocrine and Paracrine Growth Factor for Ovarian Cancer: Monokine Induction of Tumor Cell Proliferation and Tumor Necrosis Factor a Expression1. *Cancer Res.* **1993**, *53*, 1939–1944. [[PubMed](#)]
34. Liu, R.Y.; Fan, C.; Mitchell, S.; Chen, Q.; Wu, J.; Zuckerman, K.S. The role of type I and type II tumor necrosis factor (TNF) receptors in the ability of TNF-alpha to transduce a proliferative signal in the human megakaryoblastic leukemic cell line Mo7e. *Cancer Res.* **1998**, *58*, 2217–2223.
35. Adler, H.L.; McCurdy, M.A.; Kattan, M.W.; Timme, T.L.; Scardino, P.T.; Thompson, T.C. Elevated levels of circulating interleukin-6 and transforming growth factor-beta 1 in patients with metastatic prostatic carcinoma. *J. Urol.* **1999**, *161*, 182–187. [[CrossRef](#)]
36. Maolake, A.; Izumi, K.; Natsagdorj, A.; Iwamoto, H.; Kadomoto, S.; Makino, T.; Naito, R.; Shigehara, K.; Kadono, Y.; Hiratsuka, K.; et al. Tumor necrosis factor-alpha induces prostate cancer cell migration in lymphatic metastasis through CCR7 upregulation. *Cancer Sci.* **2018**, *109*, 1524–1531. [[CrossRef](#)] [[PubMed](#)]
37. Cassier, P.A.; Treilleux, I.; Bachelot, T.; Ray-Coquard, I.; Bendriss-Vermare, N.; Ménétrier-Caux, C.; Trédan, O.; Goddard-Léon, S.; Pin, J.-J.; Mignotte, H.; et al. Prognostic value of the expression of C-Chemokine Receptor 6 and 7 and their ligands in non-metastatic breast cancer. *BMC Cancer* **2011**, *11*, 213. [[CrossRef](#)]
38. Du, P.; Liu, Y.; Ren, H.; Zhao, J.; Zhang, X.; Patel, R.; Hu, C.; Gan, J.; Huang, G. Expression of chemokine receptor CCR7 is a negative prognostic factor for patients with gastric cancer: A meta-analysis. *Gastric Cancer* **2017**, *20*, 235–245. [[CrossRef](#)]

39. Peng, X.H.; Qian, X.; Mao, H.; Wang, A.Y.; Nie, S.; Shin, D.M. Targeted magnetic iron oxide nanoparticles for tumor imaging and therapy. *Int. J. Nanomed.* **2008**, *3*, 311–326.
40. Israel, L.L.; Galstyan, A.; Holler, E.; Ljubimova, J.Y. Magnetic iron oxide nanoparticles for imaging, targeting and treatment of primary and metastatic tumors of the brain. *J. Control. Release* **2020**, *320*, 45–62. [[CrossRef](#)]
41. Xue, X.; Bo, R.; Qu, H.; Jia, B.; Xiao, W.; Yuan, Y.; Vapniarsky, N.; Lindstrom, A.; Wu, H.; Zhang, D.; et al. A nephrotoxicity-free, iron-based contrast agent for magnetic resonance imaging of tumors. *Biomaterials* **2020**, *257*, 120234. [[CrossRef](#)] [[PubMed](#)]
42. Jung, M.; Mertens, C.; Tomat, E.; Brune, B. Iron as a Central Player and Promising Target in Cancer Progression. *Int. J. Mol. Sci.* **2019**, *20*, 273. [[CrossRef](#)] [[PubMed](#)]
43. Choi, J.Y.; Neuhofer, M.L.; Barnett, M.J.; Hong, C.C.; Kristal, A.R.; Thornquist, M.D.; King, I.B.; Goodman, G.E.; Ambrosone, C.B. Iron intake, oxidative stress-related genes (MnSOD and MPO) and prostate cancer risk in CARET cohort. *Carcinogenesis* **2008**, *29*, 964–970. [[CrossRef](#)] [[PubMed](#)]
44. Adams, L.C.; Brangsch, J.; Reimann, C.; Kaufmann, J.O.; Buchholz, R.; Karst, U.; Botnar, R.M.; Hamm, B.; Makowski, M.R. Simultaneous molecular MRI of extracellular matrix collagen and inflammatory activity to predict abdominal aortic aneurysm rupture. *Sci. Rep.* **2020**, *10*, 15206. [[CrossRef](#)]
45. Cheng, K.; Shen, D.; Hensley, M.T.; Middleton, R.; Sun, B.; Liu, W.; De Couto, G.; Marban, E. Magnetic antibody-linked nanomatchmakers for therapeutic cell targeting. *Nat. Commun.* **2014**, *5*, 4880. [[CrossRef](#)]
46. Zhou, M.C.A.; Kleer, C.; Lucas, P.; Rubin, M. Alpha-Methylacyl-CoA Racemase. *Am. J. Surg. Pathol.* **2002**, *26*, 926–931. [[CrossRef](#)]
47. Mazaris, E.; Tsiotras, A. Molecular Pathways in Prostate Cancer. *Nephro-Urol. Mon.* **2013**, *5*, 792–800. [[CrossRef](#)]

(A)



(B)

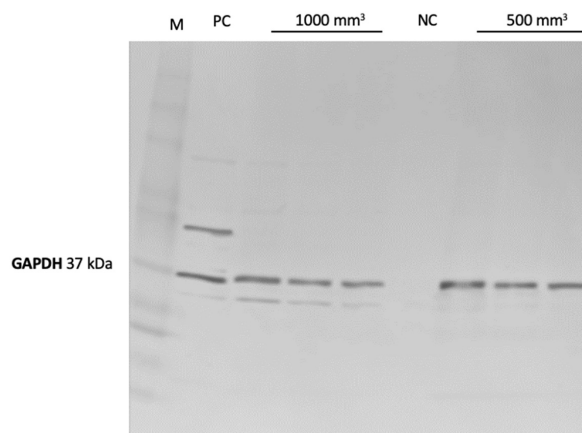


Figure S1. Western Blot analyse. **A:** Western Blot analyse for CD68. For each group, 3 tumors (n = 3 per group) were used for western blot analysis to detect the expression of CD68. Relative intensity from left to right: 290.1; 321.6; 302.7; 618; 966.0; 1144.4; PC: 1174.2. **B:** Western Blot analyse for GAPDH. For each group, 3 tumors (n = 3 per group) were used for western blot analysis to control protein levels.

5. Discussion

Molecular imaging is a non-invasive imaging modality, that provides information about the biological nature of tissues and pathological processes at the molecular and cellular levels. In the assessment of PCa, molecular imaging can be invaluable as the extracellular matrix and tumor microenvironment influence tumor progression. The ECM is responsible for tumor architecture [239] and is continuously changing [240].

5.1. Molecular MR imaging for diagnosis and characterization of PCa with an elastin-specific molecular probe

In carcinomas, the ECM is a network of macromolecules that are involved in the development of metastases, among other things [241]. The ECM structure in carcinomas is essential for understanding tumor development and thus for establishing diagnostic and therapeutic options [242]. Tumors are often characterized by stiffening due to high ECM deposition [241]. To progress, tumor cells must damage the ECM structure to migrate to other tissues and metastasize [243]. Matrix metalloproteinases (MMPs) are required to cleave ECM components. Matrikines activate MMPs, which are tumor-promoting [244].

The elasticity of tissue depends strongly on the ECM. In tumors, elasticity also plays a major function; for example, elastin is responsible for stability and tissue homeostasis [239]. Two elastin-binding proteins (EBPs), s-Gal and Galectin-3, mediate the expression and release of elastases [105].

This work showed that two groups with different PCa volumes, 500 mm³ and 1000 mm³, had different signal intensities (SI) on MRI measurement after injection of an elastin-specific molecular probe. A significantly higher SI was shown for smaller tumors than for larger tumors. Thus, it can be assumed that tumors with a larger volume express less elastic fibers, which can be a signal of future metastases [105]. Both MRI images and pathological examinations showed an irregular spatial distribution of elastic fibers over the whole PC3 tumor tissue. Regardless of the size of the tumor, more elastin was detected in the peripheral area than in the medial area of the tumor. In the MRI examinations, it was possible to make a clear differentiation between healthy and tumorous tissue. The Western blot analysis does not reflect the complete expression level of elastin. Elastin fibers are insoluble, which explains the weak bands. Elastin is a cross-linked polymer and breaking these cross-links is difficult. However, the soluble precursor tropoelastin can be detected in the Western blot. The Western blot in this study shows the expression of tropoelastin and coacervated elastin. The 500 mm³ tumors showed higher expression of new elastin compared

to the larger 1000 mm³ tumors. This observation correlates with immunofluorescence stains and with the higher MR signal in 500 mm³ tumors. Using the elastin-specific probe, an increased contrast could be measured in T1-weighted sequences, showing especially a high elastin density in the peripheral zone. The observations were confirmed by *ex vivo* investigations, immunofluorescence, laser ablation-inductively coupled plasma mass spectrometry (LA-ICP-MS), inductively-coupled plasma mass spectrometry (ICP-MS), and Elastica-van-Gieson staining.

High elastin levels play an important role in many cancers, for example, elastin promotes the invasiveness of human breast cancer cells [245]. More elastin has been detected in colorectal cancer compared to non-tumor colon tissues from the same patients. Elastin was found to critically regulate the tumor microenvironment and tumor development [246]. MMP9, MMP12, and TIMP3 were increased in the colon cancer cells. An elastin-specific molecular probe not only shows better characterization in tumor diseases but also provides better T1 imaging after injection of the molecular probe in cardiovascular diseases, such as aortic aneurysms and atherosclerosis [247-250]. In another study by Keller *et al.*, the elastin-specific molecular probe was visualized in VX2 hepatic tumors in a rabbit model, and the use of the molecular agent to differentiate specific tumors and peritumoral regions based on its ECM composition was confirmed [123, 251]. It was also shown that after thermal ablation of hepatic carcinomas in the VX2 model, molecular imaging with an elastin-specific probe is feasible and it provides an evaluation of ablation-induced remodeling of the ECM in the periphery of peri-ablation [252]. Another study by Sun *et al.* demonstrates the usefulness of the probe in renal fibrosis. The study was performed on several mouse models of renal fibrosis and fibrotic human kidneys. The elastin-specific probe enabled repeated and reproducible assessment of fibrosis and longitudinal monitoring during the therapeutic intervention [253]. Here, the potential for the specific probe to serve as a non-invasive specific imaging modality for the assessment of renal fibrosis was demonstrated [253]. Recently, a molecular agent targeting tropoelastin cross-linking (Gd₄-TESMA) has been synthesized. Thereby, the tropoelastin-binding peptide (TESMA) was conjugated to four Gd (III)-DOTA- moieties [254]. Gd₄-TESMA accumulates in atherosclerotic plaques in the murine model of plaque progression [254]. The molecular agent showed good binding affinity to tropoelastin and a serum half-life of more than 2 h [254]. Whether the probe also provides good imaging in PCa needs to be researched.

The results from the first part of this work show detection of tumors with elastin in a clinical MRI setup, which generates statements about the tumor volume and allows predictions about the further course of the tumor progression. Molecular imaging with an elastin-specific gadolinium-

based molecular probe in PCa is feasible. The study confirms an apparent loss of elastin in tumors with a larger volume. Such an imaging approach could be useful in predicting metastases.

5.2. Superparamagnetic iron-oxide nanoparticle for visualization of PCa in MRI

Ferumoxytol, while initially developed as an anemia treatment drug, is widely used as an off-label MRI molecular probe nowadays. Ferumoxytol shows good pharmacological properties, such as a long blood retention time, biodegradability, and low toxicity, which are all favorable for an MRI molecular probe [255]. Due to its high transverse relaxation activity, ferumoxytol produces negative contrast in the cellular uptake of these ultra-small superparamagnetic iron-oxide nanoparticles (uSPIONs) in T2-weighted MRI.

In this doctoral thesis, ferumoxytol was used off-label as a negative imaging MRI probe to visualize and characterize a PC3 tumor in a xenograft tumor-bearing mouse model. It was demonstrated that both the small and larger tumors took up iron-oxide nanoparticles. The focus was on the comparison between two tumor volumes, 500 mm³ and 1000 mm³. It was demonstrated that in smaller tumor volumes more iron particles were assimilated to a higher extent than in larger tumor volumes. In addition, a clear differentiation between healthy and tumorous tissue could be seen in the MR images. Heterogeneous distribution of the iron-oxide particles was observed, which means that the particles could be visualized both peripheral and intracorporeal in the tumor. With the help of pathological examinations, the results of the *in vivo* examination could be confirmed. An overlap of the CD68-positive areas in the immunofluorescence with the positive Fe areas in the LA-ICP-MS measurement was found. CD68 is a histochemical marker for macrophages [256, 257]. By this co-localization, it can be concluded that macrophages can take up ferumoxytol. Previous studies have shown the uptake of ferumoxytol in other diseases, such as aortic aneurysms or atherosclerosis [249, 250, 258]. Ferumoxytol is not only used preclinically but also clinically, as it already has had a marketing license since 2012 for anemia treatment. *Iv et al.* examined patients with high-grade malignant gliomas [259]. For this purpose, they administered 5 mg/kg ferumoxytol intravenously and carried out an MRI measurement after 24 h. Samples were then taken and analyzed histopathological, whereas the iron-oxide nanoparticles were only found in the macrophages [259]. MRI measures of sensitivity after ferumoxytol administration correlate with the concentration of macrophages that have taken up iron [259]. Ferumoxytol shows potential as a quantitative biomarker of macrophages in malignant gliomas.

Ferumoxylol-enhanced MR imaging has also been detected and quantified in lymphomas and bone sarcomas of pediatric patients [260]. Recently, ferumoxylol was shown to be useful as an additional diagnostic tool in differentiating intrapancreatic splenules from other pancreatic lesions [261]. However, larger cohorts of patients need to be studied to confirm this observation. A comparative study was conducted to determine whether ferumoxylol-enhanced MRI is as effective as gadolinium-enhanced MRI in detecting intracranial metastatic disease.

Preclinical studies such as those by Sillerud *et al.* show that ferumoxylol was phagocytosed by TAMs in a breast cancer mouse model [262]. They were able to make statements about the TAM density in tumor tissue using MRI evaluation and pathological examination (anti-F4/80 immunohistochemistry and iron staining). Other studies could confirm these results [263]. Further publications confirm the assumption that TAMs are able to take up nanoparticles [263, 264]. The tumor mass consists of about 50% TAMs [265]. TAMs promote tumor growth by suppressing immunocompetent cells, inducing neovascularization, and supporting cancer stem cells [266]. The presence of TAMs in the tumor mass makes them a good target for diagnosis, treatment, and therapy.

In this doctoral thesis, lower uptake of the iron-oxide particles was observed in the group with 1000 mm³ PC3 tumors [242]. A possible explanation for this is provided by a study by Franklin *et al.* who evaluated macrophages during breast cancer growth [242, 267]. As tumor volume increased, the presence of breast cancer macrophages (MTMs) decreased [242, 267, 268]. A correlation between the aggressiveness of the tumor and an increased incidence of TAMs has been demonstrated in prostate tumors [242, 269, 270]. Therefore, the obtained data suggest that TAMs can internalize foreign particles, but other functions play a more important role in the increase of the tumor volume [242]. To fully understand the role of TAMs in PCa progression and to find out which functions TAMs prioritize at which tumor stage of tumor progression still needs to be studied. Another explanation for the lower uptake of iron-oxide particles in the 1000 mm³ tumors may also be necrosis in tumors. Necrosis usually develops at an advanced stage due to the expression of TNF- α . It influences tumorigenesis and progression [242, 271, 272]. High TNF- α and interleukin-6 (IL-6) levels suggest a negative outlook for the patient [242, 273]. A high TNF- α concentration inhibits the proliferation of PC3 cells. A low TNF- α level upregulates C-C chemokine receptors, which is significantly associated with lymph node metastasis [274, 275].

All these studies and numerous others show the enormous potential of iron-oxide nanoparticles in MRI in the diagnosis of multiple diseases, including tumors. The surface coating of iron-oxide

nanoparticles can be changed to obtain a specific binding [63]. Teh *et al.* conjugated ferumoxytol with a fluorescent marker and PCa targeting agent heptamethine carbocyanine, under the name HMC-FMX nanoprobe [276]. Experiments were conducted in subcutaneous and orthotopic PCa mouse models [276]. However, the conjugate was not investigated in an MRI but by near-infrared fluorescence imaging, for better differentiation and visualization of tumor margins [276].

In addition to magnetic and crystalline characteristics, factors such as size, surface charge, and lipophilicity must also be included in the modification of iron-oxide nanoparticles [277]. Iron is a physiologically ubiquitous element in the body of mammals and is more lightly metabolized than Gd³⁺ based imaging probe [278]. Studies in healthy patients showed measurable amounts of residual iron on MRI, ranging from 3 to more than 11 months, after administration of ferumoxytol in healthy subjects [279]. This limitation can lead to misdiagnosis [279].

Ferumoxytol shows a therapeutic effect of the iron-oxide particles on breast cancer growth, and lung cancer metastases in the liver and lungs. Zanganeh *et al.* showed inhibition of subcutaneous adenocarcinoma growth after intravenous administration of ferumoxytol in a mouse model [264]. The administration prevented the development of liver metastases [264]. Further experimental work showed high levels of M1 macrophages [264]. Ferumoxytol can be used in a variety of medical interventions [264].

In principle, ferumoxytol shows enhanced MRI and is clinically immediately applicable. The study shows that MRI imaging with ferumoxytol is possible in primary PCa and that there is a heterogenic distribution of iron-oxide particles in the tumor. Histological examinations confirm the hypothesis that the signal reduction was caused due to the uptake of the molecular probe in macrophages in the tumor tissue. The obtained results from the study have the potential for translation into prostate cancer diagnosis.

5.3. Current and future trends in molecular imaging of prostate carcinoma

Molecular imaging using the elastin-specific molecular probe and iron-oxide nanoparticles can help to identify a tumor at an early stage by showing morphological changes in the target tissue. It can also be used to initiate appropriate therapies. Molecular visualization of biological or cellular changes or characteristics of the tumor can be performed without invasive surgery. Currently, molecular imaging methods are focused on the metabolism of cells, hormone receptors, and membrane proteins [112]. Tumor cells compared to healthy cells have differences in cell metabolism, which can be used for molecular imaging. Therefore, mainly radioactively labeled analogues of the metabolic substrates acetate [280-283], amino acids [284-288], choline [281, 289-291], glucose [292-295] and nucleosides [296, 297] are being investigated [63, 112]. However,

these metabolites are not specific for PCa, as some also occur in benign prostatic hyperplasia [298]. Pu *et al.* demonstrated the applicability of a protein MRI molecular probe (ProCA), which targeted PSMA [70]. The targeted molecular probe showed good Gd³⁺ binding affinity, metal selectivity and relaxivity, and strong PSMA targeting [63]. The experiments were performed in tumor-bearing mice, xenograft model, on a 7 T MRI. The results are promising and can be implemented for the early detection of PCa. However, further experiments in animal models have to follow to investigate the applicability in the target organ.

In addition, other components of the ECM, including collagen, laminins, fibronectin, and proteoglycans, may also have applications for the molecular imaging of PCa. For example, a molecular probe targeting collagen type 1 already exists. For the first time, the cyclic collagen molecular probe was investigated in a fibrosis-myocardial infarction mouse model by Caravan *et al.* [299]. The collagen-specific molecular probe was specific and showed high contrast for fibrotic tissue scars [299]. The molecular probe can be used to detect and evaluate a diverse range of diseases associated with fibrosis and extracellular matrix remodeling [299-301]. Not only cardiovascular diseases could be imaged with a collagen-specific probe but also tumors, such as fibrosis in pancreatic adenocarcinomas [302, 303] in lung or liver fibrosis [304]. About PCa, the applicability of the collagen probe needs to be reviewed. Due to the function of collagen in prostate cancer and the association of collagen with the pathological stage, the use of a collagen-specific probe can be very helpful [305].

Ye *et al.* reported a peptide-based molecular probe targeted for molecular imaging of the fibronectin-fibrin complex [306]. The studies were performed in a colorectal cancer xenograft mouse model. Meanwhile, there are numerous studies with promising results with a potential translational application for the development of fibrin probes for the detection of tumorous diseases as well as for the evaluation of thrombi [216, 307-310]. Recently, a new MRI molecular probe targeting extra domain B fibronectin was reported to be overexpressed in aggressive tumors [216]. Four small peptides were identified (GVK, IGK, SGV, and ZD2) specific for extra domain-B fibronectin, and these were conjugated to be visualizable on MRI. A PC3 mouse xenograft model was used. The results show improved tumor contrast on MRI.

Currently, molecular imaging is mostly performed using PET [311-313]. But there is continuous research to synthesize, modify and optimize MRI molecular probes for molecular imaging [307, 314]. To date, there are only preclinical studies with gadolinium-based molecular probes. Much research has been done in the field of molecular research over the last 30 years and many promising biomarker-targeted molecular imaging probes have been developed and successfully

tested in proof-of-concept animal studies [315]. However, so far, none has received clinical approval because of many challenges in implementation. This is mainly due to the safety profile related to metal toxicity and deposition of the imaging probe. When developing new biomarkers, it is important to have a low molecular weight to initiate rapid release in the blood and induce strong tumor and tissue penetration. They must also have high thermodynamic stability, high affinity, and specificity for the desired target. In contrast, ferumoxytol already has clinical approval and can therefore be used in patients. So far, no data have been collected regarding the use of ferumoxytol in patients with prostate carcinoma for tumor characterization. Some studies have conjugated ferumoxytol with a fluorescent dye (HMC-FMX) to perform MR lymphography in patients [276]. Using HMC-FMX, intraoperative and postoperative assessment of the peripheral area of the tumor was possible. Thus, the previous studies are dedicated to the use of ferumoxytol in patients with PCa to detect lymph nodes [316-322]. With regard to the primary assessment of PCa, further clinical studies are warranted.

With the help of molecular imaging methods, it is possible to make individual disease predictions without the need to take tissue samples from the organism. This can reduce invasive procedures and possible complications. Molecular imaging shows potential as an adjunct to existing commercial diagnostic tools, with the major advantage of providing a non-invasive assessment at the cellular level.

5.4. Limitations

In this study, xenograft models were used to demonstrate the visualization of the molecular probes. In order to also study and analyze the tumor microenvironment, it is necessary to use an orthotropic mouse model. This will make it possible to grow a tumor in the target tissue, the prostate, and decode the complete tumor microenvironment. In addition, analysis of secreted proteins, such as MMPs, would be another methodology to understand elastin degradation. To determine necrosis in the tumor, further methods are also necessary. These were not investigated in the present studies, which is a limitation.

It has been shown that the molecular probe can be used in PCa, but other studies also show the applicability of the molecular probes in other diseases, such as cardiovascular diseases or fibrosis. Therefore, the molecular probes are not specific for prostate cancer. In addition, the deposition of the elastin-specific molecular probe should be assessed after multiple administrations in different organs to investigate the possible toxicity of the molecular probe. A long-term study is also useful

Discussion

for ferumoxytol, although the long residence time of the particles in the tissue may result in a misleading evaluation.

6. References

1. Siegel RL, Miller KD, Fuchs HE, Jemal A. Cancer Statistics, 2021. *CA Cancer J Clin.* 2021;71(1):7-33.
2. Siegel RL, Miller KD, Fuchs HE, Jemal A. Cancer statistics, 2022. *CA Cancer J Clin.* 2022;72(1):7-33.
3. Institut R-K. Prostata. 2021 29.11.2021. In: Krebs in Deutschland [Internet]. Robert-Koch Institut; [106-9]. Available from: https://www.krebsdaten.de/Krebs/DE/Content/Publikationen/Krebs_in_Deutschland/krebs_in_deutschland_node.html.
4. Anamthathmakula P, Winuthayanon W. Mechanism of semen liquefaction and its potential for a novel non-hormonal contraception dagger. *Biol Reprod.* 2020;103(2):411-26.
5. Burden HP, Holmes CH, Persad R, Whittington K. Prostatosomes--their effects on human male reproduction and fertility. *Hum Reprod Update.* 2006;12(3):283-92.
6. Sauer AK, Vela H, Vela G, Stark P, Barrera-Juarez E, Grabrucker AM. Zinc Deficiency in Men Over 50 and Its Implications in Prostate Disorders. *Front Oncol.* 2020;10:1293.
7. Boyle P, Severi G, Giles GG. The epidemiology of prostate cancer. *Urologic Clinics of North America.* 2003;30(2):209-17.
8. Yin M, Bastacky S, Chandran U, Becich MJ, Dhir R. Prevalence of incidental prostate cancer in the general population: a study of healthy organ donors. *J Urol.* 2008;179(3):892-5; discussion 5.
9. Jones RA, Wenzel J. Prostate cancer among African-American males: understanding the current issues. *J Natl Black Nurses Assoc.* 2005;16(1):55-62.
10. Bostwick DG, Burke HB, Djakiew D, Euling S, Ho SM, Landolph J, Morrison H, Sonawane B, Shifflett T, Waters DJ, Timms B. Human prostate cancer risk factors. *Cancer.* 2004;101(10 Suppl):2371-490.
11. Haqq C, Li R, Khodabakhsh D, Frolov A, Ginzinger D, Thompson T, Wheeler T, Carroll P, Ayala G. Ethnic and racial differences in prostate stromal estrogen receptor alpha. *Prostate.* 2005;65(2):101-9.
12. Platz EA, Giovannucci E. The epidemiology of sex steroid hormones and their signaling and metabolic pathways in the etiology of prostate cancer. *J Steroid Biochem Mol Biol.* 2004;92(4):237-53.
13. Shen MM, Abate-Shen C. Molecular genetics of prostate cancer: new prospects for old challenges. *Genes Dev.* 2010;24(18):1967-2000.
14. Huggins C, Clarence V, Hodges. Studies on prostatic cancer. I. The effect of castration, of estrogen and of androgen injection on serum phosphatases in metastatic carcinoma of the prostate. *cancer reserach.* 1941;1.4:293-7.
15. Imamoto T, Suzuki H, Yano M, Kawamura K, Kamiya N, Araki K, Komiya A, Nihei N, Naya Y, Ichikawa T. The role of testosterone in the pathogenesis of prostate cancer. *Int J Urol.* 2008;15(6):472-80.
16. Crawford ED, Heidenreich A, Lawrentschuk N, Tombal B, Pompeo ACL, Mendoza-Valdes A, Miller K, Debruyne FMJ, Klotz L. Androgen-targeted therapy in men with prostate cancer: evolving practice and future considerations. *Prostate Cancer Prostatic Dis.* 2019;22(1):24-38.

References

17. Bolton EC, So AY, Chaivorapol C, Haqq CM, Li H, Yamamoto KR. Cell- and gene-specific regulation of primary target genes by the androgen receptor. *Genes Dev.* 2007;21(16):2005-17.
18. Michaud JE, Billups KL, Partin AW. Testosterone and prostate cancer: an evidence-based review of pathogenesis and oncologic risk. *Ther Adv Urol.* 2015;7(6):378-87.
19. Wang G, Zhao D, Spring DJ, DePinho RA. Genetics and biology of prostate cancer. *Genes Dev.* 2018;32(17-18):1105-40.
20. van Leenders GJLH, Schalken JA. Epithelial cell differentiation in the human prostate epithelium: Implications for the pathogenesis and therapy of prostate cancer. *Critical Reviews in Oncology/ Hematology.* 2003;46:3-10.
21. Kato M, Sasaki T, Inoue T. Current experimental human tissue-derived models for prostate cancer research. *Int J Urol.* 2021;28(2):150-62.
22. Crowell PD, Fox JJ, Hashimoto T, Diaz JA, Navarro HI, Henry GH, Feldmar BA, Lowe MG, Garcia AJ, Wu YE, Sajed DP, Strand DW, Goldstein AS. Expansion of Luminal Progenitor Cells in the Aging Mouse and Human Prostate. *Cell Rep.* 2019;28(6):1499-510 e6.
23. Humphrey PA. Histological variants of prostatic carcinoma and their significance. *Histopathology.* 2012;60(1):59-74.
24. Park JW, Lee JK, Phillips JW, Huang P, Cheng D, Huang J, Witte ON. Prostate epithelial cell of origin determines cancer differentiation state in an organoid transformation assay. *Proc Natl Acad Sci U S A.* 2016;113(16):4482-7.
25. Wang ZA, Mitrofanova A, Bergren SK, Abate-Shen C, Cardiff RD, Califano A, Shen MM. Lineage analysis of basal epithelial cells reveals their unexpected plasticity and supports a cell-of-origin model for prostate cancer heterogeneity. *Nat Cell Biol.* 2013;15(3):274-83.
26. Wang X, Kruihof-de Julio M, Economides KD, Walker D, Yu H, Halili MV, Hu YP, Price SM, Abate-Shen C, Shen MM. A luminal epithelial stem cell that is a cell of origin for prostate cancer. *Nature.* 2009;461(7263):495-500.
27. Chua CW, Shibata M, Lei M, Toivanen R, Barlow LJ, Bergren SK, Badani KK, McKiernan JM, Benson MC, Hibshoosh H, Shen MM. Single luminal epithelial progenitors can generate prostate organoids in culture. *Nat Cell Biol.* 2014;16(10):951-61, 1-4.
28. Wang ZA, Toivanen R, Bergren SK, Chambon P, Shen MM. Luminal cells are favored as the cell of origin for prostate cancer. *Cell Rep.* 2014;8(5):1339-46.
29. Hubbard GK, Mutton LN, Khalili M, McMullin RP, Hicks JL, Bianchi-Frias D, Horn LA, Kulac I, Moubarek MS, Nelson PS, Yegnasubramanian S, De Marzo AM, Bieberich CJ. Combined MYC Activation and Pten Loss Are Sufficient to Create Genomic Instability and Lethal Metastatic Prostate Cancer. *Cancer Res.* 2016;76(2):283-92.
30. Gurel B, Ali TZ, Montgomery EA, Begum S, Hicks J, Goggins M, Eberhart CG, Clark DP, Bieberich CJ, Epstein JI, De Marzo AM. NKX3.1 as a marker of prostatic origin in metastatic tumors. *Am J Surg Pathol.* 2010;34(8):1097-105.

References

31. Tomlins SA, Laxman B, Varambally S, Cao X, Yu J, Helgeson BE, Cao Q, Prensner JR, Rubin MA, Shah RB, Mehra R, Chinnaiyan AM. Role of the TMPRSS2-ERG gene fusion in prostate cancer. *Neoplasia*. 2008;10(2):177-88.
32. Shoag J, Liu D, Blattner M, Sboner A, Park K, Deonarine L, Robinson BD, Mosquera JM, Chen Y, Rubin MA, Barbieri CE. SPOP mutation drives prostate neoplasia without stabilizing oncogenic transcription factor ERG. *J Clin Invest*. 2018;128(1):381-6.
33. Saranyutanon S, Deshmukh SK, Dasgupta S, Pai S, Singh S, Singh AP. Cellular and Molecular Progression of Prostate Cancer: Models for Basic and Preclinical Research. *Cancers (Basel)*. 2020;12(9).
34. Graham MK, Meeker A. Telomeres and telomerase in prostate cancer development and therapy. *Nat Rev Urol*. 2017;14(10):607-19.
35. Gerhardt J, Montani M, Wild P, Beer M, Huber F, Hermanns T, Muntener M, Kristiansen G. FOXA1 promotes tumor progression in prostate cancer and represents a novel hallmark of castration-resistant prostate cancer. *Am J Pathol*. 2012;180(2):848-61.
36. Annala M, Taavitsainen S, Vandekerckhove G, Bacon JW, Beja K, Chi KN, Nykter M, Wyatt AW. Frequent mutation of the FOXA1 untranslated region in prostate cancer. *Commun Biol*. 2018;1:122.
37. Jamaspishvili T, Berman DM, Ross AE, Scher HI, De Marzo AM, Squire JA, Lotan TL. Clinical implications of PTEN loss in prostate cancer. *Nat Rev Urol*. 2018;15(4):222-34.
38. Chen WS, Alshalalfa M, Zhao SG, Liu Y, Mahal BA, Quigley DA, Wei T, Davicioni E, Rebbeck TR, Kantoff PW, Maher CA, Knudsen KE, Small EJ, Nguyen PL, Feng FY. Novel RB1-Loss Transcriptomic Signature Is Associated with Poor Clinical Outcomes across Cancer Types. *Clin Cancer Res*. 2019;25(14):4290-9.
39. Wang S, Gao J, Lei Q, Rozengurt N, Pritchard C, Jiao J, Thomas GV, Li G, Roy-Burman P, PNelson PS, Liu X, Wu H. Prostate-specific deletion of the murine Pten tumor suppressor gene leads to metastatic prostate cancer. *Cancer Cell*. 2003;4(3):209-21.
40. Deplus R, Delliaux C, Marchand N, Flourens A, Vanpouille N, Leroy X, de Launoit Y, Duterque-Coquillaud M. TMPRSS2-ERG fusion promotes prostate cancer metastases in bone. *Oncotarget*. 2017;8(7):11827-40.
41. Ganaie AA, Beigh FH, Astone M, Ferrari MG, Maqbool R, Umbreen S, Parray AS, Siddique HR, Hussain T, Murugan P, Morrissey C, Koochekpour S, Deng Y, Konety BR, Hoepfner LH, Saleem M. BMI1 Drives Metastasis of Prostate Cancer in Caucasian and African-American Men and Is A Potential Therapeutic Target: Hypothesis Tested in Race-specific Models. *Clin Cancer Res*. 2018;24(24):6421-32.
42. Srivastava SK, Bhardwaj A, Singh S, Arora S, McClellan S, Grizzle WE, Reed E, Singh AP. Myb overexpression overrides androgen depletion-induced cell cycle arrest and apoptosis in prostate cancer cells, and confers aggressive malignant traits: potential role in castration resistance. *Carcinogenesis*. 2012;33(6):1149-57.
43. Augello MA, Den RB, Knudsen KE. AR function in promoting metastatic prostate cancer. *Cancer Metastasis Rev*. 2014;33(2-3):399-411.

References

44. Wu X, Scott H, Carlsson SV, Sjoberg DD, Cerundolo L, Lilja H, Prevo R, Rieunier G, Macaulay V, Higgins GS, Verrill CL, Lamb AD, Cunliffe VT, Bountra C, Hamdy FC, Bryant RJ. Increased EZH2 expression in prostate cancer is associated with metastatic recurrence following external beam radiotherapy. *Prostate*. 2019;79(10):1079-89.
45. Lakshmiathan V, Zou L, Kim JI, Michal A, Nie Z, Messias NC, Benovic JL, Daaka Y. Identification of betaArrestin2 as a corepressor of androgen receptor signaling in prostate cancer. *Proc Natl Acad Sci U S A*. 2009;106(23):9379-84.
46. Stambolic V, Suzuki A, de la Pompa JL, Brothers GM, Mirtsos C, Sasaki T, Ruland J, Penninger JM, Siderovski DP, Mak TW. Negative Regulation of PKB/Akt-Dependent Cell Survival by the Tumor Suppressor PTEN. *Cell* 1998;95(1):29-39.
47. He W, Sciavolino P, Wing J, Augustus M, Hudson P, Meissner P, Curtis R, Shell B, Bostwick D, Tindall D, Gelmann E, Abate-Shen C, Carter K. A novel human prostate-specific, androgen-regulated homeobox gene (NKX3.1) that maps to 8p21, a region frequently deleted in prostate cancer. *Genomics*. 1997;43(1):69-77.
48. Yang CC, Chung A, Ku CY, Brill LM, Williams R, Wolf DA. Systems analysis of the prostate tumor suppressor NKX3.1 supports roles in DNA repair and luminal cell differentiation. *F1000Res*. 2014;3:115.
49. Qiu X, Boufaied N, Hallal T, Feit A, de Polo A, Luoma AM, Alahmadi W, Larocque J, Zadra G, Xie Y, Gu S, Tang Q, Zhang Y, Syamala S, Seo JH, Bell C, O'Connor E, Liu Y, Schaeffer EM, Jeffrey Karnes R, Weinmann S, Davicioni E, Morrissey C, Cejas P, Ellis L, Loda M, Wucherpfennig KW, Pomerantz MM, Spratt DE, Corey E, Freedman ML, Shirley Liu X, Brown M, Long HW, Labbe DP. MYC drives aggressive prostate cancer by disrupting transcriptional pause release at androgen receptor targets. *Nat Commun*. 2022;13(1):2559.
50. Burkhardt DL, Sage J. Cellular mechanisms of tumour suppression by the retinoblastoma gene. *Nat Rev Cancer*. 2008;8(9):671-82.
51. Chen HZ, Tsai SY, Leone G. Emerging roles of E2Fs in cancer: an exit from cell cycle control. *Nat Rev Cancer*. 2009;9(11):785-97.
52. Macleod KF. The RB tumor suppressor: a gatekeeper to hormone independence in prostate cancer? *J Clin Invest*. 2010;120(12):4179-82.
53. Neben K, Schnittger S, Brors B, Tews B, Kokocinski F, Haferlach T, Muller J, Hahn M, Hiddemann W, Eils R, Lichter P, Schoch C. Distinct gene expression patterns associated with FLT3- and NRAS-activating mutations in acute myeloid leukemia with normal karyotype. *Oncogene*. 2005;24(9):1580-8.
54. Lin L, Miller CT, Contreras JI, Prescott MS, Dagenais SL, Wu R, Yee J, Orringer MB, Misek DE, Hanash SM, Glover TW, Beer DG. The hepatocyte nuclear factor 3 α gene, HNF3 α (FOXA1), on chromosome band 14q13 is amplified and overexpressed in esophageal and lung adenocarcinomas. *Cancer Research*. 2002;62(18):5273-9.

References

55. Nucera C, Eeckhoute J, Finn S, Carroll JS, Ligon AH, Priolo C, Fadda G, Toner M, Sheils O, Attard M, Pontecorvi A, Nose V, Loda M, Brown M. FOXA1 is a potential oncogene in anaplastic thyroid carcinoma. *Clin Cancer Res.* 2009;15(11):3680-9.
56. Hu X, Stern HM, Ge L, O'Brien C, Haydu L, Honchell CD, Haverty PM, Peters BA, Wu TD, Amler LC, Chant J, Stokoe D, Lackner MR, Cavet G. Genetic alterations and oncogenic pathways associated with breast cancer subtypes. *Mol Cancer Res.* 2009;7(4):511-22.
57. Robbins CM, Tembe WA, Baker A, Sinari S, Moses TY, Beckstrom-Sternberg S, Beckstrom-Sternberg J, Barrett M, Long J, Chinnaiyan A, Lowey J, Suh E, Pearson JV, Craig DW, Agus DB, Pienta KJ, Carpten JD. Copy number and targeted mutational analysis reveals novel somatic events in metastatic prostate tumors. *Genome Res.* 2011;21(1):47-55.
58. Sahu B, Laakso M, Ovaska K, Mirtti T, Lundin J, Rannikko A, Sankila A, Turunen JP, Lundin M, Konsti J, Vesterinen T, Nordling S, Kallioniemi O, Hautaniemi S, Janne OA. Dual role of FoxA1 in androgen receptor binding to chromatin, androgen signalling and prostate cancer. *EMBO J.* 2011;30(19):3962-76.
59. Jin HJ, Zhao JC, Ogden I, Bergan RC, Yu J. Androgen receptor-independent function of FoxA1 in prostate cancer metastasis. *Cancer Res.* 2013;73(12):3725-36.
60. Wang D, Garcia-Bassets I, Benner C, Li W, Su X, Zhou Y, Qiu J, Liu W, Kaikkonen MU, Ohgi KA, Glass CK, Rosenfeld MG, Fu XD. Reprogramming transcription by distinct classes of enhancers functionally defined by eRNA. *Nature.* 2011;474(7351):390-4.
61. Razavipour SF, Harikumar KB, Slingerland JM. p27 as a Transcriptional Regulator: New Roles in Development and Cancer. *Cancer Res.* 2020;80(17):3451-8.
62. Schrecengost R, Knudsen KE. Molecular pathogenesis and progression of prostate cancer. *Semin Oncol.* 2013;40(3):244-58.
63. Kader A, Brangsch J, Kaufmann JO, Zhao J, Mangarova DB, Moeckel J, Adams LC, Sack I, Taupitz M, Hamm B, Makowski MR. Molecular MR Imaging of Prostate Cancer. *Biomedicines.* 2020;9(1).
64. Tan HL, Haffner MC, Esopi DM, Vaghasia AM, Giannico GA, Ross HM, Ghosh S, Hicks JL, Zheng Q, Sangoi AR, Yegnasubramanian S, Osunkoya AO, De Marzo AM, Epstein JI, Lotan TL. Prostate adenocarcinomas aberrantly expressing p63 are molecularly distinct from usual-type prostatic adenocarcinomas. *Mod Pathol.* 2015;28(3):446-56.
65. Li W, Qian L, Lin J, Huang G, Hao N, Wei X, Wang W, Liang J. CD44 regulates prostate cancer proliferation, invasion and migration via PDK1 and PFKFB4. *Oncotarget.* 2017;8(39):65143-51.
66. Martignano F, Gurioli G, Salvi S, Calistri D, Costantini M, Gunelli R, De Giorgi U, Foca F, Casadio V. GSTP1 Methylation and Protein Expression in Prostate Cancer: Diagnostic Implications. *Dis Markers.* 2016;2016:4358292.
67. Yousef GM, Diamandis EP. The new human tissue Kallikrein Gene Family: Structure, function, and association to disease. *Endocrine reviews.* 2001;22(2):184-204.
68. Balk SP, Ko YJ, Bubley GJ. Biology of prostate-specific antigen. *J Clin Oncol.* 2003;21(2):383-91.

References

69. Ghosh A, Wang X, Klein E, Heston WDW. Novel Role of Prostate-Specific Membrane Antigen in Suppressing Prostate Cancer Invasiveness. *cancer reserach*. 2015;65(3):727-31.
70. Pu F, Salarian M, Xue S, Qiao J, Feng J, Tan S, Patel A, Li X, Mamouni K, Hekmatyar K, Zou J, Wu D, Yang JJ. Prostate-specific membrane antigen targeted protein contrast agents for molecular imaging of prostate cancer by MRI. *Nanoscale*. 2016;8(25):12668-82.
71. Zhao J, Hamm B, Brenner W, Makowski MR. Lesion-to-background ratio threshold value of SUVmax of simultaneous [(68)Ga]Ga-PSMA-11 PET/MRI imaging in patients with prostate cancer. *Insights Imaging*. 2020;11(1):137.
72. Minner S, Wittmer C, Graefen M, Salomon G, Steuber T, Haese A, Huland H, Bokemeyer C, Yekebas E, Dierlamm J, Balabanov S, Kilic E, Wilczak W, Simon R, Sauter G, Schlomm T. High level PSMA expression is associated with early PSA recurrence in surgically treated prostate cancer. *Prostate*. 2011;71(3):281-8.
73. Perner S, Hofer MD, Kim R, Shah RB, Li H, Moller P, Hautmann RE, Gschwend JE, Kuefer R, Rubin MA. Prostate-specific membrane antigen expression as a predictor of prostate cancer progression. *Hum Pathol*. 2007;38(5):696-701.
74. Ross JS, Sheehan CE, Fisher HAG, Kaufman RPJ, Kaur P, Gray K, Webb I, Gray GS, Mosher R, Kallakury BVS. Correlation of Primary Tumor Prostate-Specific Membrane Antigen Expression with Disease Recurrence in Prostate Cancer. *Clinical Cancer Research*. 2003;9:6357-62.
75. Arap W, Pasqualini R, Costello JF. Prostate Cancer Progression and the Epigenome. *New England Journal of Medicine*. 2020;383(23):2287-90.
76. Song Z, Huang Y, Zhao Y, Ruan H, Yang H, Cao Q, Liu D, Zhang X, Chen K. The Identification of Potential Biomarkers and Biological Pathways in Prostate Cancer. *J Cancer*. 2019;10(6):1398-408.
77. Saha AK, Contreras-Galindo R, Niknafs YS, Iyer M, Qin T, Padmanabhan K, Siddiqui J, Palande M, Wang C, Qian B, Ward E, Tang T, Tomlins SA, Gitlin SD, Sartor MA, Omenn GS, Chinnaiyan AM, Markovitz DM. The role of the histone H3 variant CENPA in prostate cancer. *J Biol Chem*. 2020;295(25):8537-49.
78. Sheng Y, Wang W, Hong B, Jiang X, Sun R, Yan Q, Zhang S, Lu M, Wang S, Zhang Z, Lin W, Li Y. Upregulation of KIF20A correlates with poor prognosis in gastric cancer. *Cancer Manag Res*. 2018;10:6205-16.
79. Zhang Z, Chai C, Shen T, Li X, Ji J, Li C, Shang Z, Niu Y. Aberrant KIF20A Expression Is Associated with Adverse Clinical Outcome and Promotes Tumor Progression in Prostate Cancer. *Dis Markers*. 2019;2019:4782730.
80. Zou JX, Duan Z, Wang J, Sokolov A, Xu J, Chen CZ, Li JJ, Chen HW. Kinesin family deregulation coordinated by bromodomain protein ANCCA and histone methyltransferase MLL for breast cancer cell growth, survival, and tamoxifen resistance. *Mol Cancer Res*. 2014;12(4):539-49.
81. Wan S, He Y, Zhang B, Yang Z, Du FM, Zhang CP, Fu YQ, Mi J. Overexpression of CDCA8 Predicts Poor Prognosis and Promotes Tumor Cell Growth in Prostate Cancer. *Front Oncol*. 2022;12:784183.

References

82. Abad MA, Ruppert JG, Buzuk L, Wear M, Zou J, Webb KM, Kelly DA, Voigt P, Rappsilber J, Earnshaw WC, Jeyaprakash AA. Borealin-nucleosome interaction secures chromosome association of the chromosomal passenger complex. *J Cell Biol.* 2019;218(12):3912-25.
83. Niu YN, Xia SJ. Stroma-epithelium crosstalk in prostate cancer. *Asian J Androl.* 2009;11(1):28-35.
84. Bhowmick NA, Moses HL. Tumor-stroma interactions. *Curr Opin Genet Dev.* 2005;15(1):97-101.
85. Bhowmick NA, Neilson EG, Moses HL. Stromal fibroblasts in cancer initiation and progression. *Nature.* 2004;432(7015):332-7.
86. Alkasalias T, Moyano-Galceran L, Arsenian-Henriksson M, Lehti K. Fibroblasts in the Tumor Microenvironment: Shield or Spear? *Int J Mol Sci.* 2018;19(5).
87. Bonollo F, Thalmann GN, Kruihof-de Julio M, Karkampouna S. The Role of Cancer-Associated Fibroblasts in Prostate Cancer Tumorigenesis. *Cancers (Basel).* 2020;12(7).
88. Lo CH, Lynch CC. Multifaceted Roles for Macrophages in Prostate Cancer Skeletal Metastasis. *Front Endocrinol (Lausanne).* 2018;9:247.
89. Lanciotti M, Masieri L, Raspollini MR, Minervini A, Mari A, Comito G, Giannoni E, Carini M, Chiarugi P, Serni S. The role of M1 and M2 macrophages in prostate cancer in relation to extracapsular tumor extension and biochemical recurrence after radical prostatectomy. *Biomed Res Int.* 2014;2014:486798.
90. Erlandsson A, Carlsson J, Lundholm M, Falt A, Andersson SO, Andren O, Davidsson S. M2 macrophages and regulatory T cells in lethal prostate cancer. *Prostate.* 2019;79(4):363-9.
91. Cihan YB, Arslan A, Ergul MA. Subtypes of white blood cells in patients with prostate cancer or benign prostatic hyperplasia and healthy individuals. *Asian Pac J Cancer Prev.* 2013;14(8):4779-83.
92. Norrby K. Mast cells and angiogenesis. *APMIS.* 2002;110:355-71.
93. Xu W, Qian J, Zeng F, Li S, Guo W, Chen L, Li G, Zhang Z, Wang QJ, Deng F. Protein kinase Ds promote tumor angiogenesis through mast cell recruitment and expression of angiogenic factors in prostate cancer microenvironment. *J Exp Clin Cancer Res.* 2019;38(1):114.
94. Johansson A, Rudolfsson S, Hammarsten P, Halin S, Pietras K, Jones J, Stattin P, Egevad L, Granfors T, Wikstrom P, Bergh A. Mast cells are novel independent prognostic markers in prostate cancer and represent a target for therapy. *Am J Pathol.* 2010;177(2):1031-41.
95. Ma Z, Yue L, Xu Z, Zeng S, Ma Y, Li Z, Li W, Wang D. The effect of mast cells on the biological characteristics of prostate cancer cells. *Cent Eur J Immunol.* 2018;43(1):1-8.
96. Zhao R, Bei X, Yang B, Wang X, Jiang C, Shi F, Wang X, Zhu Y, Jing Y, Han B, Xia S, Jiang Q. Endothelial cells promote metastasis of prostate cancer by enhancing autophagy. *J Exp Clin Cancer Res.* 2018;37(1):221.
97. Ribeiro AL, Okamoto OK. Combined effects of pericytes in the tumor microenvironment. *Stem Cells Int.* 2015;2015:868475.
98. Kruslin B, Ulamec M, Tomas D. Prostate cancer stroma: an important factor in cancer growth and progression. *Bosn J Basic Med Sci.* 2015;15(2):1-8.

References

99. Tuxhorn J, Ayala G, Rowley DR. Reactive Stroma in Prostate Cancer Progression. *The Journal of Urology*. 2001;166:2472-83.
100. Bair EL, Chen ML, McDaniel K, Sekiguchi K, Cress AE, Nagle RB, Bowden GT. Membrane type 1 matrix metalloprotease cleaves laminin-10 and promotes prostate cancer cell migration. *Neoplasia*. 2005;7(4):380-9.
101. Vollmer G. Biologic and oncologic implications of tenascin-C/hexabrachion proteins. *Hematology*. 1997;25(187-210).
102. Tomas D, Ulamec M, Hudolin T, Bulimbasic S, Belicza M, Kruslin B. Myofibroblastic stromal reaction and expression of tenascin-C and laminin in prostate adenocarcinoma. *Prostate Cancer Prostatic Dis*. 2006;9(4):414-9.
103. Calderon LGR, Kobayashi PE, Vasconcelos RO, Fonseca-Alves CE, Laufer-Amorim R. Characterization of Collagen Fibers (I, III, IV) and Elastin of Normal and Neoplastic Canine Prostatic Tissues. *Vet Sci*. 2019;6(1).
104. Scandolera A, Odoul L, Salesse S, Guillot A, Blaise S, Kawecki C, Maurice P, El Btaouri H, Romier-Crouzet B, Martiny L, Debelle L, Duca L. The Elastin Receptor Complex: A Unique Matricellular Receptor with High Anti-tumoral Potential. *Front Pharmacol*. 2016;7:32.
105. Lapis K, Tímár J. Role of elastin–matrix interactions in tumor progression. *Seminars in Cancer Biology*. 2002;12(3):209-17.
106. Wang TH, Hsia SM, Shieh TM. Lysyl Oxidase and the Tumor Microenvironment. *Int J Mol Sci*. 2016;18(1).
107. Siegel RC, Pinnell SR, GMartin GR. Cross-Linking of Collagen and Elastin. Properties of Lysyl Oxidase. *J Mol Biol*. 1970;38:245.
108. Quail DF, Joyce JA. Microenvironmental regulation of tumor progression and metastasis. *Nat Med*. 2013;19(11):1423-37.
109. Ost P, Bossi A, Decaestecker K, De Meerleer G, Giannarini G, Karnes RJ, Roach M, 3rd, Briganti A. Metastasis-directed therapy of regional and distant recurrences after curative treatment of prostate cancer: a systematic review of the literature. *Eur Urol*. 2015;67(5):852-63.
110. Forrest MS, Edwards SM, Houlston R, Kote-Jarai Z, Key T, Allen N, Knowles MA, Turner F, Ardern-Jones A, Murkin A, Williams S, Oram R, Bishop DT, Eeles RA, collaborators C-UBUpcs. Association between hormonal genetic polymorphisms and early-onset prostate cancer. *Prostate Cancer Prostatic Dis*. 2005;8(1):95-102.
111. Sharma S, Zapatero-Rodriguez J, O'Kennedy R. Prostate cancer diagnostics: Clinical challenges and the ongoing need for disruptive and effective diagnostic tools. *Biotechnol Adv*. 2017;35(2):135-49.
112. Wibmer AG, Burger IA, Sala E, Hricak H, Weber WA, Alberto Vargas H. Molecular Imaging of Prostate Cancer. *Radiographics*. 2015;36(1):142-59.
113. Vaghefi H, Magi-Galluzzi C, Klein EA. Local recurrence of prostate cancer in rectal submucosa after transrectal needle biopsy and radical prostatectomy. *Urology*. 2005;66(4):881.

References

114. Lane Z, Epstein JI, Ayub S, Netto GJ. Prostatic adenocarcinoma in colorectal biopsy: clinical and pathologic features. *Hum Pathol.* 2008;39(4):543-9.
115. Ohori M, Wheeler T, Scardino PT. The new american joint committee on cancer and international union against cancer tnm.pdf>. *Cancer* 1994;74(1):104-14.
116. Barentsz JO, Richenberg J, Clements R, Choyke P, Verma S, Villeirs G, Rouviere O, Logager V, Futterer JJ, European Society of Urogenital R. ESUR prostate MR guidelines 2012. *Eur Radiol.* 2012;22(4):746-57.
117. Weinreb JC, Barentsz JO, Choyke PL, Cornud F, Haider MA, Macura KJ, Margolis D, Schnall MD, Shtern F, Tempny CM, Thoeny HC, Verma S. PI-RADS Prostate Imaging - Reporting and Data System: 2015, Version 2. *Eur Urol.* 2016;69(1):16-40.
118. Becker AS, Cornelius A, Reiner CS, Stocker D, Ulbrich EJ, Barth BK, Mortezaei A, Eberli D, Donati OF. Direct comparison of PI-RADS version 2 and version 1 regarding interreader agreement and diagnostic accuracy for the detection of clinically significant prostate cancer. *Eur J Radiol.* 2017;94:58-63.
119. Kim CH, Bhattacharjee S, Prakash D, Kang S, Cho NH, Kim HC, Choi HK. Artificial Intelligence Techniques for Prostate Cancer Detection through Dual-Channel Tissue Feature Engineering. *Cancers (Basel).* 2021;13(7).
120. Hoffman RM. Screening for Prostate Cancer. *New England Journal of Medicine.* 2011;365(21):2013-9.
121. Ilic D, Djulbegovic M, Jung JH, Hwang EC, Zhou Q, Cleves A, Agoritsas T, Dahm P. Prostate cancer screening with prostate-specific antigen (PSA) test: a systematic review and meta-analysis. *BMJ.* 2018;362:k3519.
122. Simoes GF, Sakuramoto P, Santos CBd, Furlan NKC, Augusto TM. An Overview on Prostate Pathophysiology: New Insights into Prostate Cancer Clinical Diagnosis. *Pathophysiology - Altered Physiological States*2018.
123. Kader A, Brangsch J, Reimann C, Kaufmann JO, Mangarova DB, Moeckel J, Adams LC, Zhao J, Saatz J, Traub H, Buchholz R, Karst U, Hamm B, Makowski MR. Visualization and Quantification of the Extracellular Matrix in Prostate Cancer Using an Elastin Specific Molecular Probe. *Biology (Basel).* 2021;10(11).
124. Loeb S, Catalona WJ. The Prostate Health Index: a new test for the detection of prostate cancer. *Ther Adv Urol.* 2014;6(2):74-7.
125. Punnen S, Pavan N, Parekh D. Finding the Wolf in Sheep's Clothing: The 4Kscore Is a Novel Blood Test That Can Accurately Identify the Risk of Aggressive Prostate Cancer. *Reviews in Urology.* 2015;17(1):3-13.
126. McKiernan J, Donovan MJ, O'Neill V, Bentink S, Noerholm M, Belzer S, Skog J, Kattan MW, Partin A, Andriole G, Brown G, Wei JT, Thompson IM, Jr., Carroll P. A Novel Urine Exosome Gene Expression Assay to Predict High-grade Prostate Cancer at Initial Biopsy. *JAMA Oncol.* 2016;2(7):882-9.
127. Wei JT, Feng Z, Partin AW, Brown E, Thompson I, Sokoll L, Chan DW, Lotan Y, Kibel AS, Busby JE, Bidair M, Lin DW, Taneja SS, Viterbo R, Joon AY, Dahlgren J, Kagan J, Srivastava S, Sanda MG. Can urinary PCA3 supplement PSA in the early detection of prostate cancer? *J Clin Oncol.* 2014;32(36):4066-72.

References

128. Gittelman MC, Hertzman B, Bailen J, Williams T, Koziol I, Henderson RJ, Efros M, Bidair M, Ward JF. PCA3 molecular urine test as a predictor of repeat prostate biopsy outcome in men with previous negative biopsies: a prospective multicenter clinical study. *J Urol.* 2013;190(1):64-9.
129. Dijkstra S, Birker IL, Smit FP, Leyten GH, de Reijke TM, van Oort IM, Mulders PF, Jannink SA, Schalken JA. Prostate cancer biomarker profiles in urinary sediments and exosomes. *J Urol.* 2014;191(4):1132-8.
130. Leyten GH, Hessels D, Jannink SA, Smit FP, de Jong H, Cornel EB, de Reijke TM, Vergunst H, Kil P, Knipscheer BC, van Oort IM, Mulders PF, Hulsbergen-van de Kaa CA, Schalken JA. Prospective multicentre evaluation of PCA3 and TMPRSS2-ERG gene fusions as diagnostic and prognostic urinary biomarkers for prostate cancer. *Eur Urol.* 2014;65(3):534-42.
131. Cheng XH, Black M, Ustiyan V, Le T, Fulford L, Sridharan A, Medvedovic M, Kalinichenko VV, Whitsett JA, Kalin TV. SPDEF inhibits prostate carcinogenesis by disrupting a positive feedback loop in regulation of the Foxm1 oncogene. *PLoS Genet.* 2014;10(9):e1004656.
132. Haller AC, Tan W, Payne-Ondracek R, Underwood W, Tian L, Morrison C, Li F. High SPDEF may identify patients who will have a prolonged response to androgen deprivation therapy. *Prostate.* 2014;74(5):509-19.
133. Oettgen P, Finger E, Sun Z, Akbarali Y, Thamrongsak U, Boltax J, Grall F, Dube A, Weiss A, Brown L, Quinn G, Kas K, Endress G, Kunsch C, Libermann TA. PDEF, a novel prostate epithelium-specific ets transcription factor, interacts with the androgen receptor and activates prostate-specific antigen gene expression. *J Biol Chem.* 2000;275(2):1216-25.
134. St John J, Powell K, Conley-Lacomb MK, Chinni SR. TMPRSS2-ERG Fusion Gene Expression in Prostate Tumor Cells and Its Clinical and Biological Significance in Prostate Cancer Progression. *J Cancer Sci Ther.* 2012;4(4):94-101.
135. Hagen RM, Adamo P, Karamat S, Oxley J, Aning JJ, Gillatt D, Persad R, Lodomery MR, Rhodes A. Quantitative analysis of ERG expression and its splice isoforms in formalin-fixed, paraffin-embedded prostate cancer samples: association with seminal vesicle invasion and biochemical recurrence. *Am J Clin Pathol.* 2014;142(4):533-40.
136. Svensson MAP, Sven; Ohlson, Anna-Lena; Day, John R.; Groskopf, Jack; Kirsten, Robert; Sollie, Thomas; Helenius, Gisela; Andersson, Swen-Olof; Demichelis, Francesca; Andrén, Ove; Rubin, Mark A. . A Comparative Study of ERG Status Assessment on DNA, mRNA, and Protein Levels Using Unique Samples from a Swedish Biopsy Cohort. *Applied Immunohistochemistry & Molecular Morphology.* 2014;22(2):136-41.
137. He J, Schepmoes AA, Shi T, Wu C, Fillmore TL, Gao Y, Smith RD, Qian WJ, Rodland KD, Liu T, Camp DG, 2nd, Rastogi A, Tan SH, Yan W, Mohamed AA, Huang W, Banerjee S, Kagan J, Srivastava S, McLeod DG, Srivastava S, Petrovics G, Dobi A, Srinivasan A. Analytical platform evaluation for quantification of ERG in prostate cancer using protein and mRNA detection methods. *J Transl Med.* 2015;13:54.
138. AmericanCancerSociety. Treating Prostate Cancer 2022 [Available from: <https://www.cancer.org/cancer/prostate-cancer/treating.html>].

References

139. Shirai T, Takahashi S, Cui L, Futakuchi M, Kato K, Tamano S, Imaida K. Experimental prostate carcinogenesis — rodent models. *Mutation Research*. 2000;462:219-26.
140. Lamb DJ, Zhang L. Challenges in Prostate Cancer Research: Animal Models for Nutritional Studies of Chemoprevention and Disease Progression. *The Journal of Nutrition*. 2005;135(12):3009S-15S.
141. Pollard M. The Lobund-Wistar Rat Model of Prostate Cancer. *Journal of Cellular Biochemistry*. 1992;16:84-8.
142. Ittmann M, Huang J, Radaelli E, Martin P, Signoretti S, Sullivan R, Simons BW, Ward JM, Robinson BD, Chu GC, Loda M, Thomas G, Borowsky A, Cardiff RD. Animal models of human prostate cancer: the consensus report of the New York meeting of the Mouse Models of Human Cancers Consortium Prostate Pathology Committee. *Cancer Res*. 2013;73(9):2718-36.
143. Flanagan SP. 'Nude', a new hairless gene with pleiotropic effects in the mouse. *Genet Res*. 1966;8(3):295-309.
144. van Weerden WM, Romijn JC. Use of Nude Mouse Xenograft Models in Prostate Cancer Research. *The Prostate*. 2000;43:263-71.
145. Fidler IJ. Rationale and methods for the use of nude mice to study the biology and therapy of human cancer metastasis. *Cancer and Metastasis Reviews*. 1986;5:29-49.
146. Stephenson RA, Dinney CPN, Gohji K, Ordonez NG, Killion JJ, Fidler IJ. Metastatic Model for Human Prostate Cancer Using Orthotopic Implantation in Nude Mice. *Journal of the National Cancer Institute*. 1992;84(12):951-7.
147. Bastide C, Bagnis C, Mannoni P, Hassoun J, Bladou F. A Nod Scid mouse model to study human prostate cancer. *Prostate Cancer Prostatic Dis*. 2002;5(4):311-5.
148. Zong Y, Xin L, Goldstein AS, Lawson DA, Teitell MA, Witte ON. ETS family transcription factors collaborate with alternative signaling pathways to induce carcinoma from adult murine prostate cells. *Proc Natl Acad Sci U S A*. 2009;106(30):12465-70.
149. Goldstein AS, Huang J, Guo C, Garraway IP, Witte ON. Identification of a cell of origin for human prostate cancer. *Science*. 2010;329(5991):568-71.
150. Ammirante M, Luo JL, Grivennikov S, Nedospasov S, Karin M. B-cell-derived lymphotoxin promotes castration-resistant prostate cancer. *Nature*. 2010;464(7286):302-5.
151. Pepe P, Panella P, D'Arrigo L, Savoca F, Pennisi M, Aragona F. Should men with serum prostate-specific antigen ≤ 4 ng/ml and normal digital rectal examination undergo a prostate biopsy? A literature review. *Oncology*. 2006;70(2):81-9.
152. Fernandes MC, Yildirim O, Woo S, Vargas HA, Hricak H. The role of MRI in prostate cancer: current and future directions. *MAGMA*. 2022.
153. Glazer DI, Davenport MS, Khalatbari S, Cohan RH, Ellis JH, Caoili EM, Stein EB, Childress JC, Masch WR, Brown JM, Mollard BJ, Montgomery JS, Palapattu GS, Francis IR. Mass-like peripheral zone enhancement on CT is predictive of higher-grade (Gleason 4 + 3 and higher) prostate cancer. *Abdom Imaging*. 2015;40(3):560-70.

References

154. Grover VP, Tognarelli JM, Crossey MM, Cox IJ, Taylor-Robinson SD, McPhail MJ. Magnetic Resonance Imaging: Principles and Techniques: Lessons for Clinicians. *J Clin Exp Hepatol*. 2015;5(3):246-55.
155. Bloch BN, Lenkinski RE, Rofsky NM. The Role of Magnetic Resonance Imaging (MRI) in Prostate Cancer Imaging and Staging at 1.5 and 3 Tesla : The Beth Israel Deaconess Medical Center (BIDMC) Approach. *Cancer Biomark*. 2008;4(4-5):251–62.
156. de Bazelaire C, Calmon R, Thomassin I, Brunon C, Hamy AS, Fournier L, Balvay D, Espie M, Siauve N, Clement O, de Kerviler E, Cuenod CA. Accuracy of perfusion MRI with high spatial but low temporal resolution to assess invasive breast cancer response to neoadjuvant chemotherapy: a retrospective study. *BMC Cancer*. 2011;11:361.
157. Pinker K, Grabner G, Bogner W, Gruber S, Szomolanyi P, Trattng S, Heinz-Peer G, Weber M, Fitzal F, Pluschnig U, Rudas M, Helbich T. A Combined High Temporal and High Spatial Resolution 3 Tesla MR Imaging Protocol for the Assessment of Breast Lesions. *Invest Radiol*. 2009;44:553-8.
158. Li B, Du Y, Yang H, Huang Y, Meng J, Xiao D. Magnetic resonance imaging for prostate cancer clinical application. *Chin J Cancer Res*. 2013;25(2):240-9.
159. Hricak H, Choyke PL, Eberhardt SC, Leibel SA, Scardino PT. Imaging Prostate Cancer: A Multidisciplinary Perspective. *Radiology*. 2007;243(1):28-53.
160. Vanhoutte L, Gallez B, Feron O, Balligand JL, Esfahani H, d'Hoore W, Moniotte S. Variability of Mouse Left Ventricular Function Assessment by 11.7 Tesla MRI. *J Cardiovasc Transl Res*. 2015;8(6):362-71.
161. Cabello MAR, Rubio SM, Sanz AM, Miguelanez JLS, Alba DV, Gonzalez CA, Sancho AP. Comparative study between 1.5 and 3 Tesla multiparametric MRI systems using the PIRADS version 2 classification in the diagnosis of prostate cancer. *Arch Esp Urol*. 2022;75(4):330-8.
162. Di Costanzo A, Trojsi F, Tosetti M, Giannatempo GM, Nemore F, Piccirillo M, Bonavita S, Tedeschi G, Scarabino T. High-field proton MRS of human brain. *Eur J Radiol*. 2003;48(2):146-53.
163. Soher BJ, Dale BM, Merkle EM. A review of MR physics: 3T versus 1.5T. *Magn Reson Imaging Clin N Am*. 2007;15(3):277-90, v.
164. Ibrahim MA HB, Dublin AB. . Gadolinium Magnetic Resonance Imaging. In: StatPearls I, editor. Internet: Treasure Island (FL); 2021.
165. Geraldès CFGC, Laurent S. Classification and basic properties of contrast agents for magnetic resonance imaging. *Contrast Media & Molecular Imaging*. 2009;4(1):1-23.
166. McLeod SMaM, Thomas J. . 2 Magnetic Resonance Theranostics: An Overview of Gadolinium(III)-Based Strategies and Magnetic Particle Imaging2021.
167. Tircsó G, Molnár, E., Csupász, T., Garda, Z., Botár, R., Kálmán, F. K., ... Tóth, I. . Gadolinium(III)-Based Contrast Agents for Magnetic Resonance Imaging. A Re-Appraisal. In: Techniques MliB-I, editor. Metal Ions in Bio-Imaging Techniques. 2021. p. 39-70.
168. Lee M-J, Kim M-J, Yoon C-S, Song SY, Park K, Kim WS. The T2-Shortening Effect of Gadolinium and the Optimal Conditions for Maximizing the CNR for Evaluating the Biliary System: a Phantom Study. *Korean Journal of Radiology*. 2011;12(3).

References

169. Lagemaat MW, Breukels V, Vos EK, Kerr AB, van Uden MJ, Orzada S, Bitz AK, Maas MC, Scheenen TW. (1)H MR spectroscopic imaging of the prostate at 7T using spectral-spatial pulses. *Magn Reson Med*. 2016;75(3):933-45.
170. Chen AP, Cunningham CH, Kurhanewicz J, Xu D, Hurd RE, Pauly JM, Carvajal L, Karpodinis K, Vigneron DB. High-resolution 3D MR spectroscopic imaging of the prostate at 3 T with the MLEV-PRESS sequence. *Magn Reson Imaging*. 2006;24(7):825-32.
171. Scheenen TW, Gambarota G, Weiland E, Klomp DW, Futterer JJ, Barentsz JO, Heerschap A. Optimal timing for in vivo 1H-MR spectroscopic imaging of the human prostate at 3T. *Magn Reson Med*. 2005;53(6):1268-74.
172. Westphalen AC, Reed GD, Vinh PP, Sotto C, Vigneron DB, Kurhanewicz J. Multiparametric 3T endorectal mri after external beam radiation therapy for prostate cancer. *J Magn Reson Imaging*. 2012;36(2):430-7.
173. Shah V, Turkbey B, Mani H, Pang Y, Pohida T, Merino MJ, Pinto PA, Choyke PL, Bernardo M. Decision support system for localizing prostate cancer based on multiparametric magnetic resonance imaging. *Med Phys*. 2012;39(7):4093-103.
174. Akin O, Hricak H. Imaging of prostate cancer. *Radiol Clin North Am*. 2007;45(1):207-22.
175. Sala E, Akin O, Moskowitz CS, Eisenberg HF, Kuroiwa K, Ishill NM, Rajashanker B, Scardino PT, Hricak H. Endorectal MR Imaging in the Evaluation of Seminal Vesicle Invasion: Diagnostic Accuracy and Multivariate Feature Analysis. *Radiology*. 2006;238(3):929-37.
176. Shukla-Dave A, Hricak H. Role of MRI in prostate cancer detection. *NMR Biomed*. 2014;27(1):16-24.
177. Qayyum A, Coakley FV, Lu Y, Olpin JD, Wu L, Yeh BM, Carroll PR, J. K, Roentgenol. AJ. Organ-confined prostate cancer: effect of prior transrectal biopsy on endorectal MRI and MR spectroscopic imaging. *American Journal of Roentgenology*. 2004;183:1079-83.
178. Shukla-Dave AH, Hedvig; Eberhardt, Steven C.; Olgac, Semra; Muruganandham, Manickam; Scardino, Peter T.; Reuter, Victor E.; Koutcher, Jason A.; Zakian, Kristen L. . Chronic Prostatitis: MR Imaging and 1H MR Spectroscopic Imaging Findings—Initial Observations1. *Radiology*. 2004;231(3):717-24.
179. deSouza NM, Riches SF, Vanas NJ, Morgan VA, Ashley SA, Fisher C, Payne GS, Parker C. Diffusion-weighted magnetic resonance imaging: a potential non-invasive marker of tumour aggressiveness in localized prostate cancer. *Clin Radiol*. 2008;63(7):774-82.
180. Kozlowski P, Chang SD, Goldenberg SL. Diffusion-weighted MRI in prostate cancer -- comparison between single-shot fast spin echo and echo planar imaging sequences. *Magn Reson Imaging*. 2008;26(1):72-6.
181. Mazaheri Y, Vargas HA, Akin O, Goldman DA, Hricak H. Reducing the influence of b-value selection on diffusion-weighted imaging of the prostate: evaluation of a revised monoexponential model within a clinical setting. *J Magn Reson Imaging*. 2012;35(3):660-8.
182. Vargas H, Akin O, Franiel T, Mazaheri Y, Zheng J, Moskowitz C, Udo K, Eastham J, Hricak H. Diffusion-weighted endorectal MR imaging at 3 T for prostate cancer: tumor detection and assessment of aggressiveness. . *Radiology*. 2011;259(3):775-84.

References

183. Verma S, Turkbey B, Muradyan N, Rajesh A, Cornud F, Haider MA, Choyke PL, Harisinghani M. Overview of dynamic contrast-enhanced MRI in prostate cancer diagnosis and management. *AJR Am J Roentgenol.* 2012;198(6):1277-88.
184. Li X, Priest RA, Woodward WJ, Tagge IJ, Siddiqui F, Huang W, Rooney WD, Beer TM, Garzotto MG, Springer CS, Jr. Feasibility of shutter-speed DCE-MRI for improved prostate cancer detection. *Magn Reson Med.* 2013;69(1):171-8.
185. Bloch BN, Lenkinski RE, Rofsky NM. The role of magnetic resonance imaging (MRI) in prostate cancer imaging and staging at 1.5 and 3 Tesla: the Beth Israel Deaconess Medical Center (BIDMC) approach. *Cancer biomarkers : section A of Disease markers.* 2008;4(4-5):251-62.
186. Khawaja AZ, Cassidy DB, Al Shakarchi J, McGrogan DG, Inston NG, Jones RG. Revisiting the risks of MRI with Gadolinium based contrast agents-review of literature and guidelines. *Insights Imaging.* 2015;6(5):553-8.
187. Clough TJ, Jiang L, Wong KL, Long NJ. Ligand design strategies to increase stability of gadolinium-based magnetic resonance imaging contrast agents. *Nat Commun.* 2019;10(1):1420.
188. Choi JW, Moon WJ. Gadolinium Deposition in the Brain: Current Updates. *Korean J Radiol.* 2019;20(1):134-47.
189. Robert P, Frenzel T, Factor C, Jost G, Rasschaert M, Schuetz G, Fretellier N, Boyken J, Idee JM, Pietsch H. Methodological Aspects for Preclinical Evaluation of Gadolinium Presence in Brain Tissue: Critical Appraisal and Suggestions for Harmonization-A Joint Initiative. *Invest Radiol.* 2018;53(9):499-517.
190. Swaminathan S, High WA, Ranville J, Horn TD, Hiatt K, Thomas M, Brown HH, Shah SV. Cardiac and vascular metal deposition with high mortality in nephrogenic systemic fibrosis. *Kidney Int.* 2008;73(12):1413-8.
191. Wang S, Hesse B, Roman M, Stier D, Castillo-Michel H, Cotte M, Suuronen JP, Lagrange A, Radbruch H, Paul F, Taupitz M, Schellenberger E, Sack I, Infante-Duarte C. Increased Retention of Gadolinium in the Inflamed Brain After Repeated Administration of Gadopentetate Dimeglumine: A Proof-of-Concept Study in Mice Combining ICP-MS and Micro- and Nano-SR-XRF. *Invest Radiol.* 2019;54(10):617-26.
192. Wiginton CD, Kelly B, Oto A, Jesse M, Aristimuno P, Ernst R, Chaljub G. Gadolinium-based contrast exposure, nephrogenic systemic fibrosis, and gadolinium detection in tissue. *AJR Am J Roentgenol.* 2008;190(4):1060-8.
193. Cabot RC, Harris NL, Shepard J-AO, Rosenberg ES, Cort AM, Ebeling SH, Peters CC, Kay J, Bazari H, Avery LL, Koreishi AF. Case 6-2008: A 46-Year-Old Woman with Renal Failure and Stiffness of the Joints and Skin. *New England Journal of Medicine.* 2008;358(8):827-38.
194. Aime S, Caravan P. Biodistribution of gadolinium-based contrast agents, including gadolinium deposition. *J Magn Reson Imaging.* 2009;30(6):1259-67.
195. Rogosnitzky M, Branch S. Gadolinium-based contrast agent toxicity: a review of known and proposed mechanisms. *Biometals.* 2016;29(3):365-76.

References

196. Sieber MA, Lengsfeld P, Frenzel T, Golfier S, Schmitt-Willich H, Siegmund F, Walter J, Weinmann HJ, Pietsch H. Preclinical investigation to compare different gadolinium-based contrast agents regarding their propensity to release gadolinium in vivo and to trigger nephrogenic systemic fibrosis-like lesions. *Eur Radiol.* 2008;18(10):2164-73.
197. Behzadi AH, Zhao Y, Farooq Z, Prince MR. Immediate Allergic Reactions to Gadolinium-based Contrast Agents: A Systematic Review and Meta-Analysis. *Radiology.* 2018;286(2):471-82.
198. Sage EH. Regulation of interactions between cells and extracellular matrix: a command performance on several stages. *The Journal of clinical investigation.* 2001;107(7):781-3.
199. Brady-Kalnay SM. Molecular mechanisms of cancer cell-cell interactions: cell-cell adhesion-dependent signaling in the tumor microenvironment. *Cell Adh Migr.* 2012;6(4):344-5.
200. Kaminska K, Szczylik C, Bielecka ZF, Bartnik E, Porta C, Lian F, Czarnecka AM. The role of the cell-cell interactions in cancer progression. *J Cell Mol Med.* 2015;19(2):283-96.
201. Whiteside TL. The tumor microenvironment and its role in promoting tumor growth. *Oncogene.* 2008;27(45):5904-12.
202. Ungefroren H, Sebens S, Seidl D, Lehnert H, Hass R. Interaction of tumor cells with the microenvironment. *Cell Commun Signal.* 2011;9:18.
203. DeBerardinis RJ, Thompson CB. Cellular metabolism and disease: what do metabolic outliers teach us? *Cell.* 2012;148(6):1132-44.
204. Fadaka A, Ajiboye B, Ojo O, Adewale O, Olayide I, Emuowhochere R. Biology of glucose metabolism in cancer cells. *Journal of Oncological Sciences.* 2017;3(2):45-51.
205. O'Connor JP, Aboagye EO, Adams JE, Aerts HJ, Barrington SF, Beer AJ, Boellaard R, Bohndiek SE, Brady M, Brown G, Buckley DL, Chenevert TL, Clarke LP, Collette S, Cook GJ, deSouza NM, Dickson JC, Dive C, Evelhoch JL, Faivre-Finn C, Gallagher FA, Gilbert FJ, Gillies RJ, Goh V, Griffiths JR, Groves AM, Halligan S, Harris AL, Hawkes DJ, Hoekstra OS, Huang EP, Hutton BF, Jackson EF, Jayson GC, Jones A, Koh DM, Lacombe D, Lambin P, Lassau N, Leach MO, Lee TY, Leen EL, Lewis JS, Liu Y, Lythgoe MF, Manoharan P, Maxwell RJ, Miles KA, Morgan B, Morris S, Ng T, Padhani AR, Parker GJ, Partridge M, Pathak AP, Peet AC, Punwani S, Reynolds AR, Robinson SP, Shankar LK, Sharma RA, Soloviev D, Stroobants S, Sullivan DC, Taylor SA, Tofts PS, Tozer GM, van Herk M, Walker-Samuel S, Wason J, Williams KJ, Workman P, Yankeelov TE, Brindle KM, McShane LM, Jackson A, Waterton JC. Imaging biomarker roadmap for cancer studies. *Nat Rev Clin Oncol.* 2017;14(3):169-86.
206. Yang JJ, Yang J, Wei L, Zurkiya O, Yang W, Li S, Zou J, Zhou Y, Maniccia AL, Mao H, Zhao F, Malchow R, Zhao S, Johnson J, Hu X, Krogstad E, Liu ZR. Rational design of protein-based MRI contrast agents. *J Am Chem Soc.* 2008;130(29):9260-7.
207. Lee S, Xie J, Chen X. Peptide-based probes for targeted molecular imaging. *Biochemistry.* 2010;49(7):1364-76.
208. Wei L, Li S, Yang J, Ye Y, Zou J, Wang L, Long R, Zurkiya O, Zhao T, Johnson J, Qiao J, Zhou W, Castiblanco A, Maor N, Chen Y, Mao H, Hu X, Yang JJ, Liu ZR. Protein-based MRI contrast agents for molecular imaging of prostate cancer. *Mol Imaging Biol.* 2011;13(3):416-23.

References

209. Pu F, Qiao J, Xue S, Yang H, Patel A, Wei L, Hekmatyar K, Salarian M, Grossniklaus HE, Liu ZR, Yang JJ. GRPR-targeted Protein Contrast Agents for Molecular Imaging of Receptor Expression in Cancers by MRI. *Sci Rep.* 2015;5:16214.
210. Elshafae SM, Hassan BB, Supsavhad W, Dirksen WP, Camiener RY, Ding H, Tweedle MF, Rosol TJ. Gastrin-releasing peptide receptor (GRPr) promotes EMT, growth, and invasion in canine prostate cancer. *Prostate.* 2016;76(9):796-809.
211. Cornelio DB, Roesler R, Schwartzmann G. Gastrin-releasing peptide receptor as a molecular target in experimental anticancer therapy. *Ann Oncol.* 2007;18(9):1457-66.
212. Heckl S, Pipkorn Rd, Waldeck W, Spring H, Jenne Jr, von der Lieth C-W, Corban-Wilhelm H, Debus Jr, Braun K. Intracellular Visualization of Prostate Cancer Using Magnetic Resonance Imaging. *Cancer Research* 2003;63(16):4766-72.
213. Petrini I, Barachini S, Carnicelli V, Galimberti S, Modeo L, Boni R, Sollini M, PA E. ED-B fibronectin expression is a marker of epithelial-mesenchymal transition in translational oncology. *Oncotarget.* 2016;8(3):4914-21.
214. Wu X, Yu G, Lindner D, Brady-Kalnay SM, Zhang Q, Lu Z-R. Peptide targeted high-resolution molecular imaging of prostate cancer with MRI. *American Journal of Nucl Med Molecular Imaging.* 2014;4(6):525-36.
215. Tan M, Burden-Gulley SM, Li W, Wu X, Lindner D, Brady-Kalnay SM, Gulani V, Lu Z-R. MR Molecular Imaging of Prostate Cancer with a Peptide-Targeted Contrast Agent in a Mouse Orthotopic Prostate Cancer Model. *Pharmaceutical Research.* 2011;29(4):953-60.
216. Li Y, Han Z, Roelle S, DeSanto A, Sabatelle R, Schur R, Lu ZR. Synthesis and Assessment of Peptide Gd-DOTA Conjugates Targeting Extradomain B Fibronectin for Magnetic Resonance Molecular Imaging of Prostate Cancer. *Mol Pharm.* 2017;14(11):3906-15.
217. Karimi M, Ghasemi A, Sahandi Zangabad P, Rahighi R, Moosavi Basri SM, Mirshekari H, Amiri M, Shafaei Pishabad Z, Aslani A, Bozorgomid M, Ghosh D, Beyzavi A, Vaseghi A, Aref AR, Haghani L, Bahrami S, Hamblin MR. Smart micro/nanoparticles in stimulus-responsive drug/gene delivery systems. *Chem Soc Rev.* 2016;45(5):1457-501.
218. Laurent S, Dutz S, Hafeli UO, Mahmoudi M. Magnetic fluid hyperthermia: focus on superparamagnetic iron oxide nanoparticles. *Adv Colloid Interface Sci.* 2011;166(1-2):8-23.
219. Pardo A, Pelaz B, Gallo J, Bañobre-López M, Parak WJ, Barbosa S, del Pino P, Taboada P. Synthesis, Characterization, and Evaluation of Superparamagnetic Doped Ferrites as Potential Therapeutic Nanotools. *Chemistry of Materials.* 2020;32(6):2220-31.
220. Bauer LM, Situ SF, Griswold MA, Samia AC. Magnetic Particle Imaging Tracers: State-of-the-Art and Future Directions. *J Phys Chem Lett.* 2015;6(13):2509-17.
221. Bruns OT, Ittrich H, Peldschus K, Kaul MG, Tromsdorf UI, Lauterwasser J, Nikolic MS, Mollwitz B, Merkel M, Bigall NC, Sapro S, Reimer R, Hohenberg H, Weller H, Eychmuller A, Adam G, Beisiegel U, Heeren J. Real-time magnetic resonance imaging and quantification of lipoprotein metabolism in vivo using nanocrystals. *Nat Nanotechnol.* 2009;4(3):193-201.

References

222. Kudr J, Haddad Y, Richtera L, Heger Z, Cernak M, Adam V, Zitka O. Magnetic Nanoparticles: From Design and Synthesis to Real World Applications. *Nanomaterials (Basel)*. 2017;7(9).
223. Li Q, Kartikowati CW, Horie S, Ogi T, Iwaki T, Okuyama K. Correlation between particle size/domain structure and magnetic properties of highly crystalline Fe₃O₄ nanoparticles. *Sci Rep*. 2017;7(1):9894.
224. Smith BR, Gambhir SS. Nanomaterials for In Vivo Imaging. *Chem Rev*. 2017;117(3):901-86.
225. Woodard LE, Dennis CL, Borchers JA, Attaluri A, Velarde E, Dawidczyk C, Searson PC, Pomper MG, Ivkov R. Nanoparticle architecture preserves magnetic properties during coating to enable robust multi-modal functionality. *Sci Rep*. 2018;8(1):12706.
226. Tromsdorf UI, Bigall NC, Kaul MG, Bruns OT, Nikolic MS, Mollwitz B, Sperling RA, Reimer R, Hohenberg H, Parak WJ, Foerster S, Beisiegel U, Adam G, Weller H. Size and Surface Effects on the MRI Relaxivity of Manganese Ferrite Nanoparticle Contrast Agents. *NANO Letters*. 2007;7(8):2422-7.
227. Frey NA, Peng S, Cheng K, Sun S. Magnetic nanoparticles: synthesis, functionalization, and applications in bioimaging and magnetic energy storage. *Chem Soc Rev*. 2009;38(9):2532-42.
228. Park J, Lee E, Hwang NM, Kang M, Kim SC, Hwang Y, Park JG, Noh HJ, Kim JY, Park JH, Hyeon T. One-nanometer-scale size-controlled synthesis of monodisperse magnetic iron oxide nanoparticles. *Angew Chem Int Ed Engl*. 2005;44(19):2873-7.
229. Kim BH, Shin K, Kwon SG, Jang Y, Lee HS, Lee H, Jun SW, Lee J, Han SY, Yim YH, Kim DH, Hyeon T. Sizing by weighing: characterizing sizes of ultrasmall-sized iron oxide nanocrystals using MALDI-TOF mass spectrometry. *J Am Chem Soc*. 2013;135(7):2407-10.
230. Heine M, Bartelt A, Bruns OT, Bargheer D, Giemsa A, Freund B, Scheja L, Waurisch C, Eychmuller A, Reimer R, Weller H, Nielsen P, Heeren J. The cell-type specific uptake of polymer-coated or micelle-embedded QDs and SPIOs does not provoke an acute pro-inflammatory response in the liver. *Beilstein J Nanotechnol*. 2014;5:1432-40.
231. Sheel R, Kumari P, Panda PK, Jawed Ansari MD, Patel P, Singh S, Kumari B, Sarkar B, Mallick MA, Verma SK. Molecular intrinsic proximal interaction infer oxidative stress and apoptosis modulated in vivo biocompatibility of P.niruri contrived antibacterial iron oxide nanoparticles with zebrafish. *Environ Pollut*. 2020;267:115482.
232. Kwon HJ, Shin K, Soh M, Chang H, Kim J, Lee J, Ko G, Kim BH, Kim D, Hyeon T. Large-Scale Synthesis and Medical Applications of Uniform-Sized Metal Oxide Nanoparticles. *Adv Mater*. 2018;30(42):e1704290.
233. Stoll G, Bendszus M. New approaches to neuroimaging of central nervous system inflammation. *Curr Opin Neurol*. 2010;23(3):282-6.
234. Xiao YD, Paudel R, Liu J, Ma C, Zhang ZS, Zhou SK. MRI contrast agents: Classification and application (Review). *Int J Mol Med*. 2016;38(5):1319-26.
235. Bates D, Abraham S, Campbell M, Zehbe I, Curiel L. Development and characterization of an antibody-labeled super-paramagnetic iron oxide contrast agent targeting prostate cancer cells for magnetic resonance imaging. *PLoS One*. 2014;9(5):e97220.

References

236. Kaittanis C, Bolaender A, Yoo B, Shah N, Ouerfelli O, Grimm J. Targetable Clinical Nanoparticles for Precision Cancer Therapy Based on Disease-Specific Molecular Inflection Points. *Nano Lett.* 2017;17(11):7160-8.
237. Zhu Y, Sun Y, Chen Y, Liu W, Jiang J, Guan W, Zhang Z, Duan Y. In Vivo Molecular MRI Imaging of Prostate Cancer by Targeting PSMA with Polypeptide-Labeled Superparamagnetic Iron Oxide Nanoparticles. *International Journal of Molecular Science.* 2015;16(5):9573-87.
238. Tse BW-C, Cowin GJ, Soekmadji C, Jovanovic L, Vasireddy RS, Ling M-T, Khatri A, Liu T, Thierry Benjamin, Russell PJ. PSMA-targeting iron oxide magnetic nanoparticles enhance MRI of preclinical prostate cancer. *Nanomedicine.* 2015;10(3): 375-86.
239. Bonnans C, Chou J, Werb Z. Remodelling the extracellular matrix in development and disease. *Nat Rev Mol Cell Biol.* 2014;15(12):786-801.
240. Hynes RO. The extracellular matrix: not just pretty fibrils. *Science.* 2009;326(5957):1216-9.
241. Frantz C, Stewart KM, Weaver VM. The extracellular matrix at a glance. *J Cell Sci.* 2010;123(Pt 24):4195-200.
242. Kader A, Kaufmann JO, Mangarova DB, Moeckel J, Brangsch J, Adams LC, Zhao J, Reimann C, Saatz J, Traub H, Buchholz R, Karst U, Hamm B, Makowski MR. Iron Oxide Nanoparticles for Visualization of Prostate Cancer in MRI. *Cancers (Basel).* 2022;14(12).
243. Lu P, Takai K, Weaver VM, Werb Z. Extracellular matrix degradation and remodeling in development and disease. *Cold Spring Harb Perspect Biol.* 2011;3(12).
244. Winkler J, Abisoye-Ogunniyan A, Metcalf KJ, Werb Z. Concepts of extracellular matrix remodeling in tumour progression and metastasis. *Nat Commun.* 2020;11(1):5120.
245. Salesse S, Odoul L, Chazee L, Garbar C, Duca L, Martiny L, Mahmoudi R, Debelle L. Elastin molecular aging promotes MDA-MB-231 breast cancer cell invasiveness. *FEBS Open Bio.* 2018;8(9):1395-404.
246. Li J, Xu X, Jiang Y, Hansbro NG, Hansbro PM, Xu J, Liu G. Elastin is a key factor of tumor development in colorectal cancer. *BMC Cancer.* 2020;20(1):217.
247. Makowski MR, Preissel A, von Bary C, Warley A, Schachoff S, Keithan A, Cesati RR, Onthank DC, Schwaiger M, Robinson SP, Botnar RM. Three-Dimensional Imaging of the Aortic Vessel Wall Using an Elastin-Specific Magnetic Resonance Contrast Agent. *Investigative Radiology.* 2012;47(7):438-44.
248. Makowski MR, Wiethoff AJ, Blume U, Cuello F, Warley A, Jansen CH, Nagel E, Razavi R, Onthank DC, Cesati RR, Marber MS, Schaeffter T, Smith A, Robinson SP, Botnar RM. Assessment of atherosclerotic plaque burden with an elastin-specific magnetic resonance contrast agent. *Nat Med.* 2011;17(3):383-8.
249. Reimann C, Brangsch J, Kaufmann JO, Adams LC, Onthank DC, Thone-Reineke C, Robinson SP, Hamm B, Botnar RM, Makowski MR. Dual-probe molecular MRI for the in vivo characterization of atherosclerosis in a mouse model: Simultaneous assessment of plaque inflammation and extracellular-matrix remodeling. *Scientific reports.* 2019;9(1):13827.

References

250. Brangsch J, Reimann C, Kaufmann JO, Adams LC, Onthank DC, Thone-Reineke C, Robinson SP, Buchholz R, Karst U, Botnar RM, Hamm B, Makowski MR. Concurrent Molecular Magnetic Resonance Imaging of Inflammatory Activity and Extracellular Matrix Degradation for the Prediction of Aneurysm Rupture. *Circulation: Cardiovascular Imaging*. 2019;12(3):e008707.
251. Keller S, Borde T, Brangsch J, Reimann C, Kader A, Schulze D, Buchholz R, Kaufmann JO, Karst U, Schellenberger E, Hamm B, Makowski MR. Assessment of the hepatic tumor extracellular matrix using elastin-specific molecular magnetic resonance imaging in an experimental rabbit cancer model. *Sci Rep*. 2020;10(1):20785.
252. Collettini F, Reimann C, Brangsch J, Chapiro J, Savic LJ, Onthank DC, Robinson SP, Karst U, Buchholz R, Keller S, Hamm B, Goldberg SN, Makowski MR. Elastin-specific MRI of extracellular matrix-remodelling following hepatic radiofrequency-ablation in a VX2 liver tumor model. *Sci Rep*. 2021;11(1):6814.
253. Sun Q, Baues M, Klinkhammer BM, Ehling J, Djudjaj S, Drude NI, Daniel C, Amann K, Kramann R, Kim H, Saez-Rodriguez J, Weiskirchen R, Onthank DC, Botnar RM, Kiessling F, Floege J, Lammers T, Boor P. Elastin imaging enables noninvasive staging and treatment monitoring of kidney fibrosis. *Sci Transl Med*. 2019;11(486).
254. Capuana F, Phinikaridou A, Stefania R, Padovan S, Lavin B, Lacerda S, Almouazen E, Chevalier Y, Heinrich-Balard L, Botnar RM, Aime S, Digilio G. Imaging of Dysfunctional Elastogenesis in Atherosclerosis Using an Improved Gadolinium-Based Tetrameric MRI Probe Targeted to Tropoelastin. *J Med Chem*. 2021;64(20):15250-61.
255. Peng X-H, Qian X, Mao H, Wang AY, Chen ZG, Nie S, Shin DM. Targeted magnetic iron oxide nanoparticles for tumor imaging and therapy. *International journal of nanomedicine*. 2008;3(3):311-21.
256. Chistiakov DA, Killingsworth MC, Myasoedova VA, Orekhov AN, Bobryshev YV. CD68/macrosialin: not just a histochemical marker. *Lab Invest*. 2017;97(1):4-13.
257. Betjes MGH, Haks MC, Tuk CW, Beelen RHJ. Monoclonal Antibody EBM11 (Anti-CD68) Discriminates between Dendritic Cells and Macrophages after Short-Term Culture. *Immunobiology*. 1991;183(1-2):79-87.
258. Mockel J, Brangsch J, Reimann C, Kaufmann JO, Sack I, Mangarova DB, Kader A, Taupitz M, Adams LC, Keller S, Ludwig A, Hamm B, Botnar RM, Makowski MR. Assessment of Albumin ECM Accumulation and Inflammation as Novel In Vivo Diagnostic Targets for Multi-Target MR Imaging. *Biology*. 2021;10(10).
259. Iv M, Samghabadi P, Holdsworth S, Gentles A, Rezaii P, Harsh G, Li G, Thomas R, Moseley M, Daldrup-Link HE, Vogel H, Wintermark M, Cheshier S, Yeom KW. Quantification of Macrophages in High-Grade Gliomas by Using Ferumoxytol-enhanced MRI: A Pilot Study. *Radiology*. 2019;290(1):198-206.
260. Aghighi M, Theruvath AJ, Pareek A, Pisani LL, Alford R, Muehe AM, Sethi TK, Holdsworth SJ, Hazard FK, Gratzinger D, Luna-Fineman S, Advani R, Spunt SL, Daldrup-Link HE. Magnetic Resonance Imaging of Tumor-Associated Macrophages: Clinical Translation. *Clin Cancer Res*. 2018;24(17):4110-8.

References

261. Muehler MR, Rendell VR, Bergmann LL, Winslow ER, Reeder SB. Ferumoxytol-enhanced MR imaging for differentiating intrapancreatic splenules from other tumors. *Abdom Radiol (NY)*. 2021;46(5):2003-13.
262. Sillerud LO, Neuwelt AJ, Staquicini FI, Arap W, Pasqualini R. Repurposing Ferumoxytol as a Breast Cancer-Associated Macrophage Tracer with Five-Dimensional Quantitative [Fe]MRI of SPION Dynamics. *Cancers (Basel)*. 2021;13(15).
263. Daldrup-Link HE, Golovko D, Ruffell B, Denardo DG, Castaneda R, Ansari C, Rao J, Tikhomirov GA, Wendland MF, Corot C, Coussens LM. MRI of tumor-associated macrophages with clinically applicable iron oxide nanoparticles. *Clinical Cancer Research*. 2011;17(17):5695-704.
264. Zanganeh S, Hutter G, Spitler R, Lenkov O, Mahmoudi M, Shaw A, Pajarinen JS, Nejadnik H, Goodman S, Moseley M, Coussens LM, Daldrup-Link HE. Iron oxide nanoparticles inhibit tumour growth by inducing pro-inflammatory macrophage polarization in tumour tissues. *Nature nanotechnology*. 2016;11(11):986-94.
265. Cendrowicz E, Sas Z, Bremer E, Rygiel TP. The Role of Macrophages in Cancer Development and Therapy. *Cancers* 2021;13(8).
266. Vinogradov S, Warren G, Wei X. Macrophages associated with tumors as potential targets and therapeutic intermediates. *Nanomedicine*. 2014;9(5):695-707.
267. Franklin RA, Liao W, Sarkar A, Kim MV, Bivona MR, Liu K, Pamer EG, Li MO. The cellular and molecular origin of tumor-associated macrophages. *Science*. 2014;344(6186):921-5.
268. Nielsen SR, Schmid MC. Macrophages as Key Drivers of Cancer Progression and Metastasis. *Mediators of inflammation*. 2017;2017:9624760.
269. Lissbrandt IF, Stattin P, Wikström P, Damber J-E, Egeva L, Bergh A. Tumor associated macrophages in human prostate cancer: relation to clinicopathological variables and survival. *International journal of oncology*. 2000;17(3):445-96.
270. Lewis CE, Pollard JW. Distinct role of macrophages in different tumor microenvironments. *Cancer Research*. 2006;66(2):605-12.
271. Liu RY, Fan C, Mitchell S, Chen Q, Wu J, Zuckerman KS. The role of type I and type II tumor necrosis factor (TNF) receptors in the ability of TNF-alpha to transduce a proliferative signal in the human megakaryoblastic leukemic cell line Mo7e. . *Cancer research*. 1998;58(10):2217-23.
272. Wu S, Boyer CM, Whitaker RS, Berchuck A, Wiener JR, Weinberg JB, Bast RC. Tumor Necrosis Factor a as an Autocrine and Paracrine Growth Factor for Ovarian Cancer: Monokine Induction of Tumor Cell Proliferation and Tumor Necrosis Factor a Expression1. *Cancer Research*. 1993;53(8):1939-44.
273. Adler HL, McCURDY, M. A., Kattan, M. W., Timme, T. L., Scardino, P. T., & Thompson, T. C. Elevated levels of circulating interleukin-6 and transforming growth factor-beta 1 in patients with metastatic prostatic carcinoma. *The journal of urology*. 1999;161(1):182-7.

References

274. Cassier PA, Treilleux I, Bachelot T, Ray-Coquard I, Bendriss-Vermare N, Ménétrier-Caux C, Trédan O, Goddard-Léon S, Pin J-J, Mignotte H, Bathélémy-Dubois C, Caux C, Lebecque S, Blay J-Y. Prognostic value of the expression of C-Chemokine Receptor 6 and 7 and their ligands in non-metastatic breast cancer. *BMC Cancer*. 2011;11:1-10.
275. Du P, Liu Y, Ren H, Zhao J, Zhang X, Patel R, Hu C, Gan J, Huang G. Expression of chemokine receptor CCR7 is a negative prognostic factor for patients with gastric cancer: a meta-analysis. *Gastric Cancer*. 2017;20(2):235-45.
276. Teh J, Tripathi M, Reichel D, Sagong B, Montoya R, Zhang Y, Wagner S, Saouaf R, Chung LWK, Perez JM. Intraoperative assessment and postsurgical treatment of prostate cancer tumors using tumor-targeted nanoprobes. *Nanotheranostics*. 2021;5(1):57-72.
277. Israel LL, Galstyan A, Holler E, Ljubimova JY. Magnetic iron oxide nanoparticles for imaging, targeting and treatment of primary and metastatic tumors of the brain. *Journal of Controlled Release*. 2020;320:45-62.
278. Xue X, Bo R, Qu H, Jia B, Xiao W, Yuan Y, Vapniarsky N, Lindstrom A, Wu H, Zhang D, Li L, Ricci M, Ma Z, Zhu Z, Lin TY, Louie AY, Li Y. A nephrotoxicity-free, iron-based contrast agent for magnetic resonance imaging of tumors. *Biomaterials*. 2020;257:120234.
279. Wang YX, Idee JM. A comprehensive literatures update of clinical researches of superparamagnetic resonance iron oxide nanoparticles for magnetic resonance imaging. *Quant Imaging Med Surg*. 2017;7(1):88-122.
280. Vavere AL, Kridel SJ, Wheeler FB, Lewis JS. 1-11C-acetate as a PET radiopharmaceutical for imaging fatty acid synthase expression in prostate cancer. *J Nucl Med*. 2008;49(2):327-34.
281. Emonds KM, Swinnen JV, Lerut E, Koole M, Mortelmans L, Mottaghy FM. Evaluation of androgen-induced effects on the uptake of [18F]FDG, [11C]choline and [11C]acetate in an androgen-sensitive and androgen-independent prostate cancer xenograft model. *EJNMMI Research*. 2013;3(1):31.
282. Mohsen B, Giorgio T, Rasoul ZS, Werner L, Ali GR, Reza DK, Ramin S. Application of C-11-acetate positron-emission tomography (PET) imaging in prostate cancer: systematic review and meta-analysis of the literature. *BJU Int*. 2013;112(8):1062-72.
283. Oyama N, Miller TR, Dehdashti F, Siegel BA, Fischer KC, Michalski JM, Kibel AS, Andriole GL, Picus J, Welch MJ. 11C-Acetate PET Imaging of Prostate Cancer: Detection of Recurrent Disease at PSA Relapse. *Journal of Nuclear Medicine*. 2003;44(4):549-55.
284. Schuster DM, Nanni C, Fanti S, Oka S, Okudaira H, Inoue Y, Sorensen J, Owenius R, Choyke P, Turkbey B, Bogsrud TV, Bach-Gansmo T, Halkar RK, Nye JA, Odewole OA, Savir-Baruch B, Goodman MM. Anti-1-amino-3-18F-fluorocyclobutane-1-carboxylic acid: physiologic uptake patterns, incidental findings, and variants that may simulate disease. *J Nucl Med*. 2014;55(12):1986-92.
285. Kairemo K, Rasulova N, Partanen K, Joensuu T. Preliminary clinical experience of trans-1-Amino-3-(18)F-fluorocyclobutanecarboxylic Acid (anti-(18)F-FACBC) PET/CT imaging in prostate cancer patients. *Biomed Res Int*. 2014;2014:305182.

References

286. Nanni C, Schiavina R, Brunocilla E, Borghesi M, Ambrosini V, Zanoni L, Gentile G, Vagnoni V, Romagnoli D, Martorana G, Fanti S. 18F-FACBC compared with 11C-choline PET/CT in patients with biochemical relapse after radical prostatectomy: a prospective study in 28 patients. *Clin Genitourin Cancer*. 2014;12(2):106-10.
287. Lu S, Hoestje SM, Choo EM, Epner DE. Methionine restriction induces apoptosis of prostate cancer cells via the c-Jun N-terminal kinase-mediated signaling pathway. *Cancer Letters*. 2002;179:51-8.
288. Nunez R, Macapinlac HA, Yeung HWD, Akhurst T, Cai S, Osman I, Gonen M, Riedel E, Scher HI, Larson SM. Combined 18F-FDG and 11C-Methionine PET Scans in Patients with Newly Progressive Metastatic Prostate Cancer. *The Journal of Nuclear Medicine*. 2001;43(1):46-55.
289. Ramirez de Molina A, Gutierrez R, Ramos MA, Silva JM, Silva J, Bonilla F, Sanchez JJ, Lacal JC. Increased choline kinase activity in human breast carcinomas: clinical evidence for a potential novel antitumor strategy. *Oncogene*. 2002;21(27):4317-22.
290. Igerc I, Kohlfurst S, Gallowitsch HJ, Matschnig S, Kresnik E, Gomez-Segovia I, Lind P. The value of 18F-choline PET/CT in patients with elevated PSA-level and negative prostate needle biopsy for localisation of prostate cancer. *Eur J Nucl Med Mol Imaging*. 2008;35(5):976-83.
291. Evangelista L, Guttilla A, Zattoni F, Muzzio PC, Zattoni F. Utility of choline positron emission tomography/computed tomography for lymph node involvement identification in intermediate- to high-risk prostate cancer: a systematic literature review and meta-analysis. *Eur Urol*. 2013;63(6):1040-8.
292. Effert P, Beniers AJ, Tammimi J, Handt S, Jakse G. Expression of Glucose Transporter 1 (Glut-1) in Cell Lines and Clinical Specimens from Human Prostate Adenocarcinoma. *Anticancer Research*. 2004;24:3057-64.
293. Yu YC, Desai B, Ji L, Groshen S, Jadvar H. Comparative performance of PET tracers in biochemical recurrence of prostate cancer: a critical analysis of literature. *American Journal of Nucl Med Molecular Imaging*. 2014;4(6):580-601.
294. Vargas HA, Wassberg C, Fox JJ, Wibmer A, Goldman DA, Kuk D, Gonen M, Larson SM, Morris MJ, Scher HI, Hricak H. Bone Metastases in castration- resistant Prostate cancer: Associations between Morphologic CT Patterns, Glycolytic Activity, and Androgen Receptor Expression on PET and Overall Survival1. *Radiology*. 2014;271(1):220-9.
295. Jadvar H, Desai B, Ji L, Conti PS, Dorff TB, Groshen SG, Pinski JK, Quinn DI. Baseline 18F-FDG PET/CT parameters as imaging biomarkers of overall survival in castrate-resistant metastatic prostate cancer. *J Nucl Med*. 2013;54(8):1195-201.
296. Sun H, Sloan A, Mangner TJ, Vaishampayan U, Muzik O, Collins JM, Douglas K, Shields AF. Imaging DNA synthesis with [18F]FMAU and positron emission tomography in patients with cancer. *Eur J Nucl Med Mol Imaging*. 2005;32(1):15-22.
297. Tehrani OS, Muzik O, Heilbrun LK, Douglas KA, Lawhorn-Crews JM, Sun H, Mangner TJ, Shields AF. Tumor imaging using 1-(2'-deoxy-2'-18F-fluoro-beta-D-arabinofuranosyl)thymine and PET. *J Nucl Med*. 2007;48(9):1436-41.

References

298. Mena E, Turkbey B, Mani H, Adler S, Valera VA, Bernardo M, Shah V, Pohida T, McKinney Y, Kwarteng G, Daar D, Lindenberg ML, Eclarinal P, Wade R, Linehan WM, Merino MJ, Pinto PA, Choyke PL, Kurdziel KA. 11C-Acetate PET/CT in localized prostate cancer: a study with MRI and histopathologic correlation. *J Nucl Med.* 2012;53(4):538-45.
299. Caravan P, Das B, Dumas S, Epstein FH, Helm PA, Jacques V, Koerner S, Kolodziej A, Shen L, Sun WC, Zhang Z. Collagen-targeted MRI contrast agent for molecular imaging of fibrosis. *Angew Chem Int Ed Engl.* 2007;46(43):8171-3.
300. Fuchs BC, Wang H, Yang Y, Wei L, Polasek M, Schuhle DT, Lauwers GY, Parkar A, Sinskey AJ, Tanabe KK, Caravan P. Molecular MRI of collagen to diagnose and stage liver fibrosis. *J Hepatol.* 2013;59(5):992-8.
301. Polasek M, Fuchs BC, Uppal R, Schuhle DT, Alford JK, Loving GS, Yamada S, Wei L, Lauwers GY, Guimaraes AR, Tanabe KK, Caravan P. Molecular MR imaging of liver fibrosis: a feasibility study using rat and mouse models. *J Hepatol.* 2012;57(3):549-55.
302. Polasek M, Yang Y, Schuhle DT, Yaseen MA, Kim YR, Sung YS, Guimaraes AR, Caravan P. Molecular MR imaging of fibrosis in a mouse model of pancreatic cancer. *Sci Rep.* 2017;7(1):8114.
303. Erstad DJ, Sojoodi M, Taylor MS, Jordan VC, Farrar CT, Axtell AL, Rotile NJ, Jones C, Graham-O'Regan KA, Ferreira DS, Michelakos T, Kontos F, Chawla A, Li S, Ghoshal S, Chen YI, Arora G, Humblet V, Deshpande V, Qadan M, Bardeesy N, Ferrone CR, Lanuti M, Tanabe KK, Caravan P, Fuchs BC. Fibrotic Response to Neoadjuvant Therapy Predicts Survival in Pancreatic Cancer and Is Measurable with Collagen-Targeted Molecular MRI. *Clin Cancer Res.* 2020;26(18):5007-18.
304. Chen HH, Waghorn PA, Wei L, Tapias LF, Schuhle DT, Rotile NJ, Jones CM, Looby RJ, Zhao G, Elliott JM, Probst CK, Mino-Kenudson M, Lauwers GY, Tager AM, Tanabe KK, Lanuti M, Fuchs BC, Caravan P. Molecular imaging of oxidized collagen quantifies pulmonary and hepatic fibrogenesis. *JCI Insight.* 2017;2(11).
305. Duarte AH, Colli S, Alves-Pereira JL, Martins MP, Sampaio FJB, Ramos CF. Collagen I and III and metalloproteinase gene and protein expression in prostate cancer in relation to Gleason score. *Int Braz J Urol.* 2012;38(3):341-55.
306. Ye F, Jeong E-K, Jia Z, Yang T, Parker D, Lu Z-R. A Peptide Targeted Contrast Agent Specific to Fibrin-Fibronectin Complexes for Cancer Molecular Imaging with MRI. *Bioconjugate Chemistry.* 2008;19(12):2300-3.
307. Ayat NR, Qin JC, Cheng H, Roelle S, Gao S, Li Y, Lu ZR. Optimization of ZD2 Peptide Targeted Gd(HP-DO3A) for Detection and Risk-Stratification of Prostate Cancer with MRI. *ACS Med Chem Lett.* 2018;9(7):730-5.
308. Nair SA, Kolodziej AF, Bhole G, Greenfield MT, McMurry TJ, Caravan P. Monovalent and Bivalent Fibrin-specific MRI Contrast Agents for Detection of Thrombus. *Angewandte Chemie.* 2008;120(26):4996-9.
309. Zhang Z, Kolodziej AF, Qi J, Nair SA, Wang X, Case AW, Greenfield MT, Graham PB, McMurry TJ, Caravan P. Effect of Peptide-Chelate Architecture on Metabolic Stability of Peptide-based MRI Contrast Agents. *New J Chem.* 2010;2010(34):611-6.

References

310. Botnar RM, Perez AS, Witte S, Wiethoff AJ, Laredo J, Hamilton J, Quist W, Parsons EC, Jr., Vaidya A, Kolodziej A, Barrett JA, Graham PB, Weisskoff RM, Manning WJ, Johnstone MT. In vivo molecular imaging of acute and subacute thrombosis using a fibrin-binding magnetic resonance imaging contrast agent. *Circulation*. 2004;109(16):2023-9.
311. Galgano SJ, West JT, Rais-Bahrami S. Role of molecular imaging in the detection of localized prostate cancer. *Ther Adv Urol*. 2022;14:17562872221105018.
312. Martinez J, Subramanian K, Margolis D, O'Dwyer E, Osborne J, Jhanwar Y, Nagar H, Williams N, RoyChoudhury A, Madera G, Babich J, Huicochea Castellanos S. 68Ga-PSMA-HBED-CC PET/MRI is superior to multiparametric magnetic resonance imaging in men with biochemical recurrent prostate cancer: A prospective single-institutional study. *Transl Oncol*. 2022;15(1):101242.
313. Liu FY, Sheng TW, Tseng JR, Yu KJ, Tsui KH, Pang ST, Wang LJ, Lin G. Prostate-specific membrane antigen (PSMA) fusion imaging in prostate cancer: PET-CT vs PET-MRI. *Br J Radiol*. 2022;95(1131):20210728.
314. Li Y, Gao S, Jiang H, Ayat N, Laney V, Nicolescu C, Sun W, Tweedle MF, Lu ZR. Evaluation of Physicochemical Properties, Pharmacokinetics, Biodistribution, Toxicity, and Contrast-Enhanced Cancer MRI of a Cancer-Targeting Contrast Agent, MT218. *Invest Radiol*. 2022.
315. Salarian M, Ibhagui OY, Yang JJ. Molecular imaging of extracellular matrix proteins with targeted probes using magnetic resonance imaging. *Wiley Interdiscip Rev Nanomed Nanobiotechnol*. 2020;12(4):e1622.
316. Heesakkers RAM, Fütterer JJ, Hövels AM, van den Bosch, M.; HC, Scheenen TWJ, Hoogeveen YL, Barentsz JOPCEwF-eT-wMlaaT. Prostate Cancer Evaluated with Ferumoxtran-10-enhanced T2*-weighted MR Imaging at 1.5 and 3.0 T. *Radiology*. 2006;239(2):481-7.
317. Choi JY, Neuhaus ML, Barnett MJ, Hong CC, Kristal AR, Thornquist MD, King IB, Goodman GE, Ambrosone CB. Iron intake, oxidative stress-related genes (MnSOD and MPO) and prostate cancer risk in CARET cohort. *Carcinogenesis*. 2008;29(5):964-70.
318. Choi B, Jung H, Yu B, Choi H, Lee J, Kim DH. Sequential MR Image-Guided Local Immune Checkpoint Blockade Cancer Immunotherapy Using Ferumoxytol Capped Ultralarge Pore Mesoporous Silica Carriers after Standard Chemotherapy. *Small*. 2019;15(52):e1904378.
319. Winter A, Engels S, Kowald T, Paulo TS, Gerullis H, Chavan A, Wawroschek F. [Magnetic Sentinel Lymph Node Detection in Prostate Cancer after intraprostatic Injection of Superparamagnetic Iron Oxide Nanoparticles]. *Aktuelle Urol*. 2017;48(2):132-9.
320. Sankineni S, Smedley J, Bernardo M, Brown AM, Johnson L, Muller B, Griffiths GL, Kobayashi H, Rais-Bahrami S, Pinto PA, Wood BJ, Keele B, Choyke PL, Turkbey B. Ferumoxytol as an intraprostatic MR contrast agent for lymph node mapping of the prostate: a feasibility study in non-human primates. *Acta Radiol*. 2016;57(11):1396-401.
321. Turkbey B, Agarwal HK, Shih J, Bernardo M, McKinney YL, Daar D, Griffiths GL, Sankineni S, Johnson L, Grant KB, Weaver J, Rais-Bahrami S, Harisinghani M, Jacobs P, Dahut W, Merino MJ, Pinto PA, Choyke PL. A Phase I Dosing Study of Ferumoxytol for MR Lymphography at 3 T in Patients With Prostate Cancer. *AJR Am J Roentgenol*. 2015;205(1):64-9.

References

322. Li C-S, Harisinghani MG, Lin W-C, Braschi M, Hahn PF, Mueller PR. Enhancement Characteristics of Ultrasmall Superparamagnetic Iron Oxide Particle Within the Prostate Gland in Patients With Primary Prostate Cancer. *Journal of Computer Assisted Tomography*. 2008;32(4):523-8.

Publications

Adams LC, Truhn D, Busch F, **Kader A**, Niehues SM, Makowski MR, Bressemer KK. Leveraging GPT-4 for Post Hoc Transformation of Free-text Radiology Reports into Structured Reporting: A Multilingual Feasibility Study. *Radiology*. 2023 May;307(4):e230725. doi: 10.1148/radiol.230725. Epub 2023 Apr 4.

Kader A, Kaufmann JO, Mangarova DB, Moeckel J, Adams LC, Brangsch J, Heyl JL, Zhao J, Verlemann C, Karst U, Colleoni F, Auer TA, Hamm B, Makowski MR. Collagen-Specific Molecular Magnetic Resonance Imaging of Prostate Cancer. *Int J Mol Sci*. 2022 Dec 31;24(1):711. doi: 10.3390/ijms24010711.

Kader A, Kaufmann JO, Mangarova DB, Moeckel J, Brangsch J, Adams LC, Zhao J, Reimann C, Saatz J, Traub H, Buchholz R, Karst U, Hamm B, Makowski MR. Iron Oxide Nanoparticles for Visualization of Prostate Cancer in MRI. *Cancers*. 2022; 14(12):2909.

Kaufmann JO, Brangsch J, **Kader A**, Saatz J, Mangarova DB, Zacharias M, Kempf WE, Schwaar T, Ponader M, Adams LC, Möckel J, Botnar RM, Taupitz M, Mägdefessel L, Traub H, Hamm B, Weller MG, Makowski MR. ADAMTS4-specific MR probe to assess aortic aneurysms in vivo using synthetic peptide libraries. *Nature Communication*. 2022 May 23;13(1):2867. doi: 10.1038/s41467-022-30464-8. PMID: 35606349; PMCID: PMC9126943.

Mangarova DB, Bertalan G, Jordan J, Brangsch J, **Kader A**, Möckel J, Adams LC, Sack I, Taupitz M, Hamm B, Braun J, Makowski MR. Microscopic multifrequency magnetic resonance elastography of ex vivo abdominal aortic aneurysms for extracellular matrix imaging in a mouse model. *Acta Biomater*. 2022 Mar 1;140:389-397. doi: 10.1016/j.actbio.2021.11.026. Epub 2021 Nov 21. PMID: 34818577.

Kader A, Brangsch J, Reimann C, Kaufmann JO, Mangarova DB, Moeckel J, Adams LC, Zhao J, Saatz J, Traub H, Buchholz R, Karst U, Hamm B, Makowski MR. Visualization and Quantification of the Extracellular Matrix in Prostate Cancer Using an Elastin Specific Molecular Probe. *Biology*. 2021 Nov 22;10(11):1217. doi: 10.3390/biology10111217. PMID: 34827210; PMCID: PMC8615039.

Makowski MR, Bressemer KK, Franz L, **Kader A**, Niehues SM, Keller S, Rueckert D, Adams LC. De Novo Radiomics Approach Using Image Augmentation and Features From T1 Mapping to Predict Gleason Scores in Prostate Cancer. *Invest Radiol*. 2021 Oct 1;56(10):661-668. doi: 10.1097/RLI.0000000000000788. PMID: 34047538.

Möckel J, Brangsch J, Reimann C, Kaufmann JO, Sack I, Mangarova DB, **Kader A**, Taupitz M, Adams LC, Keller S, Ludwig A, Hamm B, Botnar RM, Makowski MR. Assessment of Albumin ECM Accumulation and Inflammation as Novel In Vivo Diagnostic Targets for Multi-Target MR Imaging. *Biology (Basel)*. 2021 Sep 27;10(10):964. doi:10.3390/biology10100964. PMID: 34681063; PMCID: PMC8533611.

Snellings J*, **Kader A***, Makowski M, Hamm B, Asbach P, Warmuth C, Shahryari M, Tzschätzsch H, Sack I, Braun J. In vivo Magnetic Resonance Elastography of implanted human prostate tumors in a murine model. Oral presentation at: ISMRM. Parent session: Gynecologic & Prostate Cancers. 20 May 2021

Adams LC, Brangsch J, Kaufmann JO, Mangarova DB, Moeckel J, **Kader A**, Buchholz R, Karst U, Botnar RM, Hamm B, Makowski MR, Keller S. Effect of Doxycycline on Survival in Abdominal Aortic Aneurysms in a Mouse Model. *Contrast Media Mol Imaging*. 2021 Apr 27;2021:9999847. doi: 10.1155/2021/9999847. PMID: 34007253; PMCID: PMC8099506.

Zhao J, **Kader A**, Mangarova DB, Brangsch J, Brenner W, Hamm B, Makowski MR. Dynamic Contrast-Enhanced MRI of Prostate Lesions of Simultaneous [⁶⁸Ga]Ga-PSMA-11 PET/MRI: Comparison between Intraprostatic Lesions and Correlation between Perfusion Parameters. *Cancers (Basel)*. 2021 Mar 19;13(6):1404. doi: 10.3390/cancers13061404. PMID: 33808685; PMCID: PMC8003484.

Kader A, Brangsch J, Kaufmann JO, Zhao J, Mangarova DB, Moeckel J, Adams LC, Sack I, Taupitz M, Hamm B, Makowski MR. Molecular MR Imaging of Prostate Cancer. *Biomedicines*. 2020 Dec 22;9(1):1. doi: 10.3390/biomedicines9010001. PMID: 33375045; PMCID: PMC7822017.

Publications

Keller S, Borde T, Brangsch J, Reimann C, **Kader A**, Schulze D, Buchholz R, Kaufmann JO, Karst U, Schellenberger E, Hamm B, Makowski MR. Assessment of the hepatic tumor extracellular matrix using elastin-specific molecular magnetic resonance imaging in an experimental rabbit cancer model. *Sci Rep.* 2020 Nov 27;10(1):20785. doi: 10.1038/s41598-020-77624-8. PMID: 33247185; PMCID: PMC7695832.

Zhao J, Mangarova DB, Brangsch J, **Kader A**, Hamm B, Brenner W, Makowski MR. Correlation between Intraprostatic PSMA Uptake and MRI PI-RADS of [⁶⁸Ga]Ga-PSMA-11 PET/MRI in Patients with Prostate Cancer: Comparison of PI-RADS Version 2.0 and PI-RADS Version 2.1. *Cancers (Basel).* 2020 Nov 26;12(12):3523. doi: 10.3390/cancers12123523. PMID: 33255971; PMCID: PMC7759872.

Keller S, Borde T, Brangsch J, Adams LC, **Kader A**, Reimann C, Gebert P, Hamm B, Makowski M. Native T1 Mapping Magnetic Resonance Imaging as a Quantitative Biomarker for Characterization of the Extracellular Matrix in a Rabbit Hepatic Cancer Model. *Biomedicines.* 2020 Oct 13;8(10):412. doi: 10.3390/biomedicines8100412. PMID: 33066169; PMCID: PMC7601966.

Mangarova DM, Brangsch J, Moeckel J, **Kader A**, Ludwig A, Hamm B, Makowski MR. Current trend in molecular magnetic resonance imaging of the extracellular matrix in atherosclerosis. *J Transl Sci* May 2020 DOI: 10.15761/JTS.1000393

Danksagung

Ich möchte mich herzlich bei Herrn Professor Dr. med. Marcus R. Makowski für die Möglichkeit bedanken, dass ich meine Dissertation an der Charité-Universitätsmedizin Berlin, in der Klinik für Radiologie anfertigen konnte. Er hat mir die Möglichkeit gegeben, mich wissenschaftlich weiterzuentwickeln und mich zu entfalten. Für seine hervorragende wissenschaftliche Betreuung und seine kontinuierliche Unterstützung während meiner Dissertation bin ich ihm sehr dankbar. Außerdem schätze ich sein herausragendes Fachwissen, welches er bereit war zu teilen. Vielen Dank für das Vertrauen in mich.

Mein besonderer Dank gilt auch Herrn Professor Dr. med. Andreas Diefenbach für die Übernahme des Zweitgutachtens meiner Doktorarbeit und für die Betreuung und Unterstützung während der Erarbeitung.

Ich danke außerdem der gesamten Promotionskommission, Professor Dr. med. Andreas Diefenbach, Professor Dr. rer. nat. Daniel Schubert, Professor Dr. med. Marcus R. Makowski, Professor Dr. med. Matthias Taupitz, Professor Dr. Rupert Mutzel, PD Dr. rer. nat. Renate Radek und Dr. Vladimir Jovanovic.

Einen großen Dank möchte ich der gesamten Arbeitsgruppe Makowski aussprechen. Das Arbeitsklima, die Hilfsbereitschaft, die Unterstützung und die wissenschaftlichen Diskussionen habe ich stets geschätzt. Es war und ist mir eine Freude ein Teil dieser interdisziplinären Arbeitsgruppe zu sein. Vielen Dank PD Dr. med. Lisa C. Adams, PD Dr. med. Timo A. Auer, Dr. med. vet. Julia Brangsch, PD Dr. med. Federico Colletini, Jennifer Lilly Heyl, Jan O. Kaufmann, Dr. med. vet. Dilyana B. Mangarova, Jana Möckel, Dr. vet. med. Carolin Reimann und Jing Zhao.

Außerdem möchte ich mich bei allen Kooperationspartnern für die Unterstützung bedanken.

Als Teil des Sonderforschungsbereiches 1340 „Matrix in Vision“ möchte ich mich bei allen Mitgliedern bedanken. Mein besonderer Dank gilt Professor Dr. med. Bernd Hamm, Professor Dr. med. Matthias Taupitz und Maria-Katharina Kuhn.

Bei meiner Familie und bei meinen Freunden möchte ich mich auch bedanken.

Mein besonderer Dank richtet sich an meine Eltern und Geschwister, für die unermüdliche Unterstützung auf meinem Lebensweg. Euch widme ich diese Arbeit.

نہم تیزہ پیشکش ، بہ دایک ، باوک ، خوشک و برای خوشہویستم دہکمہ.

Selbstständigkeitserklärung

Hiermit bestätige ich, dass ich die vorliegende Arbeit selbständig angefertigt habe. Ich versichere, dass ich ausschließlich die angegebenen Quellen und Hilfen in Anspruch genommen habe.

Berlin, den 26.10.2022

Avan Kader

Unterschrift